

NORTHWESTERN UNIVERSITY

Investigation of cascade transitions in Rubidium for all-optical
modulators, switches and polarization controllers

A DISSERTATION

SUBMITTED TO THE GRADUATE SCHOOL
IN PARTIAL FULFILLMENT OF THE REQUIREMENTS

for the degree

DOCTOR OF PHILOSOPHY

Field of Physics and Astronomy

BY

Subramanian Krishnamurthy

EVANSTON, ILLINOIS

June 2014

ACKNOWLEDGEMENTS

ABSTRACT

Investigation of cascade transitions in Rubidium for all-optical modulators, switches and polarization controllers

All-optical modulation and switching are important for optical communication and quantum information processing. Conventional techniques of non-linear optics typically require relatively high power, and are not well suited for these applications. Using a tapered nano fiber (TNF) embedded in Rb vapor, we observed non-linear optical interactions at few nW of power. Design and experimental issues related to the fabrication and deployment of TNF are discussed. High-speed operation is another requirement of all-optical networks. It is well-known that the presence of buffer gas (such as Helium or Ethane) in atomic vapor causes rapid spin-relaxation between the $J=3/2$ and $J=1/2$ states and increased absorption cross-section. In this work, we employ cascade transitions in Rubidium to take advantage of this to develop high-speed all-optical modulators. Under similar conditions, a 100-fold increase in the bandwidth was observed with the possibility of increasing it further by using a higher optical field strength. Together, with the TNF technology, it has the potential to be used for developing ultra-low power high-speed all-optical modulators and switches.

Polarimetric or Stokesmetric Imaging (SI) technique allows us to distinguish objects with similar reflectivity but different polarimetric features. A conventional SI

system consists of a quarter wave plate (QWP) and a linear polarizer (LP), and requires the QWP to be inserted and removed between various readings. Consequently, the speed of the system is greatly limited, which hinders it from being integrated into a real-time system. In this work, we investigated the suitability of a cascade transitions in Rubidium (Rb) for developing optically controlled waveplates and polarizers, which would be capable of functioning at much higher speeds, for use in an SI system. These effects are based on selection rules and quantum interference phenomenon between various Zeeman sub-levels in Rb. Both theoretical and experimental results are presented.

Finally, we also introduce a novel algorithm for numerical evaluation of the steady-state solution and the time-dependent evolution of an arbitrarily large quantum system, where symbolic computations may be too slow or memory intensive and consequently impractical. Use of parallel computing techniques enables extremely efficient and high-speed computation. The algorithm was used extensively employed in simulations of the systems investigated in this work.

Table of Contents	6
Chapter 1 BACKGROUND	7
Chapter 2 TAPERED NANO FIBER	36
Chapter 3 LADDER SYSTEM & MODULATOR	55
Chapter 4 HIGH SPEED MODULATION	68
Chapter 5 OPTICALLY CONTROLLED POLARIZER	76
Chapter 6 OPTICALLY CONTROLLED WAVEPLATE	106
Chapter 7 N-LEVEL ALGORITHM	125
Chapter 8 SUMMARY	160

CHAPTER 1 BACKGROUND

An all-optical switch is one that allows one beam of light, typically called the probe, to be controlled by another, typically called the switching beam. For some types of switches, the presence of this switching beam may control whether or not the probe is present at the output. All-optical switches have far reaching applications in both quantum and classical information processing^{1, 2,3,4}

All-optical switches may be used in classical communication. For long distance communication most signals may be carried in the form of light guided by optical fiber. This method is more efficient than sending signals electronically over long distances since the signal experiences less attenuation over long distances than electronic signals over standard transmission lines. Currently, however, switching within the network must take place electronically. Typically light brought by fibers needs to be converted to an electronic signal by optical to electronic transducers, processed electronically, and then converted back to an optical signal. An efficient all-optical switch, however, could eliminate the need for fiber to copper connections by being able to process the signal while in optical form.

In principle, such a switch could work at a single photon level, allowing direct control of one single photon pulse by another. This could be useful to the field of quantum information processing. This switch could serve as a way of producing entangled states, achieving non-demolition measurements, or implementing an optical logic gate, which in turn may have direct uses in the field of quantum computation. More immediately, a low

light level switch could play an important role in the field of classical information processing by allowing the switching of different individual channels in a many channel system, at a fraction of the input optical power required by current all-optical switches.

Most current all-optical switches depend on intense interactions between light and nonlinear media which may be extremely inefficient. The need for high switching beam powers has prevented all-optical switching from being very useful in most applications. Our research has been primarily aimed at increasing the strength of interactions between light and matter to produce more efficient switches using Tapered Nano Fibers. We have also investigated a high speed modulator by employing buffer gas induced spin relaxation in a cascade system in Rubidium.

It is well documented that in many situations of interest, features indiscernible via conventional imaging become highly resolved under Stokesmetric Imaging (SI)^{5,6,7}. In a typical SI scenario, a target is illuminated by fully or partially polarized light. The light scattered or reflected by the target is then analyzed using a Stokesmeter, which determines the magnitude of each of the four Stokes parameter components. Stokesmeters, in their simplest form, are comprised of a combination of polarizers and wave-plates with different orientations. A key problem with the existing SI systems is that the polarizers and waveplates cannot be turned on or off or reoriented rapidly. The free space versions of the optically controlled polarizers and waveplates that are described in this work have the potential to operate at speeds of few MHz (limited by the

decay rate of the intermediate level) and thus hold the promise of making very high speed SI practical.

This thesis will be divided up in the following way. First I will review the theory of relevant atom-field interactions, including two level systems and pump probe theory. In chapter 2, I will talk about the design of the TNF system and work done using the TNF. In Chapter 3, I will then present some details about the cascade system and the modulator implemented. Chapter 4 talks about the high-speed modulator schematic and experimental results will be presented. Chapter 5 and 6 are dedicated to optically controlled polarizer and waveplate respectively. They will also talk in some detail about the computational model that was adopted for modeling the system. In chapter 7, we present details about a novel computational algorithm that allows us to perform numerical computations of arbitrarily large quantum systems in a highly efficient manner. Finally, in chapter 8, I will present a summary of the thesis.

Two Level Systems

We review briefly, here, the quantum mechanical models of absorption and index of refraction for two and three level atomic systems. First we will discuss two level interactions. We will assume that, if the atom has any other energy levels, they are not coupled, and are unavailable to the system. We are assuming, in other words, that the electric field which drives the transition between the two levels we will be treating here is far off resonance for the other transitions, and that no other fields are present. We first solve the Schrödinger equation to illustrate the behavior of this kind of system, and then

show how the index of refraction and absorption of the material may be calculated from the atomic wavefunctions. Finally we will generalize the approach to derive the index profiles for multi-level systems, in particular three level cascade systems. Consider, then, an electron in the energy well of an atom, initially in its ground state.

Equation 1.1: $\psi(x, t = 0) = \psi_1(x)$

It interacts with an electromagnetic field of the form

Equation 1.2: $\vec{E}(x, t) = E_0 \hat{x} \cos(kz) \cos(\omega t + \phi)$

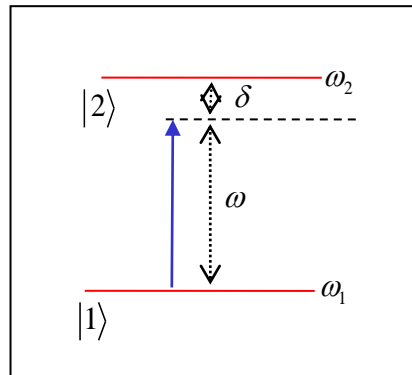


Figure 1.1: Energy level diagram for a two level system

In the presence of the field, the electron will have energy

Equation 1.3: $\hat{H} = \hat{H}_0 + \hat{H}_1$, where $\hat{H}_0 = \frac{\hat{p}^2}{2m} + V(\vec{r})$, $\hat{H}_1 = -\hat{p} \cdot \hat{E}$

The dipole moment of the electron is given by its charge times its distance from the nucleus. This expression of the energy assumes that the wavelength of the light is long

enough that the field is, at any time, approximately constant over the region of the wavefunction for the electron. Now we plug in:

$$\text{Equation 1.4: } \hat{p} = \mu_0 \hat{x} \text{ (electron lies along x axis), so that } \hat{H}_1 = -\mu_0 E_0 \hat{x} \cos(kz) \cos(\omega t)$$

(Note that the carets are intended to indicate operators, not unit vectors.) Since we have assumed that only two levels are available, we can write the wavefunction of the electron at any time as a superposition of those two levels.

$$\text{Equation 1.5: } |\psi(x, t)\rangle = c_1(t)|\psi_1\rangle + c_2(t)|\psi_2\rangle \quad \text{where } c_1(t) = \langle\psi|\psi_1\rangle, c_2(t) = \langle\psi|\psi_2\rangle$$

The Schrödinger equation for the system is then:

$$\text{Equation 1.6: } i\hbar \frac{d}{dt} \begin{bmatrix} c_1(t) \\ c_2(t) \end{bmatrix} = \begin{bmatrix} \langle\psi_1|\hat{H}|\psi_1\rangle & \langle\psi_2|\hat{H}|\psi_1\rangle \\ \langle\psi_1|\hat{H}|\psi_2\rangle & \langle\psi_2|\hat{H}|\psi_2\rangle \end{bmatrix} \begin{bmatrix} c_1(t) \\ c_2(t) \end{bmatrix}$$

We know that

$$\text{Equation 1.7: } \langle\psi_m|\hat{H}_0|\psi_n\rangle = E_m \delta_{mn}$$

where E_m is the energy of the m^{th} level. We then write

$$\text{Equation 1.8: } \hat{H}_1 = -p_0 E_0 \hat{x} \cos(kz) \cos(\omega t + \phi) \approx \frac{-p_0 E_0}{2} \hat{x} \left(e^{i(\omega t + \phi)} + e^{-i(\omega t + \phi)} \right) = f(t) \hat{x}$$

Where we have made use of our assumption that the field is approximately constant over the spatial extent of the wavefunction, at any given time. Thus:

$$\text{Equation 1.9: } \langle\psi_m|\hat{H}_1|\psi_n\rangle = f(t) \langle\psi_m|\hat{x}|\psi_n\rangle$$

Since $|\psi_1\rangle$ and $|\psi_2\rangle$ are eigenfunctions of the unperturbed, spherically symmetric Hamiltonian, we know from symmetry that

$$\text{Equation 1.10: } \langle \psi_1 | \hat{x} | \psi_1 \rangle = \langle \psi_2 | \hat{x} | \psi_2 \rangle = 0$$

We will define

$$\text{Equation 1.11: } x_{12} = \langle \psi_1 | \hat{x} | \psi_2 \rangle = \langle \psi_2 | \hat{x} | \psi_1 \rangle^*$$

We assume this quantity to be real and non-zero. We further define the ‘‘Rabi frequency’’ as

$$\text{Equation 1.12: } \Omega_0 = \frac{-d_0 E_0 x_{12}}{\hbar}$$

We now have

$$\text{Equation 1.13: } \hat{H} = \hbar \begin{bmatrix} \omega_1 & \Omega_0 \left(e^{i(\omega t + \phi)} + e^{-i(\omega t + \phi)} \right) \\ \Omega_0 \left(e^{-i(\omega t + \phi)} + e^{i(\omega t + \phi)} \right) & \omega_2 \end{bmatrix}$$

We now make the ‘‘rotating wave approximation’’⁸, ignoring the complex conjugate terms since they do not strongly couple the levels.

$$\text{Equation 1.14: } H \approx \hbar \begin{bmatrix} \omega_1 & \frac{\Omega_0}{2} e^{-i(\omega t + \phi)} \\ \frac{\Omega_0}{2} e^{i(\omega t + \phi)} & \omega_2 \end{bmatrix}$$

It is this expression for the Hamiltonian that we plug into the Schrödinger equation given as Equation 1.6. In order to solve this equation, we will make some changes of variable.

The goal here is find an effective Hamiltonian which is time independent. First, we introduce a “Q” matrix, where

$$\text{Equation 1.15: } \hat{Q} = \begin{bmatrix} e^{i(\theta_1 t + \eta_1)} & 0 \\ 0 & e^{i(\theta_2 t + \eta_2)} \end{bmatrix} \text{ such that } \hat{Q}^{-1} = \hat{Q}^*$$

We note that

$$\text{Equation 1.16: } \dot{\hat{Q}} = i\hat{M}\hat{Q}$$

We now act on both sides of Equation 1.6 with this Q matrix.

$$\text{Equation 1.17: } \hat{Q} \frac{d|\psi\rangle}{dt} = -\frac{i}{\hbar} \hat{Q} \hat{H} |\psi\rangle$$

We take the derivative and insert an identity operator $\hat{I} = \hat{Q}^{-1}\hat{Q}$:

$$\text{Equation 1.18: } \frac{d\{\hat{Q}|\psi\rangle\}}{dt} - \dot{\hat{Q}}|\psi\rangle = -\frac{i}{\hbar} \hat{Q} \hat{H} \hat{Q}^{-1} \hat{Q} |\psi\rangle$$

We now define two more new variables:

$$\text{Equation 1.19: } |\tilde{\psi}\rangle = \begin{bmatrix} \tilde{c}_1(t) \\ \tilde{c}_2(t) \end{bmatrix} = \hat{Q} |\psi\rangle \text{ and } \hat{H}' = \hat{Q} \hat{H} \hat{Q}^{-1}$$

Equation 1.18 now becomes:

$$\text{Equation 1.20: } \frac{d|\tilde{\psi}\rangle}{dt} = \frac{-i}{\hbar} \hat{H}' |\tilde{\psi}\rangle + i\hat{M} |\tilde{\psi}\rangle = \frac{-i}{\hbar} [\hat{H}' - \hbar\hat{M}] |\tilde{\psi}\rangle$$

We can now write a new equation that strongly resembles the original Schrödinger equation:

Equation 1.21:

$$i\hbar \frac{d|\tilde{\psi}\rangle}{dt} = \tilde{H}|\tilde{\psi}\rangle$$

$$\text{where } \tilde{H} = \hat{H}' - \hbar\hat{M} = \hbar \begin{bmatrix} (\omega_1 - \theta_1) & \frac{\Omega_0}{2} e^{i\omega t + i\phi} e^{i[(\theta_1 t + \eta_1) - (\theta_2 t + \eta_2)]} \\ \frac{\Omega_0}{2} e^{-i\omega t - i\phi} e^{-i[(\theta_1 t + \eta_1) - (\theta_2 t + \eta_2)]} & (\omega_2 - \theta_2) \end{bmatrix}$$

However, if we now choose:

$$\text{Equation 1.22: } \quad \theta_1 - \theta_2 = \omega$$

We eliminate the time dependence. We can further choose, arbitrarily

$$\text{Equation 1.23: } \quad \theta_1 = \omega_1, \quad \eta_1 = 0, \quad \eta_2 = \phi$$

This simplifies our effective Hamiltonian to

$$\text{Equation 1.24: } \quad \tilde{H} = \hbar \begin{bmatrix} 0 & \Omega_0/2 \\ \Omega_0/2 & -\delta \end{bmatrix} \quad \text{where } \delta = \omega - (\omega_1 - \omega_2)$$

We also have

$$\text{Equation 1.25: } \quad |\tilde{\psi}\rangle = \hat{Q}|\psi\rangle = \begin{bmatrix} c_1(t) e^{i\omega t} \\ c_2(t) e^{i(\omega_1 - \omega)t + i\phi} \end{bmatrix} = \begin{bmatrix} \tilde{c}_1(t) \\ \tilde{c}_2(t) \end{bmatrix}$$

Our Schrödinger equation now requires that we take the time derivative of $|\tilde{\psi}\rangle$.

$$\text{Equation 1.26: } \quad i\hbar \frac{d|\tilde{\psi}\rangle}{dt} = i\hbar \begin{bmatrix} \dot{\tilde{c}}_1 \\ \dot{\tilde{c}}_2 \end{bmatrix}$$

We can set this equal to the result of acting upon this wavefunction with the effective Hamiltonian:

Equation 1.27:
$$\tilde{H}|\tilde{\psi}\rangle = \hbar \begin{bmatrix} 0 + \frac{\Omega_0}{2} \tilde{c}_2 \\ \frac{\Omega_0}{2} \tilde{c}_1 - \delta \tilde{c}_2 \end{bmatrix}$$

Setting Equation 1.26 and Equation 1.27 equal, we find

Equation 1.28:
$$\dot{\tilde{c}}_1 = -i \frac{\Omega_0}{2} \tilde{c}_2, \quad \dot{\tilde{c}}_2 = -i \frac{\Omega_0}{2} \tilde{c}_1 + i\delta \tilde{c}_2$$

Taking the derivative of the $\dot{\tilde{c}}_1$ equation gives us

Equation 1.29:

$$\ddot{\tilde{c}}_1 = -i \frac{\Omega_0}{2} \dot{\tilde{c}}_2 = -i \frac{\Omega_0}{2} \left(-i \frac{\Omega_0}{2} \tilde{c}_1 + i\delta \tilde{c}_2 \right) = -i \frac{\Omega_0}{2} \left(-i \frac{\Omega_0}{2} \tilde{c}_1 + i\delta \frac{2i}{\Omega_0} \dot{\tilde{c}}_1 \right) = \left(-\frac{\Omega_0^2}{4} \tilde{c}_1 + i\delta \dot{\tilde{c}}_1 \right)$$

This has the form of a simple harmonic oscillator equation, with the general solution:

Equation 1.30:
$$\tilde{c}_1(t) = \frac{1}{\sqrt{2}} \left[A e^{-i\Omega_A t} + B e^{i\Omega_B t} \right]$$

Below, we plug this into the equation and solve for the undetermined constants.

Equation 1.31:

$$\begin{aligned} -\frac{\Omega_0^2}{4} \tilde{c}_1(t) &= -\frac{\Omega_0^2}{4\sqrt{2}} \left[A e^{-i\Omega_A t} + B e^{i\Omega_B t} \right]; \quad i\delta \dot{\tilde{c}}_1(t) = \frac{\delta}{\sqrt{2}} \left[\Omega_A A e^{-i\Omega_A t} - \Omega_B B e^{i\Omega_B t} \right] \\ \ddot{\tilde{c}}_1(t) &= \frac{1}{\sqrt{2}} \left[-\Omega_A^2 A e^{-i\Omega_A t} - \Omega_B^2 B e^{i\Omega_B t} \right] \\ \rightarrow -\Omega_A^2 &= \delta \Omega_A - \frac{\Omega_0^2}{4} \quad \& \quad -\Omega_B^2 = -\delta \Omega_B - \frac{\Omega_0^2}{4} \end{aligned}$$

The result is

Equation 1.32:
$$\Omega_A = \left(-\delta \pm \sqrt{\delta^2 + \Omega_0^2}\right)/2, \quad \Omega_B = \left(\delta \pm \sqrt{\delta^2 + \Omega_0^2}\right)/2$$

If we plug these in and assume the atom is initially in the ground state so that

Equation 1.33:
$$A(0) + B(0) = \sqrt{2}, \quad A(0) - B(0) = 0, \quad \rightarrow A(0) = B(0) = 1/\sqrt{2}$$

We get the following time evolution for the system:

Equation 1.34:
$$\tilde{c}_1(t) = \frac{1}{2} \left[e^{-i(-\delta \pm \sqrt{\delta^2 + \Omega_0^2})t/2} + e^{i(\delta \pm \sqrt{\delta^2 + \Omega_0^2})t/2} \right] = e^{i\delta t} \cos\left(\sqrt{\delta^2 + \Omega_0^2}t/2\right)$$

The excited state amplitude obeys the same equation (as we see by taking the derivative of the \tilde{c}_2 expression in Equation 1.1):

Equation 1.35:
$$\ddot{\tilde{c}}_2 = -i\frac{\Omega_0}{2} \left(-i\frac{\Omega_0}{2} \tilde{c}_2 \right) + i\delta \dot{\tilde{c}}_2$$

The initial conditions tell us, then, that

Equation 1.36:
$$\tilde{c}_2(t) = \frac{1}{2} \left[e^{-i(-\delta \pm \sqrt{\delta^2 + \Omega_0^2})t/2} - e^{i(\delta \pm \sqrt{\delta^2 + \Omega_0^2})t/2} \right] = i e^{i\delta t} \sin\left(\sqrt{\delta^2 + \Omega_0^2}t/2\right)$$

Equation 1.34 and Equation 1.36 give the solution for the behavior of a two level system under resonant excitation in the absence of decay. They apply in a frame of reference that is said to “rotate with the field”⁸ so that the Hamiltonian is time independent. We can recover the behavior in the non-rotating frame by solving Equation 1.25 for $|\psi\rangle$.

Inverting the transformation gives us

Equation 1.37:
$$|\psi\rangle = \hat{Q}^{-1} |\tilde{\psi}\rangle = \begin{bmatrix} \tilde{c}_1(t) e^{-i\omega_1 t} \\ \tilde{c}_2(t) e^{-i(\omega_1 - \omega)t - i\phi} \end{bmatrix} = \begin{bmatrix} c_1(t) \\ c_2(t) \end{bmatrix}$$

We have solved the system. The phase of the ground and excited state coefficients oscillate rapidly, but the magnitude of those coefficients changes sinusoidally with a frequency $\sqrt{\delta^2 + \Omega_0^2}/2$. This is known as the effective Rabi frequency. It is the rate at which the population of the ground state oscillates in the presence of a driving field.

This solution is, however, physically unrealistic for optical excitation. This model treats the field classically, and does not include the coupling of the atom to the vacuum fluctuations in the electromagnetic field which cause spontaneous decay in real atoms. The decay rate is proportional to the cube of the field energy difference between two states, and is on the scale of tens of nanoseconds for optically coupled transitions⁹. Strictly, the best way to include this effect is to quantize the field and analyze the system in a fully quantum, rather than semi-classical, way. However, it is possible to include the effect in our semi-classical calculations using an empirical “decay matrix,” and that is the approach we will take here.

In order to include decay empirically, however, we need to re-write the problem in the density matrix formalism. This formalism is described in greater detail in reference 8 and 9. It allows us to consider the behavior of a statistical sample of atoms, rather than calculating the behavior of each individually, and to include random, spontaneous decay statistically. The density matrix is defined by

Equation 1.38:
$$\hat{\rho} = \sum_m W_m |\psi_m\rangle\langle\psi_m|$$

The sum is over all atomic states populated by atoms in the sample, and the weight factor indicates what fraction of the atoms in the collection are in each state.

The diagonal elements of this matrix $\rho_{jj} = \sum_m W_m |c_j|^2$ represent the average populations of the energy levels. The off diagonal elements $\rho_{jk} = \sum_m W_m c_j c_k^*$ represent the average phase of superpositions of the two states labeled by the indices. Those off diagonal elements will be zero if all atoms in the collection are in an eigenstate, or if they are all in superpositions but all with different phases.

In this formalism, the equation of motion is written:

Equation 1.39:
$$\dot{\hat{\rho}} = -\frac{i}{\hbar} [\hat{H}, \hat{\rho}] + \dot{\hat{\rho}}_{\text{decay}}$$

The first term is simply the Schrödinger equation restated in the new notation⁸. The second term is empirical, and accounts for the statistical nature of decay.

To solve this equation of motion it is useful to work again in the rotated frame, in which the Hamiltonian is time-independent. To find the density matrix in the rotated frame, we must simply performing the averaging over the $|\tilde{\psi}\rangle$ instead of $|\psi\rangle$ and we find

Equation 1.40:
$$\tilde{\rho} = \begin{pmatrix} \tilde{\rho}_{11} & \tilde{\rho}_{12} \\ \tilde{\rho}_{21} & \tilde{\rho}_{22} \end{pmatrix} = \sum_m W_m |\tilde{\psi}_m\rangle\langle\tilde{\psi}_m| = \hat{Q}\hat{\rho}\hat{Q}^{-1}, \text{ where } |\tilde{\psi}_m\rangle = \hat{Q}|\psi_m\rangle$$

So that

Equation 1.41:

It can be shown⁸ that the equation of motion (the Optical Bloch Equation) is now

$$\text{Equation 1.42: } \dot{\tilde{\rho}} = -\frac{i}{\hbar} [\tilde{H}, \tilde{\rho}] + \dot{\tilde{\rho}}_{\text{decay}}$$

The decay matrix is determined phenomenologically to be⁸:

$$\text{Equation 1.43: } \dot{\tilde{\rho}}_{\text{decay}} = \begin{bmatrix} \Gamma \tilde{\rho}_{22} & -\frac{\Gamma}{2} \tilde{\rho}_{21} \\ -\frac{\Gamma}{2} \tilde{\rho}_{12} & -\Gamma \tilde{\rho}_{22} \end{bmatrix}$$

The presence of decay means the system now eventually settles into a steady state motion which does not depend on its initial condition. The system indeed resembles the damped, driven harmonic oscillator we used for our classical model, with the decay playing the role of the damping force. All motions which are not caused by the driving force will eventually be damped out. So the oscillation that we found at $\sqrt{\delta^2 + \Omega_0^2}/2$ represents only a transient behavior. These oscillations are damped by the interaction with vacuum fluctuations, and on a timescale determined by the inverse of Γ , the amplitude of the oscillations decays. The steady state is time dependent in that the motion of the electron follows that of the driving field, but it is time-independent in the rotating frame in which the field is constant.

The steady state is that which satisfies the condition:

$$\text{Equation 1.44: } \dot{\tilde{\rho}} = -\frac{i}{\hbar} [\tilde{H}, \tilde{\rho}] + \dot{\tilde{\rho}}_{\text{decay}} = 0$$

In general, it is more convenient to solve this numerically (or using a symbolic equation solver such as Wolfram's *Mathematica*) than by hand. The solution in this case is:

Equation 1.45:

$$\tilde{\rho}_{11} = 1 - \frac{\Omega^2}{2\Omega^2 + \Gamma^2 + 4\delta^2}, \quad \tilde{\rho}_{12} = \frac{i(\Omega\Gamma - 2i\Omega\delta)}{2\Omega^2 + \Gamma^2 + 4\delta^2},$$

$$\tilde{\rho}_{21} = \frac{-i(\Omega\Gamma + 2i\Omega\delta)}{2\Omega^2 + \Gamma^2 + 4\delta^2}, \quad \tilde{\rho}_{22} = \frac{\Omega^2}{2\Omega^2 + \Gamma^2 + 4\delta^2}$$

As we mentioned above, the off diagonal elements tell us about the average number of atoms in superposition states, and whether or not those superpositions are generally in phase. The relevance of this phase for dispersion calculations is well illustrated by the solutions to, for example, the infinite square well:

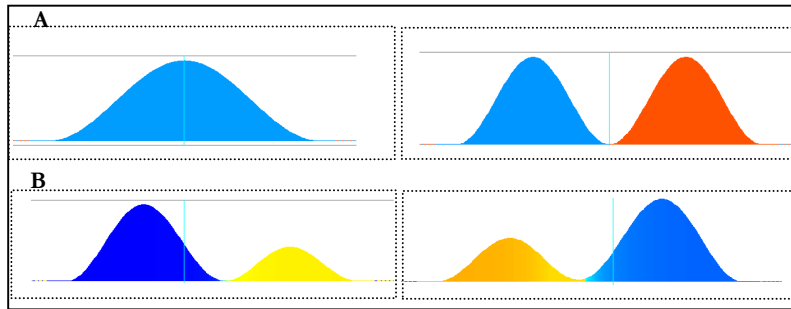


Figure 1.1: A) Probability distributions for particles in ground state and first excited state of infinite square well. B) Probability distributions for superpositions of ground and first excited states: two different phases.

The position of the electron, and thus the dipole moment of the atom, changes with the phase of the superpositions. Eigenstates of the unperturbed Hamiltonian are symmetric and thus atoms in these have zero dipole moment. If the sample includes

atoms in superposition states, but the phase of the superposition states is random, the average dipole moment, which gives the polarization of the material, will again be zero.

If, on the other hand, the atoms, following the field, are all stretched into the same superposition state, these off diagonal components will not be zero, and their values will tell us about the phase difference between the motion of the atomic dipole and that of the field. Recall that the index of refraction is determined by the difference in phase between the field radiated by the atomic dipoles in the medium and the driving field. The phase of the radiated field is, in general, 90 degrees out of phase with the motion of the dipoles themselves^{Error! Bookmark not defined.}. To calculate the index of refraction and the absorption coefficient explicitly, we must make use of a theorem provable from the density matrix formalism:

Equation 1.46:
$$\langle \hat{x} \rangle = Tr(\rho \hat{x}) = x_0(\rho_{21} + \rho_{12})$$

This applies to any operator, not just the position operator. However, it is the average position of the electron with which we are primarily concerned. We have already seen, in the previous chapter, how knowing the average position of the electrons relative to their nuclei, and hence the average dipole moment, allows us to calculate the polarization response of the material, and how this response function can be plugged into the wave equation to allow us to calculate the index of refraction and the absorption coefficient.

We expect this value for the average position to be a real number with a sinusoidal time dependence, matching the time dependence of the driving field. However, because it

will be out of phase with the driving field, we cannot express this number as a scalar multiple of the driving field unless we use phasor notation. We “complexify” x by dropping the complex conjugate, so that:

Equation 1.47: $\langle \hat{x} \rangle_C = x_0(\rho_{21})$

The phase of this complex number tells us the relative phase between the motion of the field and that of the electron.

The dipole moment of an individual atom in the rotating frame is then $ex_0\tilde{\rho}_{21}$. If this is simply a positive scalar multiple of i (keeping in mind that e , the charge on the electron, is negative), it means the phasor is of the form $|ex_0\rho_{21}|Exp[i\pi/2]$, and the dipole motion is $\pi/2$ radians (90 degrees) out of phase with the driving field. The radiated field is thus 180 degrees out of phase with the driving field. That this is the case when $\delta = 0$ can be seen from Equation 1.45. On resonance, then, the radiated field adds destructively with the driving field. This shows qualitatively that an imaginary $ex_0\tilde{\rho}_{21}$ is associated with absorption. If $ex_0\tilde{\rho}_{21}$ were proportional to $-i$, the radiated field would then add in phase with the driving field, and the result would be gain, which is mathematically equivalent to negative absorption. If $ex_0\tilde{\rho}_{21}$ is real, then the dipole motion will itself be in phase with the driving field, meaning the radiated field is 90 degrees out of phase with it. The net field produced lags behind the original driving field by an amount that depends on the relative strengths of the original field and the reradiated field. This shows qualitatively that the real part of $\tilde{\rho}_{21}$ is associated with index of refraction.

To demonstrate these effects mathematically, we need only calculate the polarization:

$$\text{Equation 1.48: } P_C = Np_C = Ne\langle x \rangle_C = Nex_0(\rho_{21}) = \varepsilon_0\chi E_C \quad \text{where } E_C = E_0e^{i\omega t}$$

The subscript ‘‘C’’ is intended to indicate that these are complex phasors and not real quantities. (In the previous chapter we used a tilde for this purpose, however since we have used that same notation already in this chapter to indicate quantities which are expressed in the rotating frame, we must change our convention slightly.) The real quantities are given by the sum of the phasor with its complex conjugate.

We have already determined ρ_{21} , so Equation 1.48 allows us to calculate the average dipole moment of the ensemble, which tells us the polarization and thus, the susceptibility of the medium as

$$\text{Equation 1.49: } \chi = \frac{Nex_0(\rho_{12})}{\varepsilon_0 E_C} \quad \text{where } E_C = E_0e^{i\omega t}$$

From this point on, the calculation of the index is exactly the same as it is in the classical case. Therefore, we conclude that:

$$\text{Equation 1.50: } n = \frac{c}{v_p} = \frac{cK_R}{\omega} = \text{Re}\left[\sqrt{1+\chi}\right] = \text{Re}\left[\sqrt{1+\frac{Nex_0(\rho_{21})}{\varepsilon_0 E_C}}\right]$$

Therefore:

$$\text{Equation 1.51: } n \approx 1 + \frac{1}{2} \frac{Nex_0 \text{Re}\left[\frac{-i(\Omega\Gamma + 2i\Omega\delta)}{2\Omega^2 + \Gamma^2 + 4\delta^2}\right]}{\varepsilon_0 E_C}$$

We need only specify our driving field strength and frequency (which determine $\Omega, E_C,$ and δ) and the decay rate and resonant frequency of our atomic energy levels in order to completely determine the index for a two level system.

Similarly, the absorption is given by:

Equation 1.52:
$$\alpha_L = -2\kappa_I = -2 \operatorname{Im} \left[\omega \sqrt{\mu_0 \epsilon_0 (1 + \chi)} \right] = -2 \operatorname{Im} \left[\omega \sqrt{\mu_0 \epsilon_0 \left(1 + \frac{Nex_0(\rho_{21})}{\epsilon_0 E_C} \right)} \right]$$

Therefore:

Equation 1.53:
$$\alpha_L \approx -2\omega \sqrt{\mu_0 \epsilon_0} \left(1 + \frac{1}{2} \operatorname{Im} \left[\frac{Nex_0 \left(\frac{-i(\Omega\Gamma + 2i\Omega\delta)}{2\Omega^2 + \Gamma^2 + 4\delta^2} \right)}{\epsilon_0 E_C} \right] \right)$$

Plotting the expression for the index gives us:

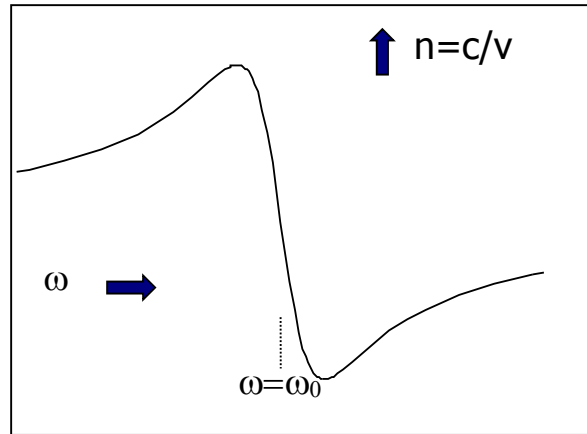


Figure 1.2: Lineshape of index of refraction vs. frequency derived using two-level quantum mechanical model.

For the absorption coefficient, we get:

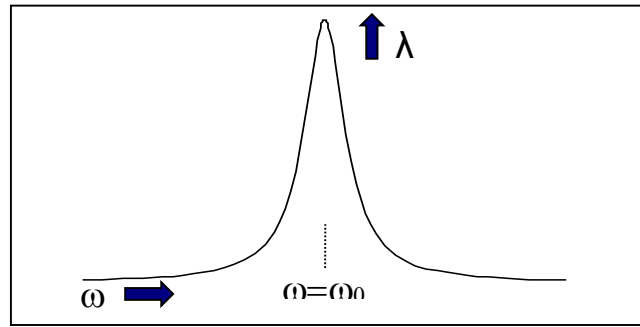


Figure 1.3: Lineshape of absorption vs. frequency derived using two-level quantum mechanical model.

These lineshapes clearly agree with the results derived using the classical model. This is the same approach we will now use (with less derivation) to model the behavior of three level systems.

PUMP PROBE THEORY

In the following section I will discuss several different types of systems which consist of two beams (a pump and a probe), and either two or three atomic levels. Within pump-probe systems, the pump beam is used to affect the interaction of the probe with an atomic medium. We will investigate how to use a pump to induce probe transparency within the medium, and discuss the switching applications of these systems.

The systems we will consider are the following. First we will look at a two level co- and counter-propagating pump-probe system with the pump and probe having the same polarization. Next we will investigate three level counter-propagating pump-probe systems, also of the same polarization, and see how these systems lead to V-type EIT. We will then see how linearly cross polarized co- and counter-propagating pump and probe behave in a two level atom. Lastly we will explore how the cross polarized co- and counter-propagating pump and probe behave in a three level atom.

Co-propagating Saturated Absorption

One method for inducing transparency in a system is by saturation. The simplest example of this is that of an overlapped co-propagating pump and probe traveling through an atomic vapor. Consider this for a two level system in the following way. First note that if a resonant weak probe ($\Omega_{probe} \ll \Gamma$) is sent through a collection of two level atoms, the output probe intensity would decrease as photons from the field are absorbed and fluoresced in random directions.

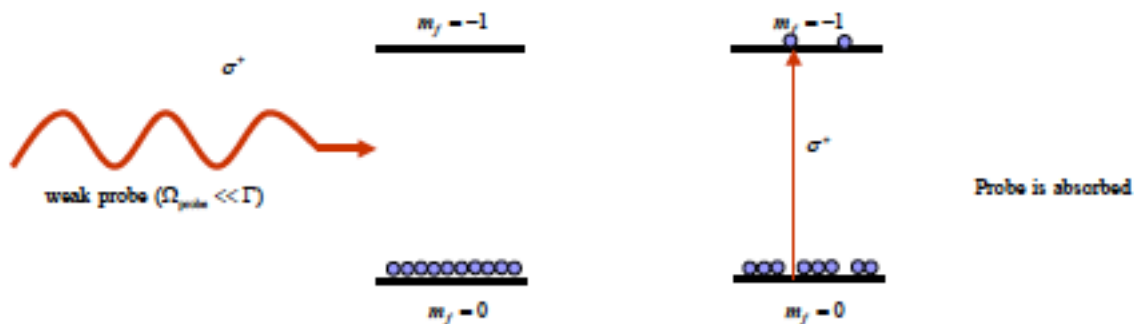


Figure 1.4 Absorption of a probe in a two level system

Next, assume a resonant strong pump is overlapped and co-propagating with the weak probe and sent through the system. If the pump is sufficiently strong ($\Omega_{pump} \gg \Gamma$), the system will be come saturated, having equal number of atoms in the ground state and excited state. At this point, atoms in the system can no longer absorb photons, and the medium will be transparent to the weak probe.



Figure 1.5 Saturation induced transparency of probe in two level system
Counter-propagating Saturated Absorption

Doppler free spectroscopy, otherwise known as counter-propagating saturated absorption, allows one to resolve hyperfine levels in a Doppler broadened atomic medium. In an atomic vapor atoms have a velocity spread corresponding to the Boltzmann energy distribution. If a scanning beam is sent an atomic vapor to probe atomic resonance, a broad resonance profile on the order of a GHz would be measured even though the actual linewidth of Rubidium is on the order of MHz. The profile measured can be thought of as a convolution or a weighted averaged of the Doppler free absorption profile with the Boltzman distribution as shown in the diagram below.

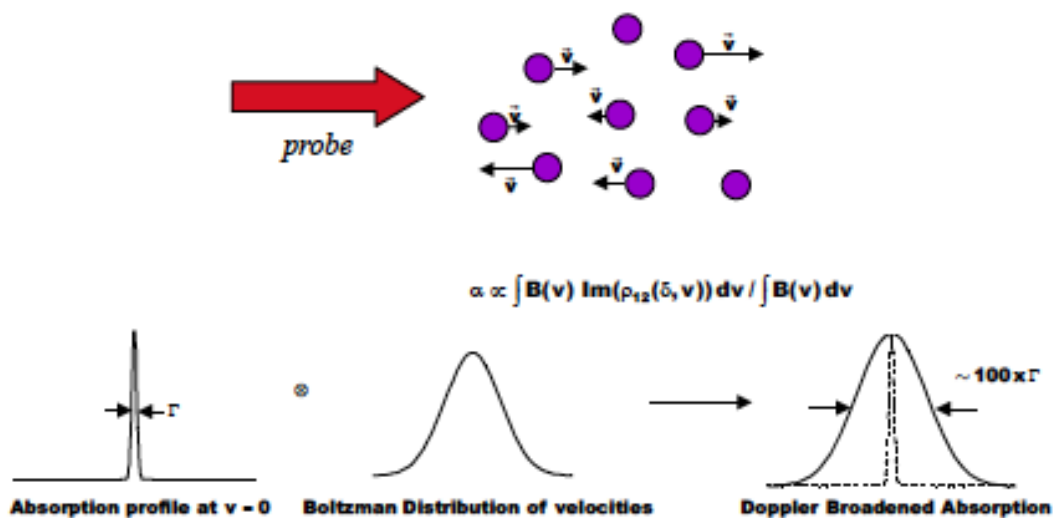


Figure 1.6 Illustration of Doppler Broadening of Linear Absorption

This linear absorption profile is shown below for the $F=3$, D2 transitions in Rb85.

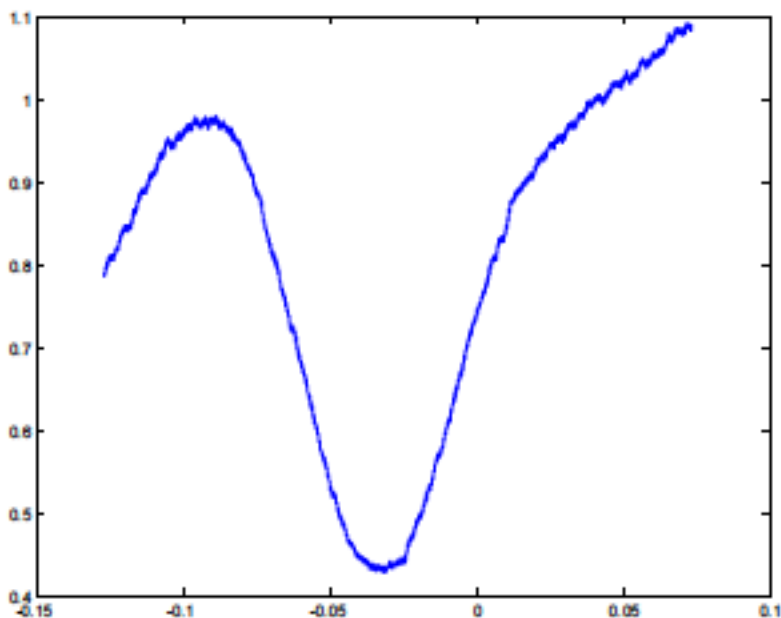


Figure 1.7 *Intensity vs frequency trace of Doppler Broadened linear absorption for Rb 85, $5S_{1/2}$ $F = 3$ transitions*

In order to resolve the hyper fine energy levels, we can send a counter-propagating pump of the same frequency, derived from the same laser, through the atomic vapor. Note that with a counter-propagating pump and probe, the zero velocity atoms are the only velocity group which will see the probe and pump at the same frequency. For example, if, as the probe frequency is scanned, a velocity group other than the zero velocity group experiences a resonant probe, the pump will either be red or blue shifted from resonance depending on the direction of motion. If the pump is strong enough to saturate the atomic transition at resonance condition, these zero velocity atoms will be transparent to the probe field, even though other atoms within the Doppler profile will still absorb the

probe, as it is scanned through their Doppler-shifted resonances.

We note that for a co-propagating pump and probe as discussed above, all velocity groups see the two fields at the same frequency. Therefore the behavior is identical to that of the counter-propagating saturated absorption at the zero velocity group.

The result for counter-propagating beams in a multilevel system is shown below for the $F=3$, D2 transition in Rb85, having three hyperfine transitions, and three cross-over peaks, which will be discussed below.

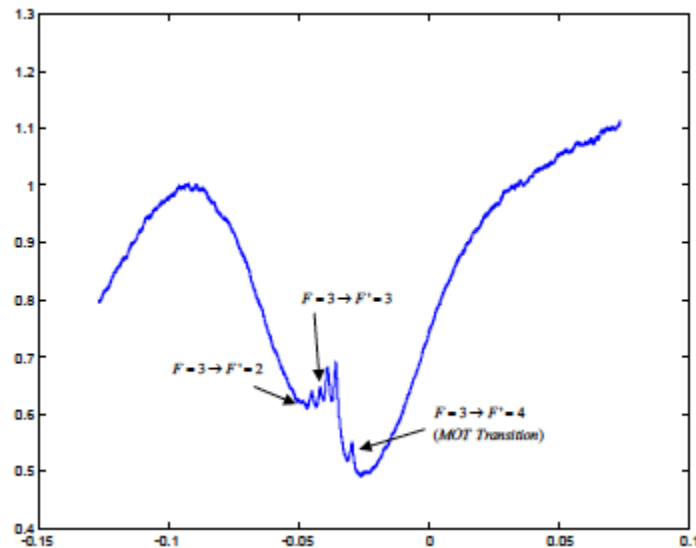


Figure 1.8 *Intensity vs frequency trace of saturated absorption in Rb85, $5S_{1/2} F = 3$ showing zero velocity peaks and V-type EIT cross over peaks (see below for details)*

Three Level Counter-Propagating Pump-Probe System of the same Polarization (V-type EIT)

Note that even though there are only three hyperfine transitions, six peaks are present. These extra peaks are known as cross-over peaks. This induced transparency is caused by

a different mechanism than saturation discussed above. When the laser is scanned to a frequency half way between two resonant frequencies, the velocity group at $\Delta\omega/2k$ experiences a probe Doppler shifted towards resonance for one transition and the pump oppositely Doppler shifted towards resonance for the other transition. This is shown in the diagram below for a cross-over peak located half way between $F = 3 \rightarrow F = ' 2$ and $F = 3 \rightarrow F = ' 3$.

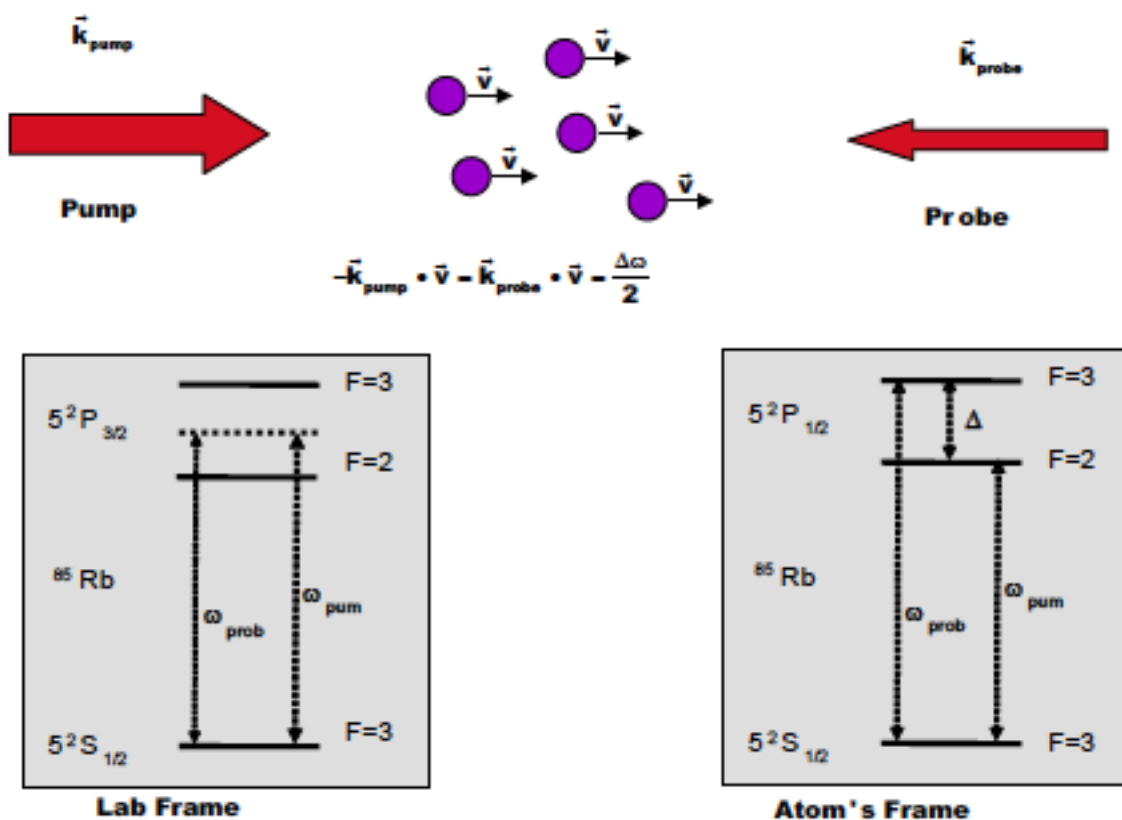


Figure 1.9 This figure describes the idea behind cross over peaks

We see that when the frequency is, in the lab frame, half way between the two atomic transitions, the velocity group located at $v = \pm \Delta\omega/2k$ experiences the pump and probe beams as resonant on two different transitions. In the frame of the atom, this can be

viewed as a three level V-type EIT system.¹⁰

The stronger pump field imparts a light shift on the ground state, causing the system to be transparent to the probe. This behavior can be understood in the frame of the atom by noting that when a strong field is applied to the effective pump leg, the atom-field interaction energy shifts the ground state eigen-energy to that of the dressed state. This results in the beam which was once resonant for the probe leg becoming off resonant by an amount equal to the light shift. If the value of the light shift is larger than Γ , the probe will be transmitted. We find that when a strong pump is applied, a cross-over peak is always present in the saturated absorption profile between two resonance peaks. This light shift induced transparency may be found in any multi-level atom.

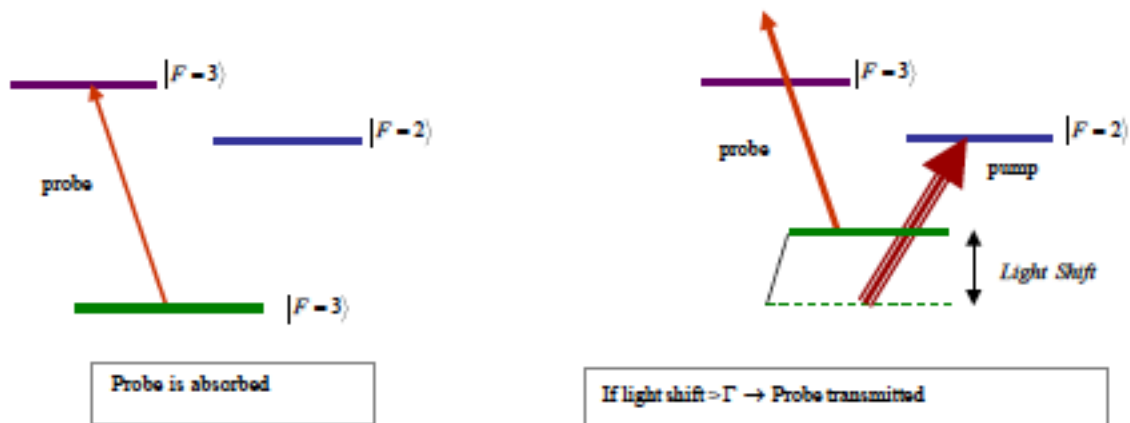


Figure 1.10 *Illustration of how light shifts can induce probe transparency*

Three Level Linearly Crossed Polarized Co- and Counter- Propagating Pump-Probe System

If we consider the interaction of the linearly cross polarized light with a multilevel system, however, we find that another mechanism for inducing transparency is present. We find that in a multilevel atom the behavior of the density matrix elements is not affected by the relative phases of the fields. This may be seen in the following way. For

the three level V-type system below, the $m \rightarrow 0 +m= 1$ transition interacts with σ^+ light, whereas the $m \rightarrow 0 -m= 1$ transition interacts with σ^- light.

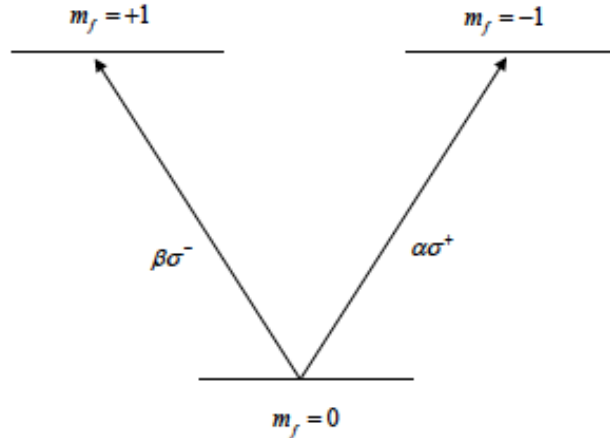


Figure 1.11 Three level system coupled by σ^+ and σ^- light

If we make a transformation to another 3 level basis for which

$$|+\rangle = \frac{1}{2}(|m_f = +1\rangle + |m_f = -1\rangle) \text{ and } |-\rangle = \frac{e^{i\phi}}{2}(|m_f = +1\rangle - |m_f = -1\rangle),$$

We get the three level system shown below, where now, the states are coupled by linearly polarized light. This is comparable to the V-type EIT situation discussed above, however, in this case the excited states are degenerate in energy.

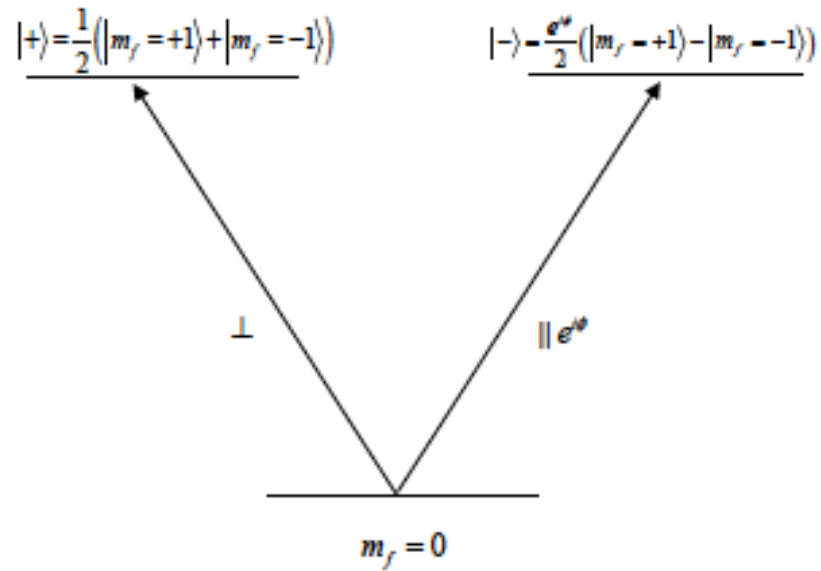


Figure 1.12 *Three level system coupled by \parallel and \perp light*

Note that this system is not affected by the relative phase differences between the two beams. If a weak \perp - polarized probe is present in this multilevel scheme, it will be absorbed by the $|+\rangle$ state. If a \parallel - polarized pump is also present, regardless of the relative phase between the two, it will induce a light shift on the ground state, as shown below. Similar to the V-type EIT case discussed above, this will cause the medium to be transparent to the probe.

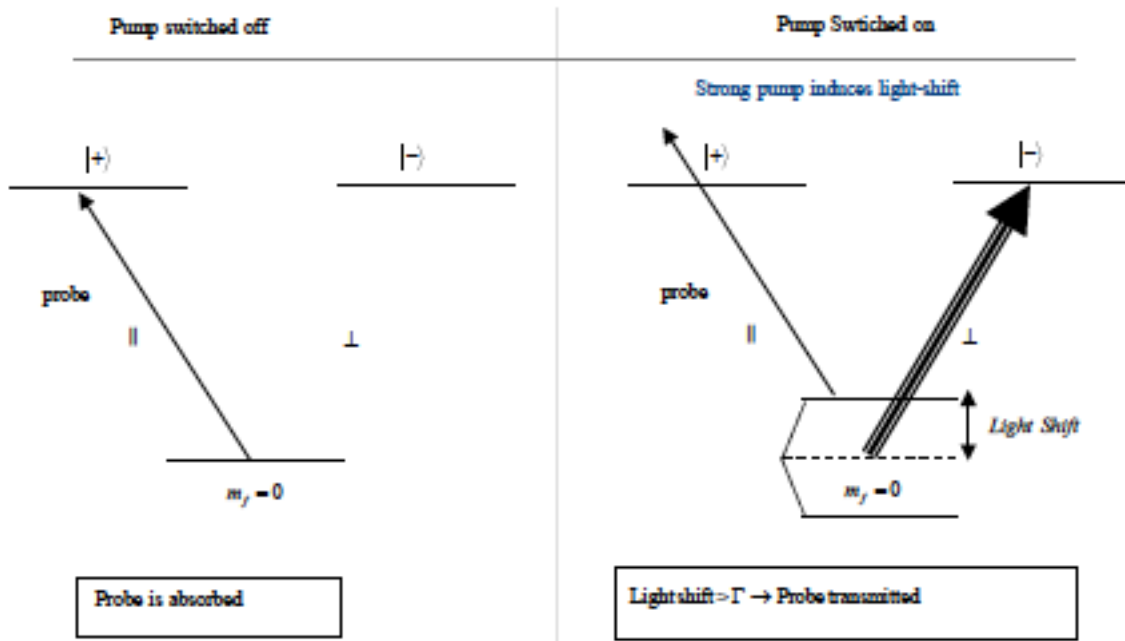


Figure 1.13 This illustration shows probe absorption when the pump field is off, and light shift induced probe transmission when the pump field is switched on

Since this process is unaffected by phase differences in the pump and probe it can be the dominant cause for induced probe transparency regardless of such factors such as mirror vibrations, and variations in optical path differences between the two beams.

Note that this is identical to the behavior we would observe for zero velocity group atoms in a counter-propagating saturated absorption experiment where the beams were cross-polarized.

Counter-propagating saturated absorption experiments also have cross-over peaks, as discussed above for the case of matching polarization. For the velocity group which experiences a cross-polarized pump and probe as resonant for two different non-degenerate levels, we can use a three level model similar to the cross-polarized model above. The energy diagram for this is shown below.

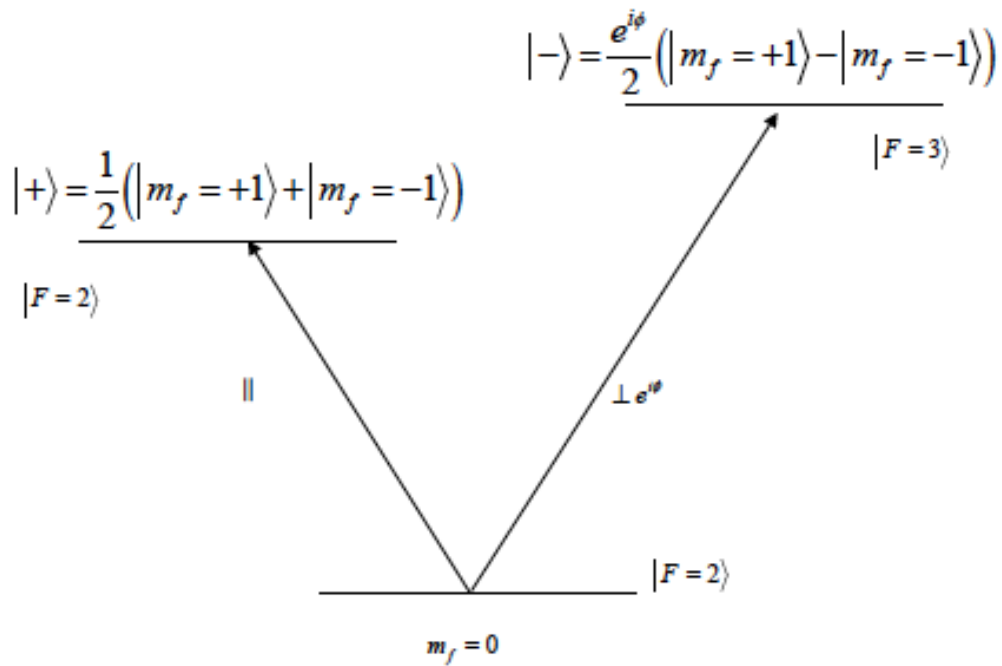


Figure 1.14 *Illustration of three level system corresponding to linearly cross polarized V-type system*

Again the ground state can be light-shifted by the stronger pump beam, creating the transparency for the weaker probe beam.

CHAPTER 2 TAPERED NANO FIBER – THEORY AND EXPERIMENTS

To minimize the energy cost per switching event we would like the switching beam and probe to be efficient at low optical powers. To improve switching efficiency we must increase the interaction strength between the atoms and our beams. One way to accomplish this is to increase the number of atoms that interact with our beams. The other way to increase interaction strength is to increase the electric field strength per photon by the use of tapered nano- fibers (TNF), for example. An advantage of using TNF over optical resonators is that switching may be implemented directly in optical fiber

TNF Theory

The TNF consists of standard single mode silica optical fiber for which a small section, approximately 3 cm, is heated and pulled so that the diameter in this region is reduced to approximately 500 nm. The mode guided by the fiber will adiabatically decrease in mode area as it travels down the tapered region, increasing in intensity to as much as 60,000 times the original intensity. (With this type of enhancement, saturation of a stationary Rb atom can be achieved at approximately 20 pW.) The fiber will also convert the original mode from one which is guided by the core/cladding interface to one which is guided by the cladding/environment interface. This results in an evanescent mode which leaks into the environment. When inserted into either atomic vapor or cold atoms, this evanescent field can interact directly with the atoms. This is illustrated below

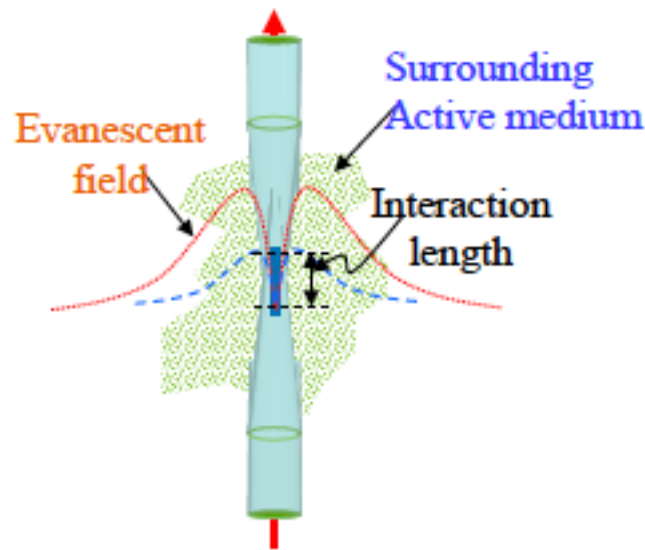


Figure 2.1 *This figure illustrates a tapered nano-fiber (TNF).*

Numerical simulations of the TNF yield the data shown below and are also reported in other works.^{11,12,13} The first plot shows the fraction of energy located in the evanescent field and mode volume as a function of fiber diameter. We find that the minimum mode area, $0.2 \mu\text{m}^2$, is obtained for a fiber diameter of approximately $0.45 \mu\text{m}$. As the diameter is reduced further, the mode quickly delocalizes causing a rise in mode area. At this diameter, we find that that fraction of energy outside the fiber corresponds to approximately 10%.

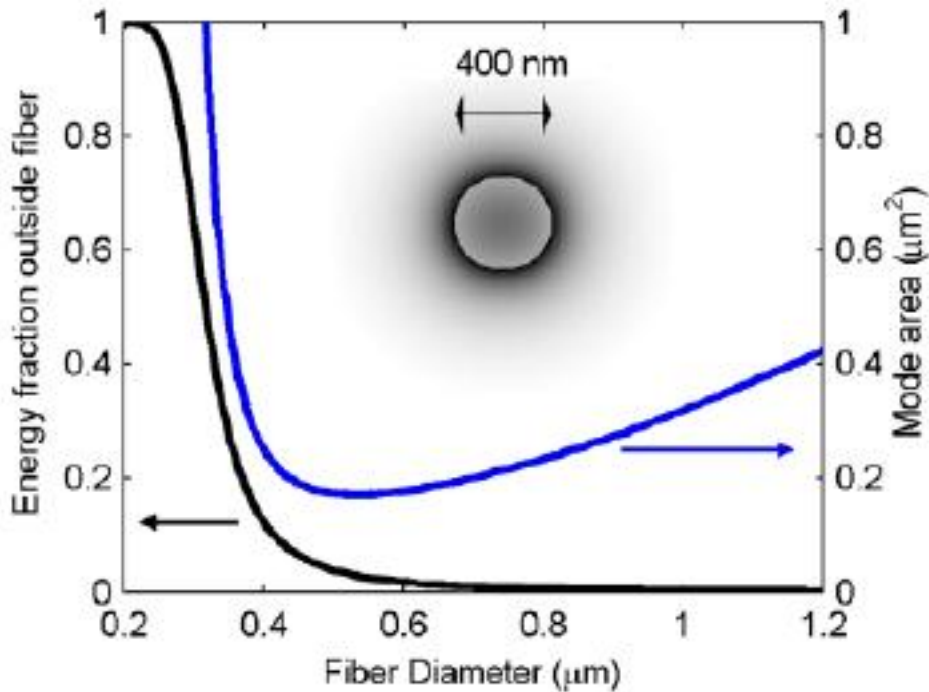


Figure 2.2 fraction of mode energy outside fiber (black) and Mode area (blue) versus the fiber diameter

Atoms with velocities typically found in hot vapor can pass through the small mode area of the TNF in a few nanoseconds. This is much shorter than the natural decay time of the atom (approximately 25 ns) and leads to an effect known as transit time broadening. We can understand transit time broadening by picturing the field from the reference frame of the moving atom. As the atom moves through the field, it experiences a temporally varying field with a shape dependent on the transverse optical mode field. This pulse has a spread of frequency components determined by its Fourier transform. To observe the broadening of atomic linewidth, one may scan the laser supplying the TNF field. As the laser scans through frequencies which are nonresonant in the lab frame, the pulse seen by the atom may still have a component at the resonant frequency and consequently still be partially absorbed. Furthermore, due to energy conservation, the total power of the pulse must be distributed among the frequency components dictated by its Fourier transform. For this reason, when the laser is tuned to resonance, the power contained in the component of the field at the resonant frequency will be less for an atom moving through

the field than for a stationary atom. This results in higher saturation powers for atomic vapor. Note that effects due to transit time broadening are negligible in cold atoms. The figure below shows calculated transit time linewidth and saturation powers as a function of taper diameter.

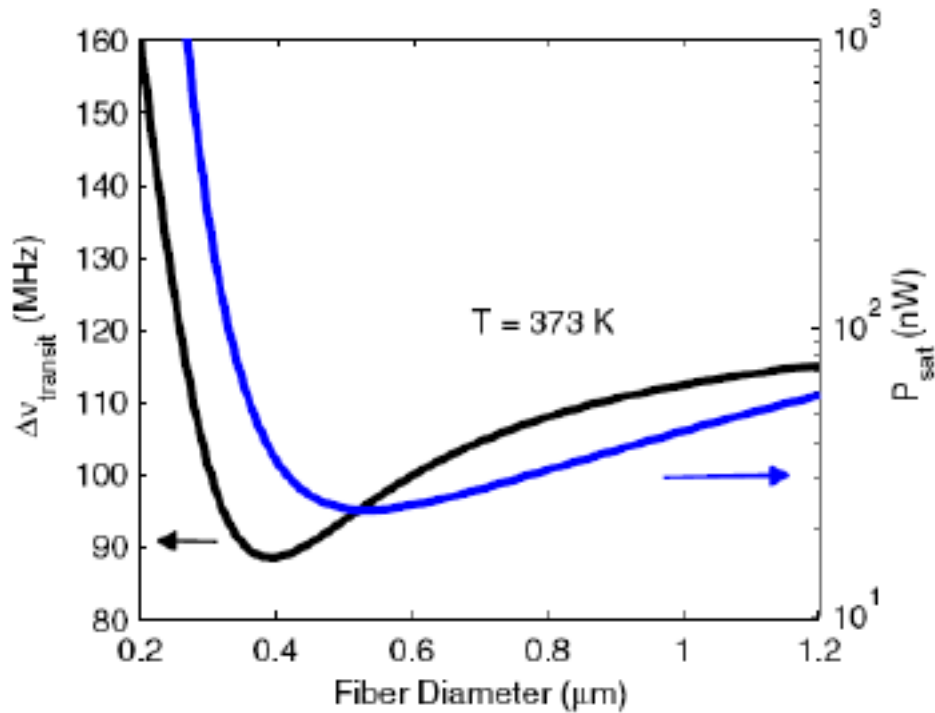


Figure 2.3 Transit time linewidth (black) and Saturation power (blue) versus fiber diameter

Taper Fabrication

The tapered fibers are fabricated from Thorlabs 780HP single mode (at 780 nm) fiber. The first step is to strip a small section of acrylic coating off of the center of a fiber. The fiber is then placed into two Newport magnetic fiber clips, which are firmly attached to two motor driven pulling stages. The stripped section is centered between the two pulling stages, directly over a hydrogen oxygen torch which is also fixed to a motion control stage. Using a program in MATLAB, the motion of the torch and pulling stages can be

controlled directly by the computer. Once the torch is lit and the program is initiated, the two pulling stages move apart from one another as the torch moves back and forth under the stripped section. As the pulling stages move further apart from one another, the glass of the heated fiber melts and the fiber adiabatically reduces in diameter. This pulling continues until the diameter at the center of the fiber is approximately 500 nm.

During the tapering process, laser light may be coupled into the fiber, and a photo detector can be used to measure the transmission efficiency as the fiber is pulled. Several factors can influence the optical transmission such as flame size, pulling speed, and torch speed. Also, since the evanescent mode is guided in air outside the fiber, any dust that falls on the tapered section will dramatically reduce transmission. A high magnification camera is also used to watch the pulling process. When the fiber diameter is comparable to the wavelength of light, bands of color may be seen on the fiber due to interference effects, similar to those seen on oil droplets. The variation of color over the length of the tapered section corresponds to variation in fiber diameter.

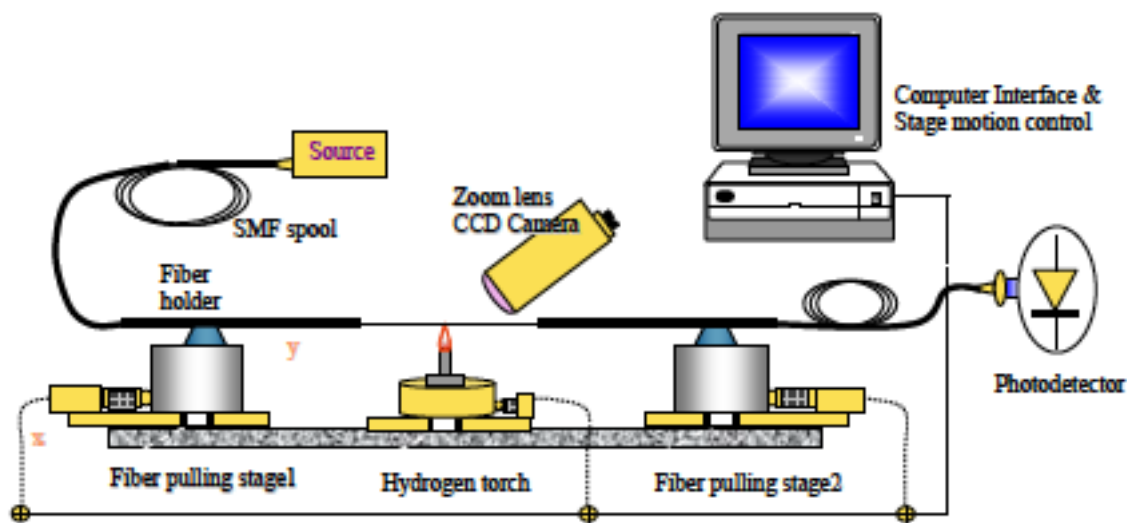


Figure 2.4 *TNF fabrication apparatus*

Below is a picture from a Scanning Electron Microscope of the tapered section of a TNF. Since there was no vibration isolation, the picture shows oscillations in the

suspended fiber due to the mechanical pump used to evacuate the SEM. Nevertheless, we see that the diameter is approximately 400 nm.

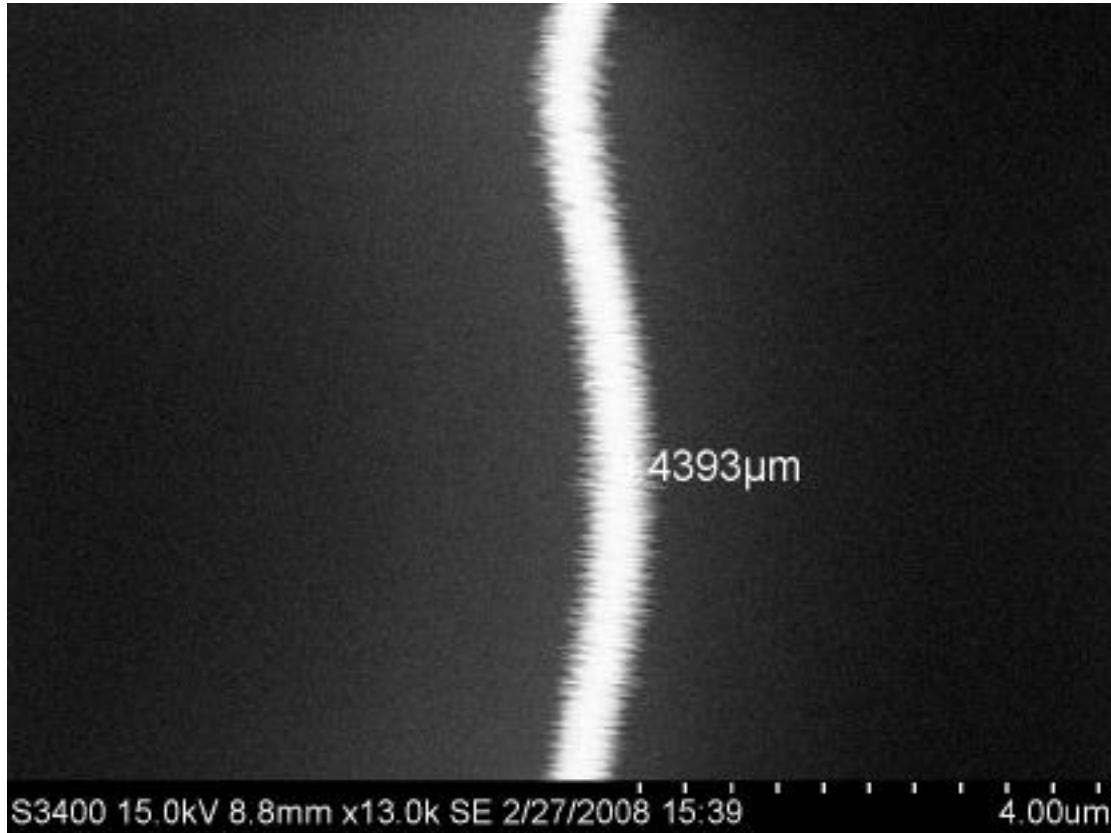


Figure 2.5 *Image of tapered fiber taken from an SEM*

Installation in Vapor Cell

Switching in TNF has been proposed in atomic vapor as well as cold atoms. A separate apparatus was necessary for each method. The system for switching in vapor is illustrated below.

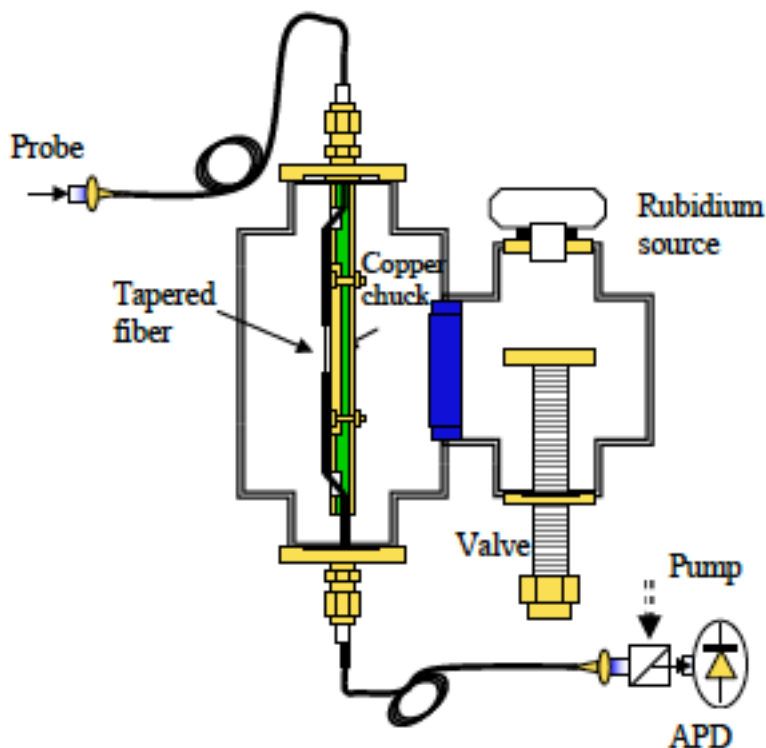


Figure 2.6 Rubidium vapor cell for TNF experiment

The vapor cell consists of two sections, one that houses the fiber and one that contains a Rb source. These sections are separated by a valve, and are continuously pumped by a mechanical pump to a pressure of 10 mT. The fiber is first attached to a custom made copper chuck using UV curable epoxy. The chuck is then inserted into the vapor cell from the top. Custom made Teflon ferrules¹⁴ mounted into Swagelok connectors are drilled through the center with a number 80 drill bit so that the fiber slips through. When the Swagelok connector is tightened, the ferrules are forced down and compressed to form a tight seal around the input and output of the fiber in order to keep air out of the system.

To vaporize the Rb, the reservoir holding the Rb is heated to a temperature of 150 °C . In order to minimize the amount of Rb condensing on the cell and the fiber both are heated to about 100 °C. If Rb condenses on the fiber, transmission through the fiber will decrease. Light may be coupled into the fiber, and monitored at the output with an APD.

One experiment, discussed later, employs cross-polarized counter-propagating beams in the fiber achieved by coupling a probe into one end of the fiber, and a pump into the other end. A polarizing beam splitter is used to separate the beams, and send the probe beam to the APD.

Saturated Absorption in a Tapered Nanofiber

A diagram of the experiment is shown below.

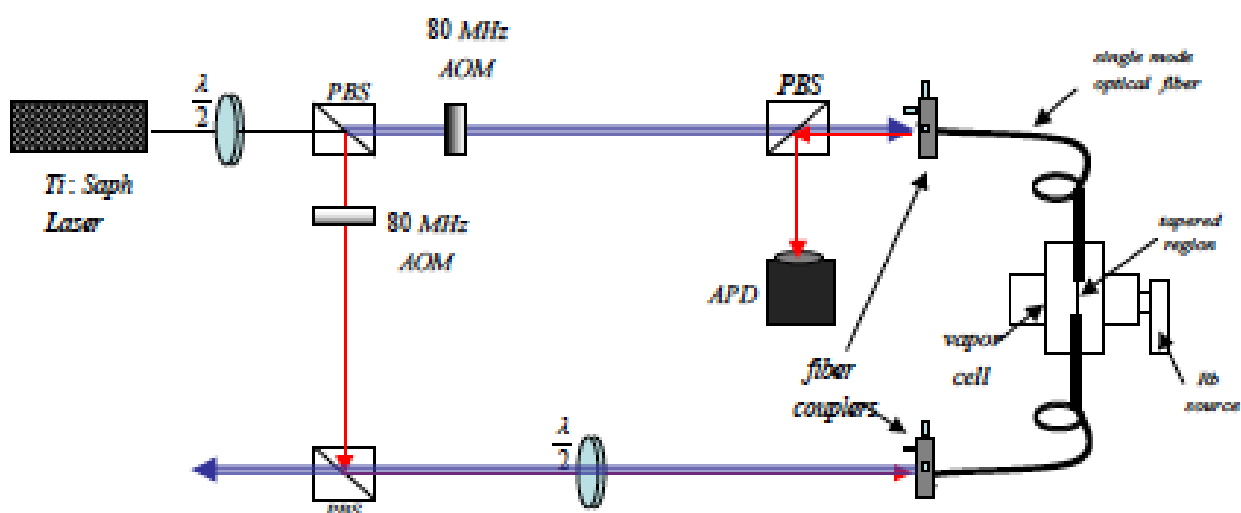


Figure 2.7 Apparatus for observing V-type EIT in a TNF embedded in an Rb vapor cell

In our experimental setup [illustrated above], a TNF was inserted into a chamber containing hot rubidium vapor, which contained a natural mixture of Rb85 and Rb87 isotopes. A Newport single-mode fiber at 780 nm was drawn adiabatically into a TNF with a waist diameter of approximately 400 nm using the “flame-brush” technique¹⁵ with a hydrogen-air torch. The resulting taper profile is nearly exponential with a $1/e$ length of ~ 3 mm. During the adiabatic tapering process, monitoring of fiber transmission showed negligible loss (ranging from 1%–10%) for final taper waist diameters of approximately 400 nm.

The TNF is mounted to a copper chuck using UV-curable epoxy and inserted into the vacuum chamber using a set of Teflon fiber feedthroughs, which maintain fiber continuity into and out of the vacuum chamber. A gate valve isolates the optical fiber during loading or unloading from a rubidium metal source. During experiments, the vacuum chamber was heated to 100 °C (to minimize Rb condensation), and Rb vapor was created by heating the source region to 200 °C, with the chamber pressure maintained at 5 mTorr by a roughing pump. For these measurements, we made no attempt to prevent dephasing for atoms which struck the TNF. Assuming the vapor inside the chamber is at an average temperature of 100 °C, the atomic density is estimated to be 6×10^{12} atoms/cm³.

For the first set of experiments, a weak probe beam (approximately 10 nW) obtained from a Ti: sapphire laser was transmitted through the TNF, and the optical transmission was monitored with an avalanche photodiode. The frequency of the probe was scanned over the Doppler broadened spectrum of the *D2* manifold. The graph below shows the transmission spectrum through the TNF (lower spectrum), and a reference Rb vapor cell kept at 100 °C (upper spectrum).

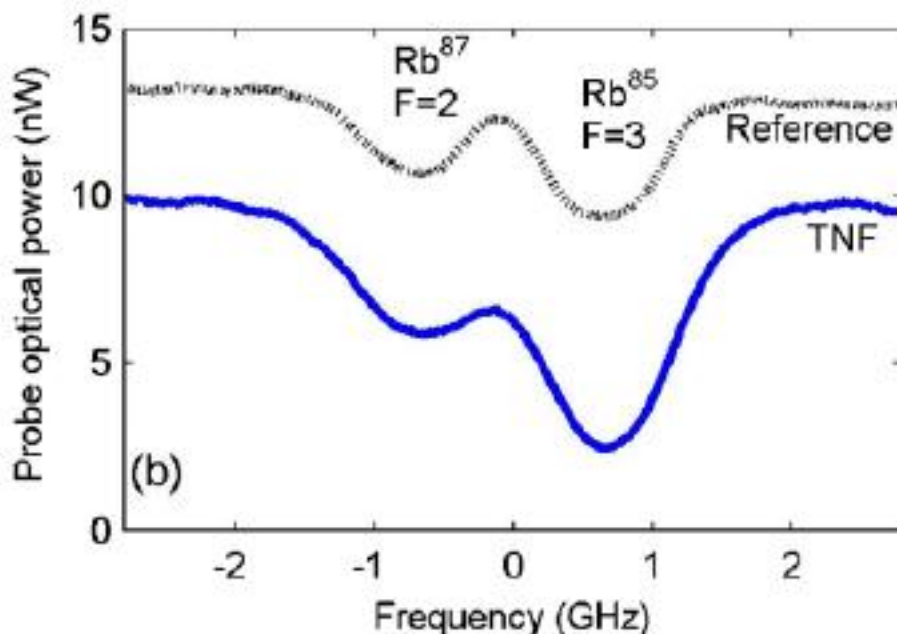


Figure 2.8 *Linear absorption measured in a vapor embedded TNF (blue) and reference cell (black)*

The dip on the left corresponds to the $F = 2$ transitions in the $D2$ manifold of Rb87, while the dip on the right corresponds to the $F = 3$ transitions in the same manifold of Rb85. Far away from resonance, the probe was found to be attenuated by about 20% due to a combination of losses at the input couplers and by TNF absorption. The data clearly show transmission dips representative of rubidium vapor absorption, with peak locations similar to that of the reference cell. However, the shape of the transmission dips for the Rb-TNF system is slightly different than that for the reference cell, which is due to both differences in Doppler broadening and transit time dephasing present in this experimental measurement.

A pump-probe measurement was performed, with the strong counter-propagating pump beam cross-polarized with respect to the probe. This measurement was performed on the $D1$ manifold in order to delineate more clearly the spectral features in the presence of large transit-time broadening. The figure below illustrates the probe transmission

spectrum (power ~ 1 nW) for counter-propagating pump powers of 10 nW (middle, green) and 30 nW (lower, red), for a TNF with a waist diameter of approximately 400 nm. For comparison, a reference trace is also shown for a conventional vapor cell (upper, blue).

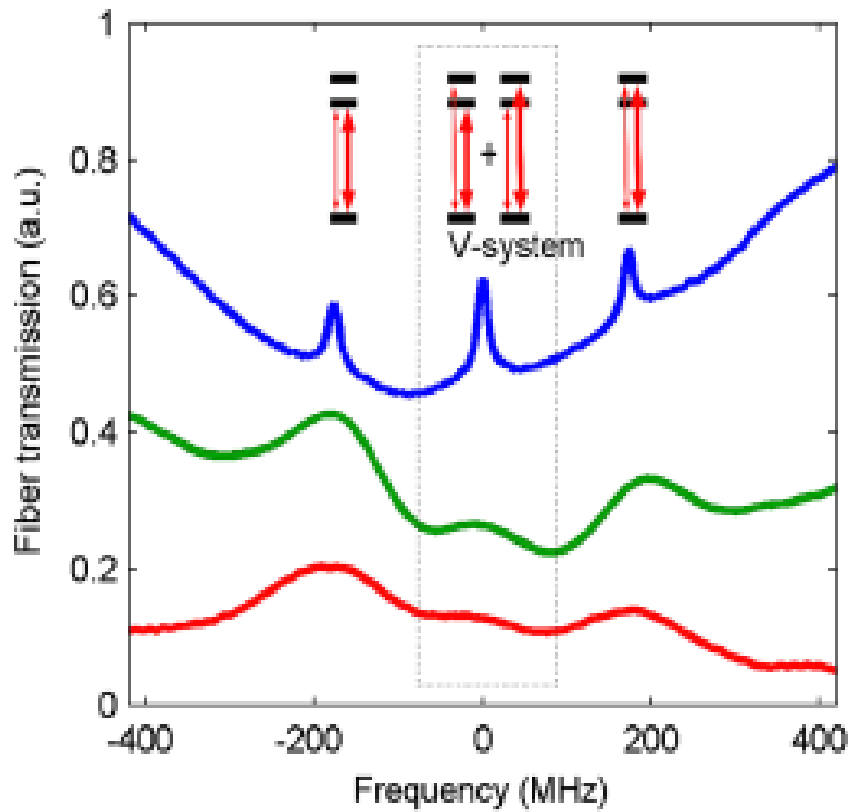


Figure 2.9 Saturated absorption observed in TNF with a probe power of 1 nW and a pump power of 10 nW (green) and 30 nW (red). Also plotted is saturated absorption in a reference cell (blue).

The peaks on the left and the right correspond to self-induced transparency (SIT) for Rb85 atoms with zero axial velocities, corresponding to the $F=3$ to $F'=2$ and the $F=3$ to $F'=3$ hyperfine transitions, respectively. This measurement is similar to that of conventional saturated absorption spectroscopy, with a V-type three level EIT peak (with orthogonally polarized pump and probe) located at the crossover resonance location.

This peak is composed of V-type EIT measurements of two groups of atoms: one with

an axial velocity such that the probe excites the $F = 3$ to $F' = 3$ transition and the pump excites the $F = 3$ to $F' = 2$ transition, and the other with an equal but opposite axial velocity so that the probe excites the $F = 2$ to $F' = 3$ transition and the pump excites the $F = 3$ to $F' = 2$ transition. The EIT signal for the TNF is readily apparent for the lower pump power measurement, where the peak is clearly separated from the SIT peaks. The amplitude of this peak is measurably greater than the background signal for both the low and high power spectra, even though the high power spectrum is less resolvable due to power broadening.

For the conventional vapor cell, the transparency seen at the EIT resonance is larger than that at the SIT peaks due to the larger number of atoms in the combined 180 MHz Doppler-shifted groups (there is approximately 1.5 times the number of atoms in an isotropic vapor cell, which arises from the width of the Doppler distribution) than the individual zero axial velocity groups. Furthermore, the peak widths are the power-broadened individual hyperfine transitions (~ 6 MHz power broadened to ~ 18 MHz). However, for the TNF signal, there is a noticeable difference between the linewidths and relative amplitudes of the SIT and EIT peaks. Here, the line broadening for the lower (middle) power curve is due primarily to the transit-time effect. The transit-time broadening is about 110 MHz, close to the theoretical prediction. The dramatically smaller amplitude of the V -system EIT peak in the TNF measurement is likely due to a nonisotropic atomic velocity distribution in the Rb-TNF cell, which leads to a smaller population of atoms with the correct longitudinal Doppler shifted velocity component for the EIT interaction. The relative magnitude of the three absorption peaks is consistent with a 210 MHz wide effective Doppler distribution. The effective reduction of the Doppler width may be attributable to the geometry of the cell and the relative position of the TNF and the vacuum pump. Further investigation will be carried out in the future to study this effect.

V-system modulator in TNF

The experimental setup is summarized in Figure 2.10. The output of a Ti:Sapphire laser was split by a 50/50 non-polarizing beam splitter. The beam reflected by the splitter was shifted up by 80 MHz with an acousto-optic modulator (AOM), to produce the S-polarized probe beam. The beam passing through the splitter was up-shifted by a second AOM, also at 80 MHz, to produce the pump beam, which was P-polarized by passing through a half-wave plate. Attenuators (not shown) were then used to reduce the power in both beams independently. The pump and probe were combined on a polarizing beam-splitter (PBS), and coupled into the TNF. The output was passed through another PBS, separating out the pump and the probe. The probe was then detected with an avalanche photo-diode (APD). Using another non-polarizing beam splitter, 10% of the probe beam (before attenuation) was diverted to a vapor cell for saturated absorption spectroscopy. Signal from this cell was used to lock the laser to a hyperfine transition.

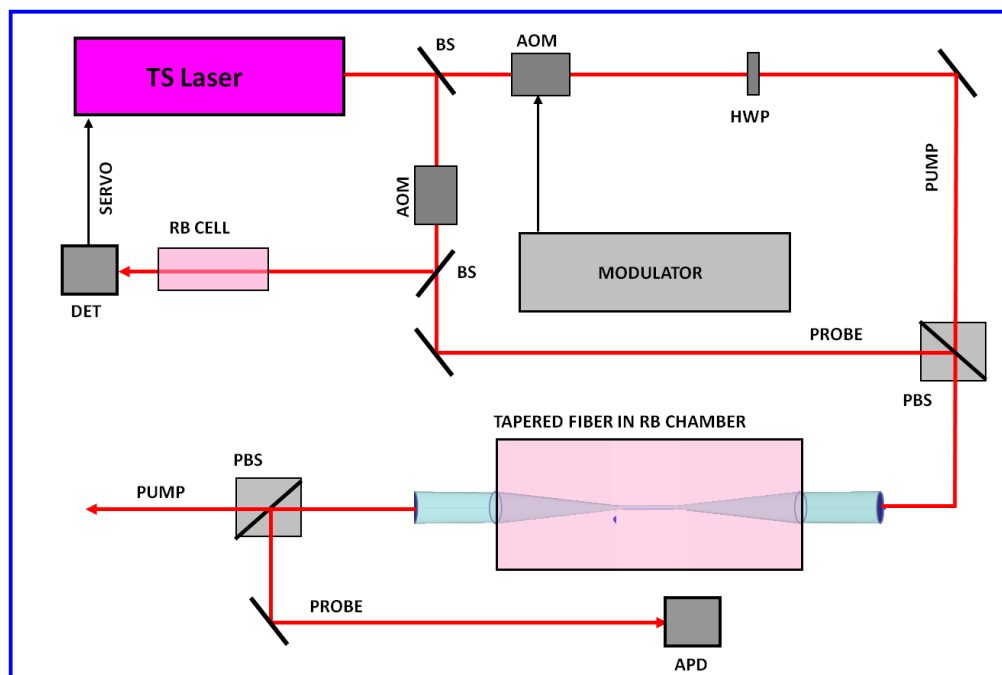


Figure 2.10 Experimental setup for demonstrating optical modulation. Both AOMs are operated at the same frequency (80 MHz). The pump and the probe are each linearly polarized, orthogonal to each other.

Figure 2.11 shows one set of data taken using this setup. The probe (pump) power was 100 pW (40 nW). First, the red trace shows the probe transmission when the pump beam is turned off. As the probe frequency was scanned across the D1 manifold, three dips were observed. The biggest dip corresponds to the transition from the $5S_{1/2}$, $F=3$ ground-state in ^{85}Rb to the $5P_{3/2}$ hyperfine levels, which are not resolved because of Doppler broadening. The small dip on its left corresponds to a transition in ^{87}Rb , from $5S_{1/2}$, $F=2$ ground-state to the $5P_{3/2}$ hyperfine levels. The dip on its right corresponds to the transition from the $5S_{1/2}$, $F=2$ ground-state in ^{85}Rb to the $5P_{3/2}$ hyperfine levels. The

scan range was not long enough to see the other transition in ^{87}Rb : from $5\text{S}_{1/2}$, $F=1$ ground-state to the $5\text{P}_{3/2}$ hyperfine levels.

Next, the blue trace shows the probe absorption when the pump is turned on. There is a strong increase in the probe transmission at the center of the $F=3$ transition (the middle one in Fig. 2.11). The physical mechanism behind the strong modulation of the probe transmission caused by the pump can be explained as follows. Consider first the Zeeman sublevel of the $m_F=0$ in the $F=3$ ground-state, and how it is coupled to the $F'=2$ excited state. The probe, which is a superposition of left and right circularly polarized light, with a relative phase ψ , would couple this state to $m_F=-1$ and $m_F=1$ sublevels in the $F'=2$ state. The pump is also a superposition of left and right circularly polarized light, with a relative phase ϕ , and would excite the same pair of transitions.

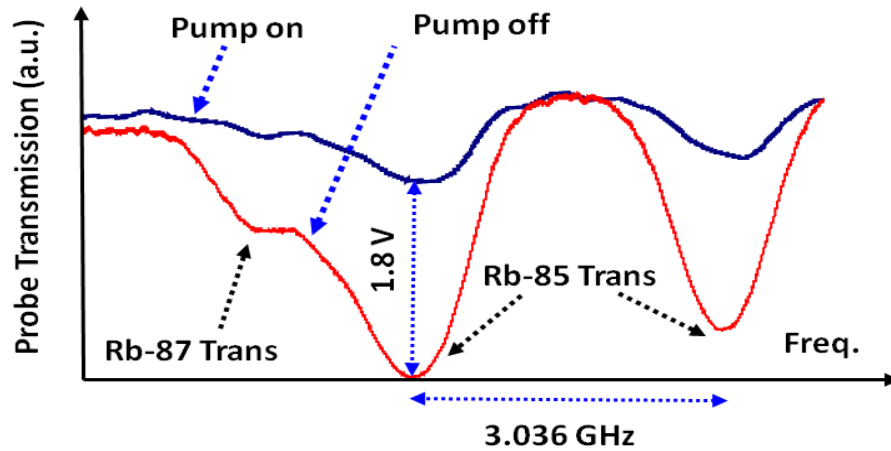


Figure 2.11 Absorption spectrum of the probe in the absence (red) and presence (blue) of the pump.

However, the phases ψ and ϕ differ by π . As such, the net interaction can be represented as a V-system, with one leg excited by the probe and the other by the pump. This is illustrated in Figure 2.12. Here, the in-phase superposition state ($|p\rangle$) is coupled to the ground state $|a\rangle$ by the P-polarized pump beam only, and the out-of-phase superposition state ($|n\rangle$) is coupled to the ground state $|a\rangle$ by the S-polarized probe beam only. Thus, the net interaction is equivalent to the V-system. Specifically, in the absence of the pump, the probe excites state $|a\rangle$ to state $|n\rangle$, corresponding to strong absorption. However, when the pump is present, the effective continuous measurement process keeps the atoms locked in state $|a\rangle$, thus reducing strongly the absorption of the probe beam.

It should be noted that when the pump is turned on, the residual probe absorption develops some asymmetry, and the centroid of each dip appears to be slightly shifted.

Further investigation is required to elucidate the origin of these effects, and will be carried out in the future. However, for the purpose of modulation, these effects may not be very important.

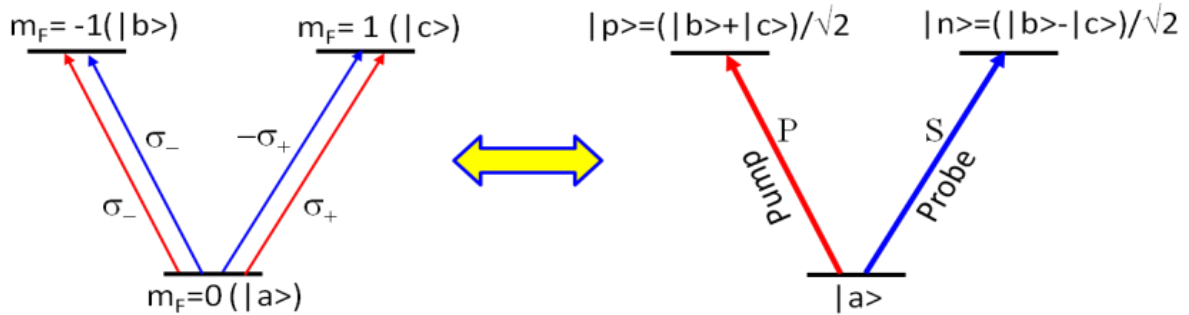


Figure 2.12 Schematic illustration of the process that produces the QZE when the atoms are excited by cross-linearly polarized pump and probe beams.

A more quantitative description of the process makes use of the concept of level splitting, as also described in the introduction. Specifically, when the pump is turned on, the ground state gets split into two dressed states, each out of resonance for the probe if the pump intensity is greater than the saturation intensity of the isolated atom (i.e., $\Omega > \Gamma$, where Ω is the pump Rabi frequency, and Γ is the natural linewidth). When the Doppler broadening is taken into account, the condition for probe transparency is that $\Omega > \sqrt{\Gamma * \Gamma_D}$, where Γ_D is the half-width of the Doppler broadening. This condition is satisfied by the pump power (~ 40 nW) used. The same model applies to transitions to the $F=3$ and $F=4$ excited states as well. Of course, for some values of m_F , only left (right) circular transition is allowed; in that case, the system behaves as a pure two level transition,

excited by identically polarized parts of the pump and the probe. The reduction in probe transmission for these sublevels is due to the conventional self-induced transparency.

Figure 2.13 shows results of pulsed modulation, with the laser locked at the center of the $F=3$ transition. The probe is kept constant at 100 pW, while the pump intensity is modulated by using the pump AOM. The top left panel shows the probe transmission when this modulation is at 10 Hz. The other three panels show the same for increasing modulation frequencies. At 10 KHz, the probe transmission deviates from the square profile, due to the limited bandwidth (~ 50 kHz) of the APD.

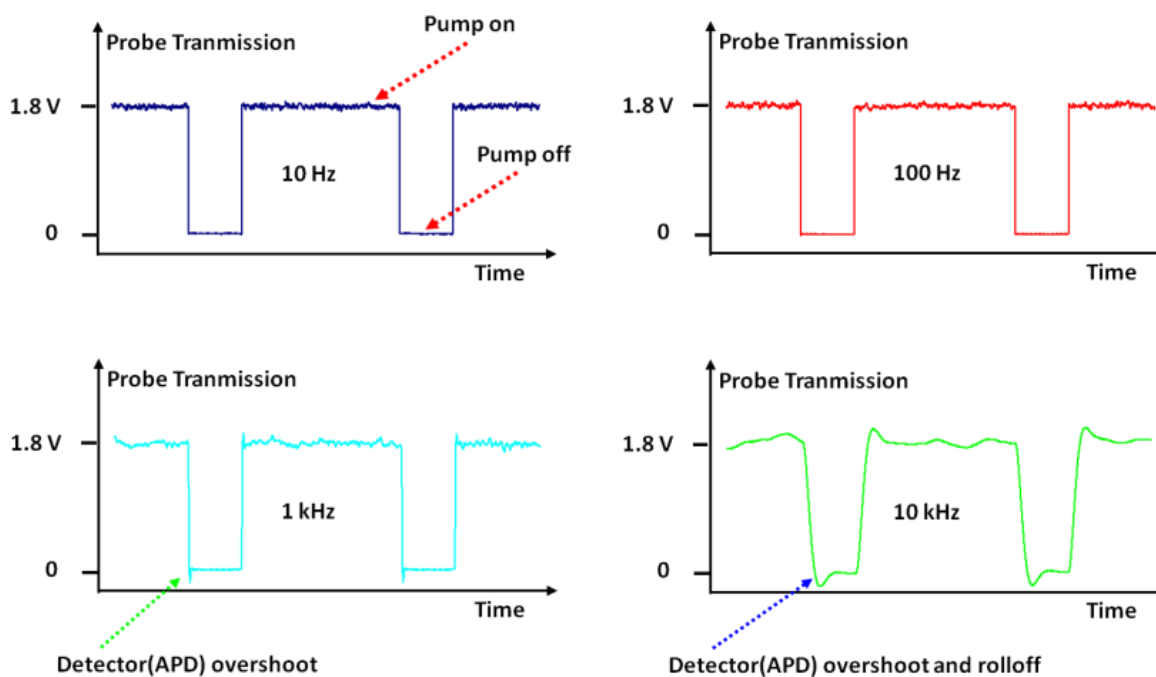


Figure 2.13 Low-frequency modulation results for a duty cycle of 70% (on-state), for four different frequencies. At 10 kHz, the signal is limited by the APD bandwidth.

A careful consideration of the physical mechanism behind this modulation reveals that the modulation speed is fundamentally limited by the time needed for the atoms to repopulate the ground state, $|a\rangle$, after the pump is turned off, so that they can absorb the probe again. This means that the modulation bandwidth cannot exceed the homogeneous linewidth (HL). For the TNF system, the HL is dominated by the transit time broadening, which is about 100 MHz, as shown in ref. 5. The HL can be increased very significantly by adding a buffer gas, such as ^4He . In a series of studies carried out in the context of the development of diode pumped alkali lasers (DPALs), it has been shown that the atoms excited to the $5P_{3/2}$ state relaxes very rapidly to the $5P_{1/2}$ state. The rate of relaxation from the $5P_{1/2}$ state to the ground state can be augmented by adding an auxiliary, strong

beam that would be turned on and at the same time as the pump is turned off, and turned off before turning on the pump again. For buffer gas pressure of 1 atm, the HL is about 10 GHz. A HL linewidth as large as 500 GHz is possible in the presence of a buffer gas pressure of 25 atm. Of course, the intensity needed to saturate a 500 GHz broadening would be too hard to realize in a TNF. However, based on a typical DPAL laser in Rb, which requires a threshold pump intensity of about $15 \mu\text{W}/\mu\text{m}^2$, a pump power of about $3 \mu\text{W}$ should be enough to achieve the 10 GHz modulation bandwidth in the TNF, which has a mode area of only $0.2 \mu\text{m}^2$. The same level of power would be needed for the auxiliary pump beam for rapid depopulation of $5P_{1/2}$ state to the ground state.

CHAPTER 3 LADDER SYSTEM & MODULATOR

As shown in Figure 3.1 the system consists of three states: a ground state ($|1\rangle$), a strongly-damped intermediate state ($|2\rangle$), and a third state ($|3\rangle$) which may or may not be strongly damped. The control beam couples $|1\rangle$ to $|2\rangle$, and the probe beam couples $|2\rangle$ to $|3\rangle$. For resonant excitation, the corresponding dressed states (defined as products of photon number states and atomic states) are degenerate, as shown in Fig. 3.1(b). When the coupling between $|1\rangle$ and $|2\rangle$ is strong, the resulting states, upon diagonalization ($|+\rangle$ and $|-\rangle$) are split by an amount equaling the Rabi frequency of the $|1\rangle$ to $|2\rangle$ transition, which is much larger than the natural linewidth of $|3\rangle$, as illustrated in Fig. 3.1(c).

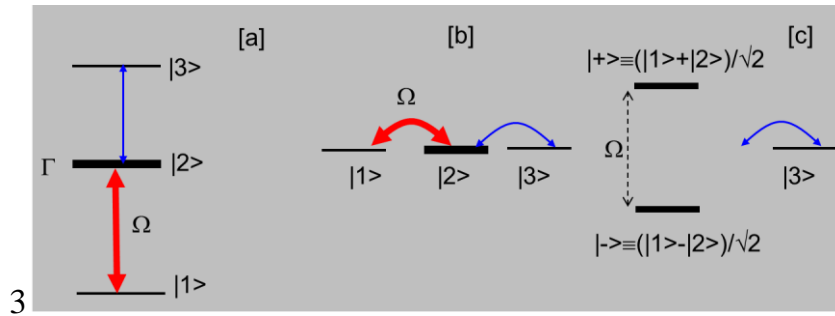


Figure 3.1 AC-Stark effect in a Ladder Transition: (a) The control beam couples $|1\rangle$ to $|2\rangle$, and the probe beam couples $|2\rangle$ to $|3\rangle$; (b) For resonant excitation, the corresponding dressed states are degenerate; (c) When the strong control beam coupling is diagonalized, the resulting states are split by an amount much larger than the natural linewidth of $|2\rangle$.

There are several combinations of parameters that can be considered for controlling the probe absorption. Consider first Case I, where the probe is resonant for the $|2\rangle$ to $|3\rangle$ transition, but the pump is relatively weak, so that the two diagonalized states ($|+\rangle$ and $|-\rangle$) are not resolved. In this case, the probe is transparent when the pump is not present (since the atoms remain in state $|1\rangle$), and is absorbed when the pump is turned on. Consider next Case II where the pump is strong so that the two diagonalized states are clearly resolved, but the probe is detuned from the $|2\rangle$ to $|3\rangle$ transition (positively or negatively) by half the separation between the two diagonalized states. In this case, the probe is absorbed in the presence of the pump, but is transparent when the pump is not present. This is the same as what happens for Case I, but for different reasons. Finally, consider Case III, where again the pump is strong so that the two diagonalized states are clearly resolved, but the probe is resonant for the $|2\rangle$ to $|3\rangle$ transition (as shown in Fig. 3.1). In this case, the probe is transparent both in the presence and in the absence of the pump. Cases I and II can be considered to be QZE-based control of probe absorption,

since the mechanism in each case can be interpreted in terms of AC-Stark effects. We describe experimental results based on Case I, while the scheme we describe for high speed modulation in the presence of buffer gas is based on Case II.

a. Experimental set-up

In this section, we describe our experiment for realizing a Case I type QZE modulator in a conventional vapor cell of length ~ 7.5 cm, under free space propagation of light. The experimental configuration is illustrated schematically in Fig. 3.2. Briefly, beams from two tunable lasers (Ti-Sapphire laser at 795 nm, and a fiber laser at 1323 nm) are combined with a dichroic mirror (DCM). Both the control and the signal beams are co-propagating, and linearly polarized in the same direction. A part of the 795 light is sent to a reference vapor cell for saturated absorption spectroscopy and locking. The combined beams are sent through a vapor cell, shielded from magnetic fields with μ -metal. The cell is heated to temperatures of about 150 C using bifilarly wound wires that do not add any magnetic fields. Experimentally, we estimated the optical depth for the strongest transition ($5S_{1/2}, F=2, mF=2$ to $5P_{3/2}, F=3, mF=3$) on the D2 line to be ~ 220 , corresponding to an atomic density of $\sim 10^{10}$ cm $^{-3}$. After passing through the cell, another DCM is used to split the light into two parts, and the signal at each frequency is monitored with a separate detector.

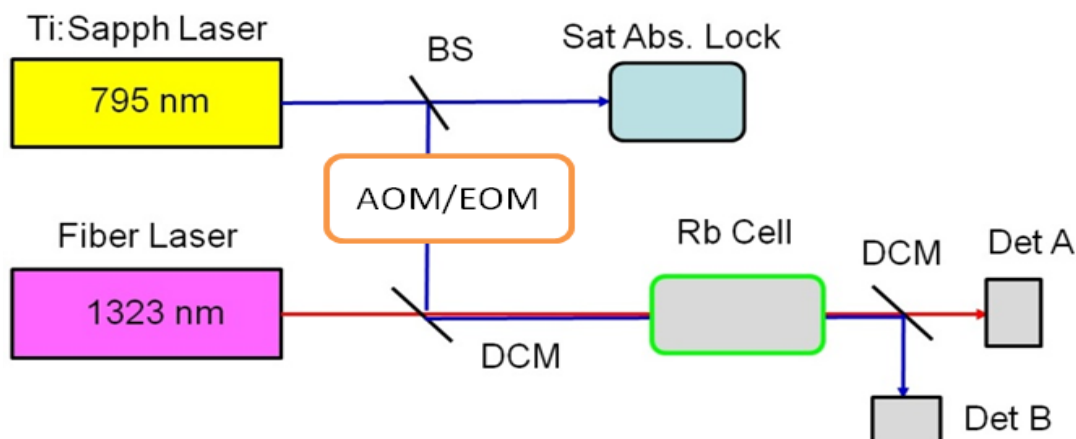


Figure 3.2 Schematic illustration of the experimental setup for observing the ladder-transition based QZE modulator. DCM: Dichroic mirror, AOM: Acousto-Optic modulator, EOM: Electro-Optic modulator, BS: Beam Splitter

The acousto-optic modulator (AOM) and the electro-optic modulator (EOM) shown in Fig. 3.2 are used only while performing the actual modulation, and are removed while characterizing the absorption profile at 1323nm. While performing spectroscopic measurements and switching at low frequencies (up to ~ 5 MHz), we used Thorlabs PDA55 and Thorlabs PDA400 for detecting light at 795nm and 1323nm respectively. For high frequency switching, (where the use of EOM necessitated low control beam power), an APD was used for detection of 1323nm light while the 795nm light was not monitored on a detector-the switching input applied to the EOM was used as reference.

b. Spectroscopic details

We chose to use the $5S_{1/2} \rightarrow 5P_{1/2} \rightarrow 6S_{1/2}$ ladder transition in Rb for our experiment, dictated in part by lasers readily available to us. Using the reference saturated absorption cell, we locked the pump laser (795 nm) to one of the resonances of the $5S_{1/2} \rightarrow 5P_{1/2}$ manifold and the probe laser (at 1323nm) was then scanned across the $6S_{1/2}$ manifold over a few GHz. The modulator should work just as well if the ladder transition is of the type $5S_{1/2} \rightarrow X \rightarrow Y$, where X is $5P_{1/2}$ or $5P_{3/2}$, and Y can be one of many states that are coupled to the X states via optical dipole transitions and has a higher energy than that of X. For example Y can be $7S_{1/2}$, $4D_{3/2}$, $4D_{5/2}$, $5D_{3/2}$, $5D_{5/2}$, and so on.

Figure 3.3(a) shows the spectroscopic details of the ladder transition for ^{85}Rb . The probe beam was scanned over the $6S_{1/2}$ manifold while the control beam was locked to the $F=2 \rightarrow F=2$ transition on the lower leg. The separation between the hyperfine levels in the $5P_{1/2}$ manifold (~ 360 MHz) is less than the Doppler linewidth (~ 600 MHz). Hence, atoms are excited to both hyperfine levels of the $5P_{1/2}$ manifold even if the 795nm laser is locked to only the $F=2 \rightarrow F=2$ transition. As a result, it is expected that 4 lines would be observed for the 1323nm absorption (upper leg) as this laser is scanned over a few GHz (Fig. 3(b)). However, it is to be noted that, due to Doppler shift, the atoms excited to the $F=3$ state of the intermediate level correspond to negative velocity (with respect to the direction of propagation of the 795 nm laser beam) atoms, and not zero velocity atoms. Thus, the transitions from this state to the $6S_{1/2}$ manifold are shifted to lower frequencies by an amount equal to the separation between the hyperfine states in the $5P_{1/2}$ manifold

(~ 360 MHz). In the case of ^{85}Rb , the frequency difference between the hyperfine states in the $6S_{1/2}$ manifold (~ 710 MHz) is such that this shift causes the $F=2 \rightarrow F=2$ transition almost to overlap the $F=3 \rightarrow F=3$ transition, for the 1323 nm beam. As a result, only 3 lines are expected to be observed distinctly (see Fig. 3.3(c)). It is to be noted that Fig. 3.3(b) and 3.3(c) only illustrate the expected relative positions of the ^{85}Rb absorption lines (at 1323nm), and not the actual observed data, which are described next.

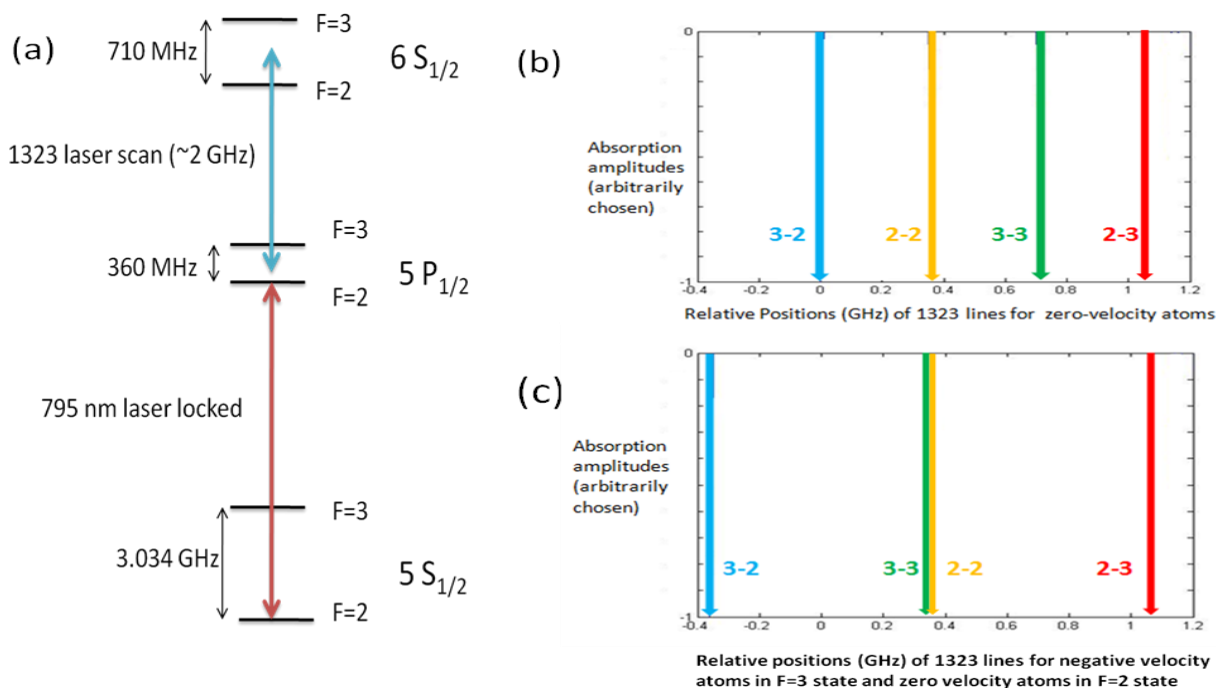


Figure 3.3 Spectroscopic details of ladder transition in ^{85}Rb (a) Schematic of various hyperfine levels used, along with the transition frequencies. (b) Expected spectrum if both hyperfine states of intermediate level are occupied by zero velocity atoms. (c) Shift of spectrum in (b) due to $F=3$ state at the intermediate level being occupied by negative velocity atoms

Figures 3.4(a) and 3.4(b) show a couple of typical profiles that were observed for ^{85}Rb . The data in Fig. 3.4(a) corresponds to a relatively low power (~ 2 mW) of the control beam, and only three absorption lines are observed, in keeping with the explanation provided in Fig. 3.3 above. The relative separation between the lines is in good agreement with the expected spectrum, as illustrated in Fig. 3.3(c). This data has been taken in AC mode (on a standard digital oscilloscope) and hence shows negative values. The slow background modulation seen in the signal is most likely due to the etalon effect from the windows of the cell. The data in Fig. 3.4(b), taken in DC mode, corresponds to much higher power (~ 200 mW) of the control beam, and we see almost complete absorption of the probe while the lines are strongly power broadened. Of course, the amount of 1323nm absorption increases with the number of atoms excited to the intermediate leg, which in turn is determined by the power of the control beam. Thus at sufficiently high power of the control beam, the upper transition is completely saturated. It should be noted that even in this case, the pump power is not high enough to correspond to Case II, since the power broadening is less than the effective width of the intermediate state (~ 600 MHz) due to Doppler broadening.

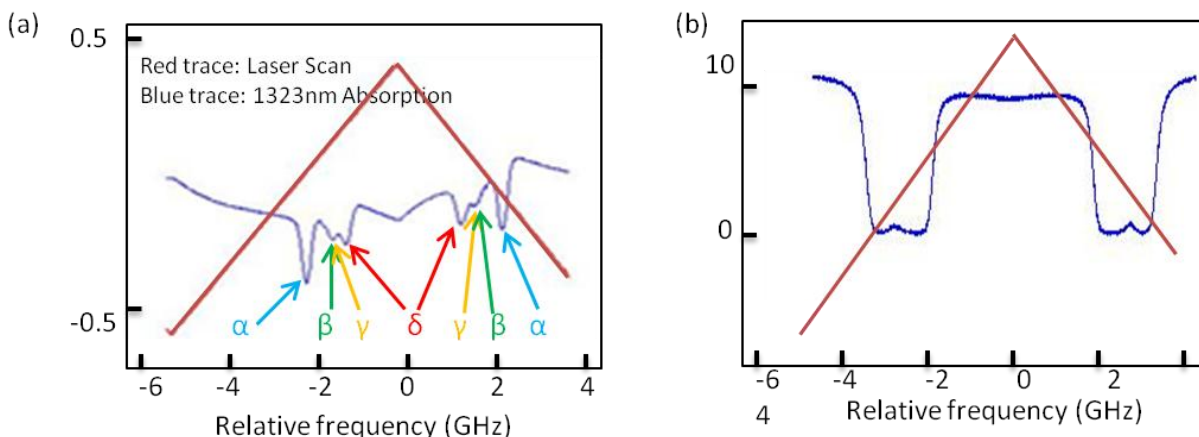


Figure 3.4 Typical absorption profiles for the ladder transitions (at 1323nm) that are observed in ^{85}Rb . (a) Corresponds to 795 nm laser power $\sim 2\text{mW}$, data taken in AC mode. The hyperfine transitions corresponding to the absorption dips are α : $3 \rightarrow 2$, β : $3 \rightarrow 3$, γ : $2 \rightarrow 2$, δ : $2 \rightarrow 3$. The repeat scan has been shown due to the asymmetry of the signal (b) Corresponds to 795 nm laser power $\sim 200\text{mW}$, we see near 100% absorption and the lines are highly power broadened. Note that the null value of the probe detuning is defined arbitrarily to be at the turn-around point of the scan in each case.

Figure 3.5 shows the spectroscopic details for ^{87}Rb and a few typical absorption profiles that were observed at 1323nm. The control laser was locked to the $F=1 \rightarrow F=1$ transition on the lower leg as shown in Fig. 3.5(a). For moderately high powers ($\sim 50\text{mW}$) of the control beam, atoms get excited to both hyperfine levels of the $5P_{1/2}$ manifold, due to power broadening of the $5S_{1/2} \rightarrow 5P_{1/2}$ transition. At these powers, we can clearly resolve 4 absorption lines, as shown in Fig. 3.5(b). It is worth noting that each of the lines is control-power-broadened because of the fact that a significant number of velocity groups are excited to both hyperfine states of the intermediate level due to the relatively high power of the control beam. At sufficiently low powers of the control beam ($\sim 0.5\text{mW}$), two of the four lines are almost completely suppressed, and each individual

line can be seen as a narrow sharp line, as illustrated in Fig. 3.5(c). It is well known that the upper-leg is not Doppler broadened, and the spectra reported here are consistent with this feature of a ladder transition.

As before, the data in Fig. 3.5(b) and Fig. 3.5(c) have been taken in AC mode on a standard digital oscilloscope, and hence show negative values. The slow background modulation observed in both figures is again most likely due to the etalon effect of the Rb cell window, as mentioned previously. It should be noted that ladder transitions of this type have been studied previously, theoretically as well as experimentally^{16,17,18} in different contexts. The Doppler-free nature of the upper leg of the ladder transition in the co-propagating configuration is consistent with the theoretical model presented in ref. 16, and the experimental results presented in refs. 17 and 18. The hyperfine splitting frequencies we have observed for the $5P_{1/2}$ to $6S_{1/2}$ transition for both ^{85}Rb and ^{87}Rb are in agreement with those reported in ref. 16. However, the experiment reported in ref. 16 did not show any absorption lines for this transition; therefore, a quantitative comparison of the spectral response is not possible. Finally, the accidental near-degeneracy we have observed between the $F=3 \leftrightarrow F=2$ and $F=2 \leftrightarrow F=2$ transitions on the upper leg in the case of ^{85}Rb due to contributions from different velocity groups (as illustrated in figure 3.3 c and figure 3.4a) has not been reported in any of these references.

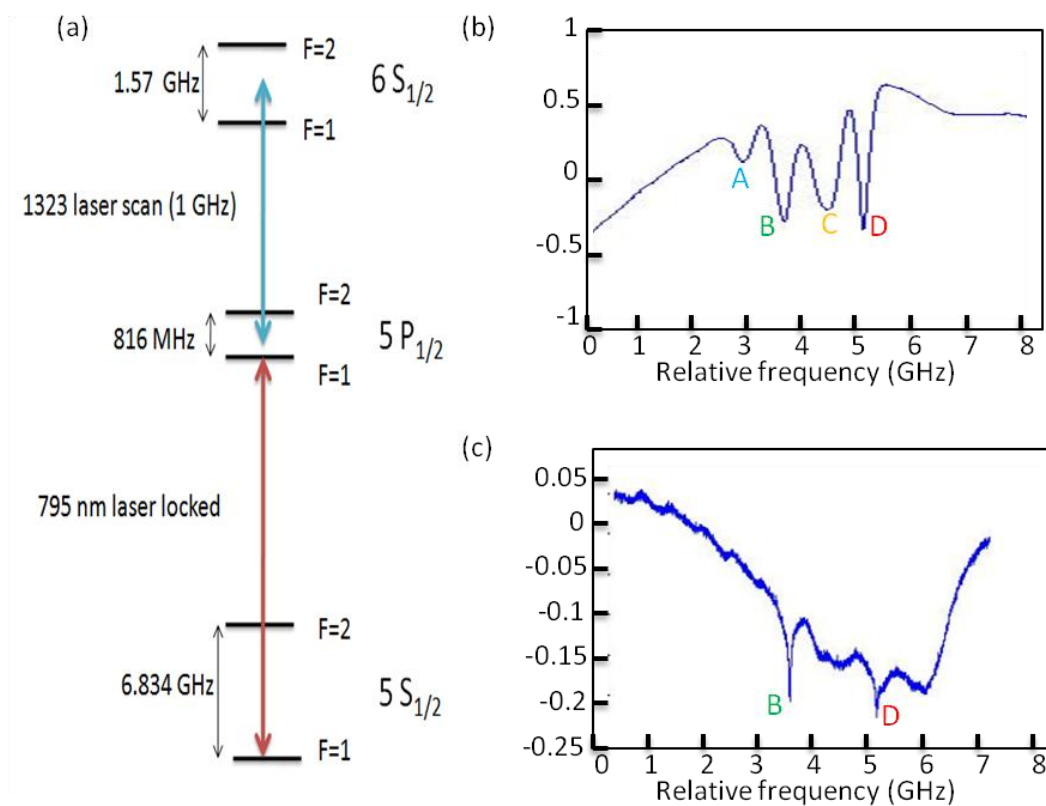


Figure 3.5 Spectroscopic details of ladder transition in ^{87}Rb (a) Schematic of various hyperfine levels used along with the transition frequencies. (b) Absorption corresponding to 795 nm laser power $\sim 50\text{mW}$; all four transitions can be clearly seen. The hyperfine transitions corresponding to the absorption dips are A: $2 \rightarrow 1$, B: $1 \rightarrow 1$, C: $2 \rightarrow 2$, D: $1 \rightarrow 2$. (c) Corresponds to 795 nm laser power $\sim 0.5\text{mW}$; two of the four lines are suppressed and only transitions from $F=1$ are observed.

c. Modulation

In order to demonstrate modulation, we chose to use the strongest absorption line at the upper leg of transitions, which in our case was the $F=3 \rightarrow F=2$ resonance for ^{85}Rb (due in part to the fact that in a natural mixture of Rb, 72.15 % is ^{85}Rb , and 27.85% is ^{87}Rb). Keeping the probe laser (1323 nm) parked on this resonance, we then modulated the

amplitude of the pump beam (795 nm). At low frequencies, switching of the control beam was accomplished using an AOM while for higher frequencies, an EOM configured for intensity modulation was used. The result is shown in Fig. 3.6.

For low frequencies, we used a pump power of $\sim 200\text{mW}$ and we see a strong modulation, in phase with the pump modulation, with a modulation depth of essentially 100% up to a speed of 1MHz. The modulation depths obtained while using the EOM were smaller because of the low control beam power ($\sim 2\text{mW}$) used. This was necessitated by the damage threshold ($\sim 20\text{mW}$) of the EOM used to switch the pump beam and the relatively low efficiency of the EOM ($\sim 20\%$). We have tested the modulation up to a speed of 75 MHz, and determined a 3dB bandwidth of approximately 3 MHz, as shown in Fig. 3.7. In Fig. 3.7, we have plotted the modulation amplitude at various frequencies (obtained using the EOM), normalized to the amplitude at 1MHz, where the modulation depth was essentially 100%, when obtained with the AOM.

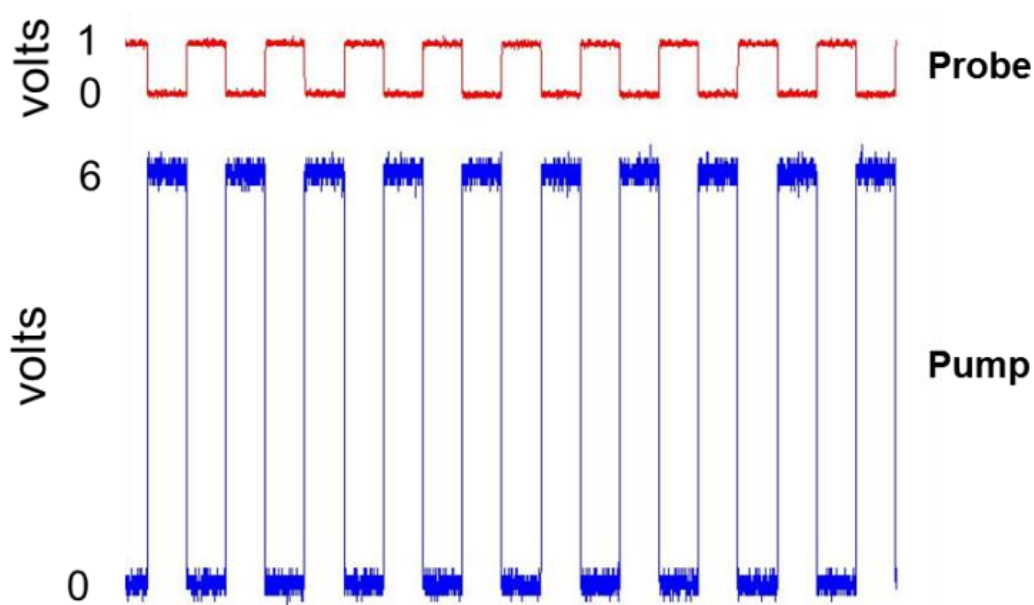


Figure 3.6 Voltage as measured by the probe and pump detectors (top and bottom respectively) at a frequency of ~ 1 MHz. The intensities are directly proportional to the voltage recorded.

A careful consideration of the physical mechanism behind this modulation reveals that the modulation speed is fundamentally limited by the time needed for the atoms to repopulate the ground state, after the pump is turned off, so that they can absorb the probe again. This means that the modulation bandwidth cannot exceed the homogeneous linewidth (HL). This constraint is rather obvious for Case I, which has been employed here. As we will discuss later, this constraint on the maximum speed also holds if Case II is employed for modulation.

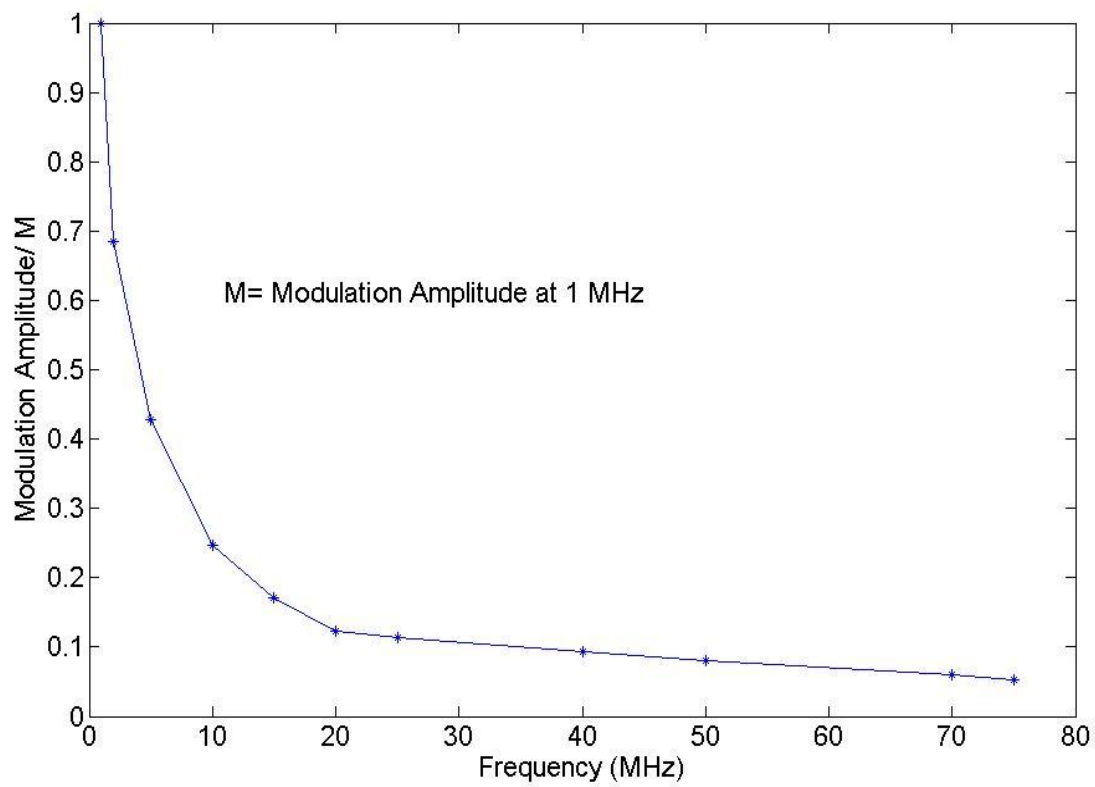


Figure 3.7 Modulation amplitude (normalized to the amplitude at 1 MHz) vs. frequency

CHAPTER 4 HIGH SPEED MODULATION

Experiment

The HL can be increased very significantly by adding a buffer gas, such as ^4He . In a series of studies carried out in the context of the development of diode pumped alkali lasers (DPALs),¹⁹ it has been shown that the atoms excited to the $5P_{3/2}$ state relaxes very rapidly to the $5P_{1/2}$ state.

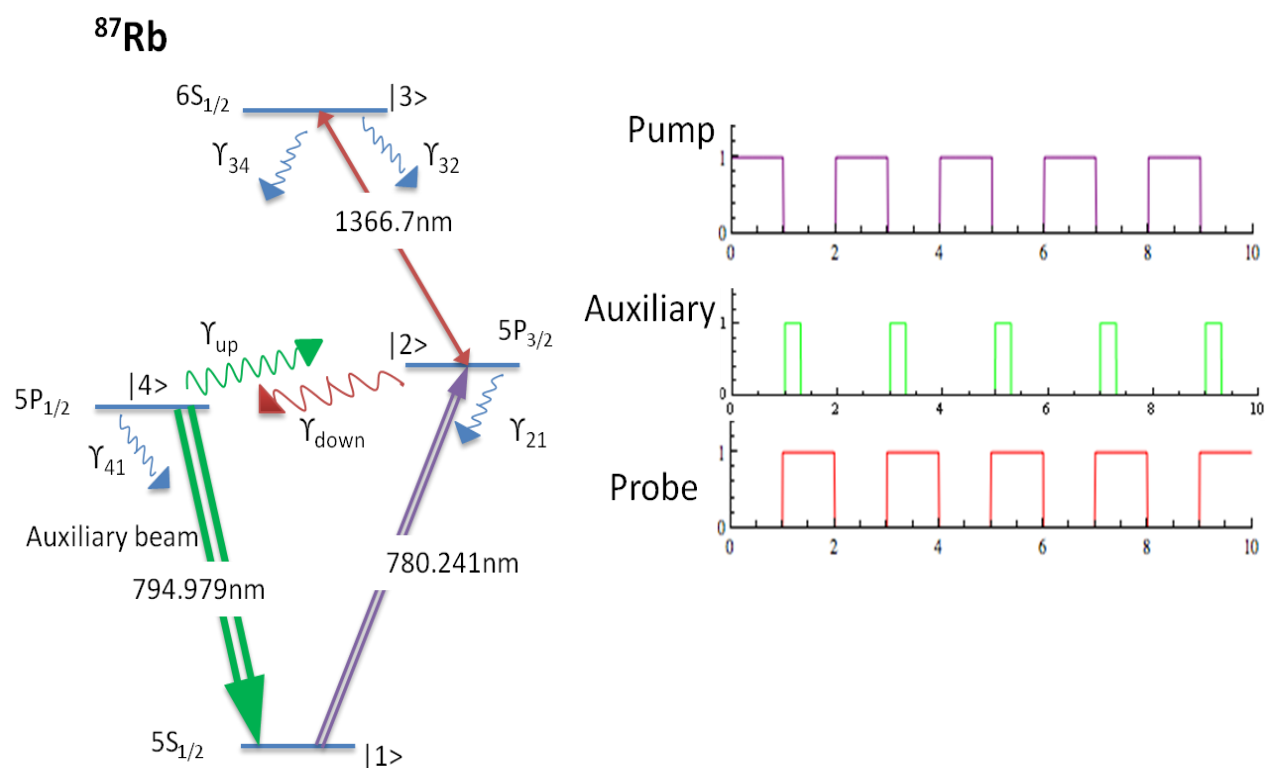


Figure 4.1. Schematic of modulator in the presence of buffer gas and auxiliary beam. The reciprocal relaxation rates (γ_{down} and γ_{up}) for the $5P_{1/2}$ and $5P_{3/2}$ states can be controlled by the pressure of the buffer gas. Typically, $\gamma_{\text{up}} \approx \gamma_{\text{down}} / 4$. For a pressure of about 1 atm, $\gamma_{\text{down}} \approx 10$ GHz. The γ_{mn} (m and n integers) relaxation rates along the optical transitions are due to radiative decays, and are not affected by the buffer gas. Specifically, $\gamma_{34} = \gamma_{32} \approx$

3 MHz and $\gamma_{21} = \gamma_{41} \approx 6$ MHz. A schematic of the timing sequence of the pump and the auxiliary beam and the expected probe absorption are shown on the right.

This process increases the HL for the pump transition significantly. For example, HL (given effectively by γ_{down} , which is much larger than γ_{21}) is about 10 GHz for a buffer gas pressure of 1 atm, and can be as large as 500 GHz for a pressure of 25 atm. However, the rate of decay from the $5P_{1/2}$ state to the ground state is not affected by the presence of the buffer gas, thus preventing rapid repopulation of the ground state. This effect would normally limit the maximum modulation speed achievable. But, this constraint can be circumvented via the addition of an auxiliary beam (which we henceforth call the deshelving beam) that would be turned on at the same time as the pump is turned off, and turned off before turning on the pump again, as illustrated in Fig. 4.1. For best performance, (in terms of contrast obtained during modulation) the pulse width of the de-shelving beam applied should be much smaller than the time scale of the dominant relaxation rate (namely $1/\gamma_{\text{up}}$) from the $5P_{1/2}$ state. However, even for longer pulse widths (up to $100/\gamma_{\text{up}}$), the system produces very good contrast. Furthermore, this beam should be as close as possible to an ideal π -pulse in a 2-level system. The deshelving beam causes rapid repopulation of the ground state, thereby ensuring atoms can be cycled back to the $5P_{3/2}$ state when the pump is turned on again. The speed would be limited by the dominant relaxation rate (γ_{down}) of the $5P_{3/2}$ state, which is in turn controlled by the buffer gas pressure. It is to be noted that while we have chosen to use $6S_{1/2}$ as the highest level to illustrate this scheme, there are many other states (e.g., $7S_{1/2}$, $4D_{3/2}$, $4D_{5/2}$, $5D_{3/2}$, $5D_{5/2}$ and so on) that would work just as well. However, for optimal

operation, the intermediate state must be $5P_{3/2}$, since the quenching rate is higher from $5P_{3/2}$ to $5P_{1/2}$ than that in the reverse direction.

b. Simulation Results

Preliminary results obtained from the simulation of the system shown in Fig. 4.1 are presented in Fig. 4.2. The values of the decay rates used were $\gamma_{\text{down}} \sim 10$ GHz, $\gamma_{\text{up}} \sim 2.5$ GHz, $\gamma_{34} = \gamma_{32} \sim 3$ MHz and $\gamma_{21} = \gamma_{41} \sim 6$ MHz. The simulations are carried out using the Case II configuration, with the negative probe detuning matched to half the Rabi frequency. Thus, the probe is resonant with the $|+\rangle$ to $|3\rangle$ transition. The residual oscillations seen in the probe absorption occur at the pump Rabi frequency.

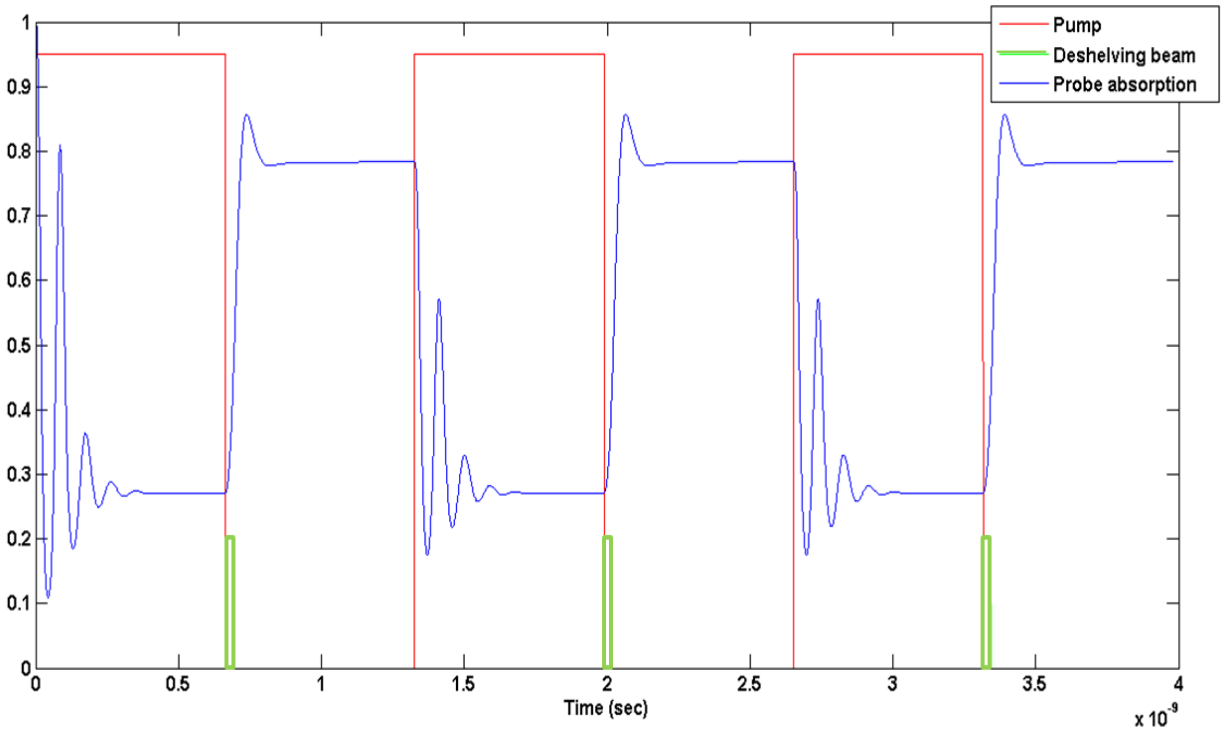


Figure 4.2 High speed modulation in the presence of buffer gas, and using an auxiliary (deshelving) beam. The power levels of the pump and the deshelving beam have been re-scaled. The deshelving beam is applied immediately after turning off the pump and for a very short duration. The modulation speed is about 1 GHz. The temporal width of the deshelving π -pulse used for the simulation is $2/\gamma_{\text{down}}$.

These oscillations can be understood clearly by considering the limiting case where state $|2\rangle$ is completely undamped ($\gamma_{\text{down}}=0$, $\gamma_{21}=0$), state $|3\rangle$ decays to state $|2\rangle$ only, and the deshelving beam is turned off, so that state $|4\rangle$ is completely decoupled from the system. In this case, the population of level $|2\rangle$ oscillates between 0 and 1 (in the limit of a vanishingly weak probe beam) at the rate of the pump Rabi frequency. Thus, if the configuration of Case I is employed, the probe absorption would obviously oscillate (between the maximum value and zero) at the same frequency. Oscillation of the probe

absorption between the maximum value and zero also occurs if Case II is employed.

The later may appear to be somewhat surprising, since the population of the $|+\rangle$ level (as well as that of the $|-\rangle$ level) remains constant at a value of $1/2$, and the probe is resonant with $|+\rangle$ to $|3\rangle$ transition. On the other hand, it is sensible if one considers the fact that at some point in time there are no atoms in state $|2\rangle$. These two observations can be reconciled by noting that even though the probe is resonant with the $|+\rangle$ to $|3\rangle$ transition, there is also the off-resonant transition between the $|-\rangle$ state and state $|3\rangle$. For the very short time scale of the Rabi oscillation, the $|+\rangle$ and $|-\rangle$ state are effectively broadened by the Rabi frequency (akin to transit time broadening), in a manner so that during one point in the Rabi oscillation cycle, the imaginary part of ρ_{32} , which determines the probe absorption (ρ being the density matrix) vanishes due to equal and opposite contributions from the $|+\rangle$ and $|-\rangle$ states. We have verified this explicitly, using numerical simulations under this condition.

In the presence of the strong damping of level $|2\rangle$, as employed in the simulation for Fig. 4.2, these oscillations get damped, producing a steady-state absorption of the probe, on a time scale given by the damping rate of level $|2\rangle$. Thus, if we used the same technique, but without the buffer gas, the probe absorption would remain oscillatory through the whole time during which the pump is on, since the timescale for reaching steady state would be given by the inverse of the radiative decay rate (γ_{21}) of level 2 only, corresponding to more than 30 nanosecond, which is much longer than the modulation

rate shown in Fig. 4.2. Thus, employing Case II by itself is not enough to achieve high speed modulation; the rapid decay rate of level $|2\rangle$ is essential.

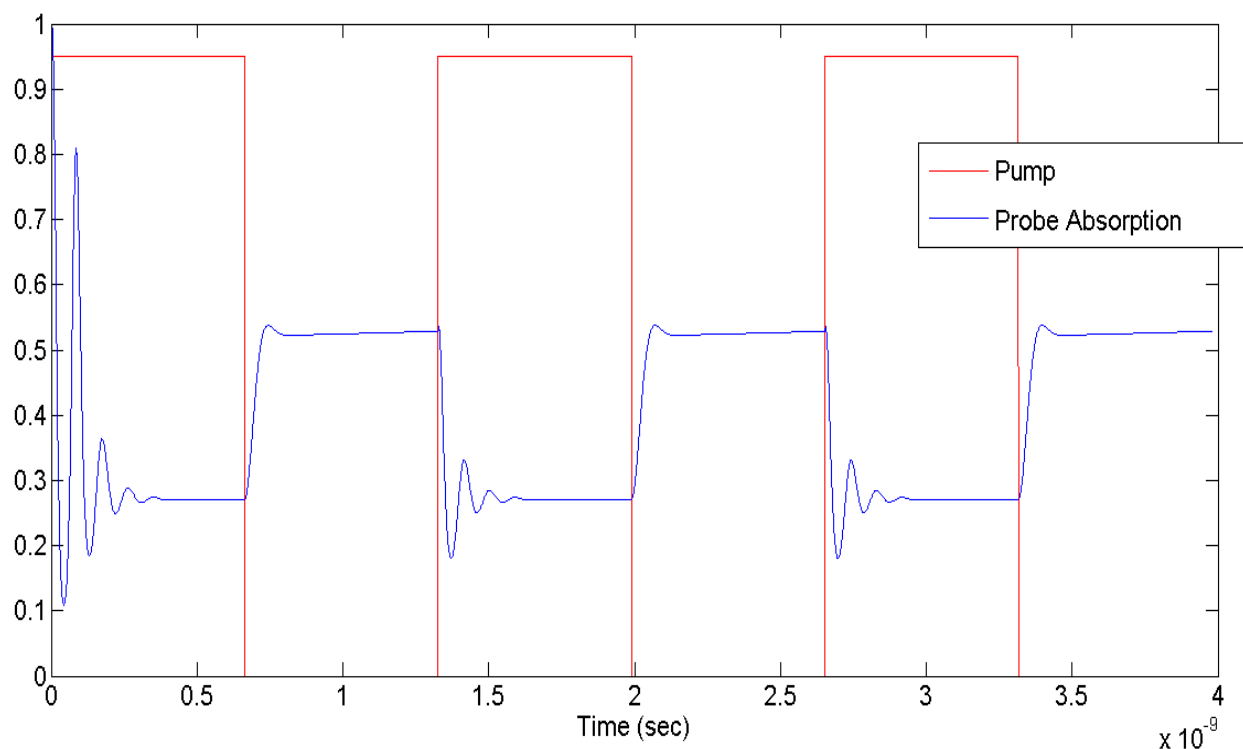


Figure 4.3 High speed modulation using buffer gas but without any deshelving beam. The power level of the pump has been re-scaled. The switching speed is about 1 GHz.

In Fig. 4.3, we show results obtained for the same set of parameters as used in Fig. 4.2, except that the deshelving beam is not used. As can be seen, a modulation with a significant contrast is still achievable. Thus, the presence of the deshelving beam is not essential for obtaining high speed modulation. To see why this is the case, we recall from Fig. 4.1 that there is also a relaxation (γ_{up}) of atoms from the $5P_{1/2}$ state to the $5P_{3/2}$ state in the presence of buffer gas, at a rate which is about 4 times smaller than the decay rate

(γ_{down}) in the opposite direction. Consequently, the atoms never leave the $5P_{3/2}$ state completely during the time when the pump is turned off. Half of these atoms get tuned back to resonance (between the $|+\rangle$ and $|3\rangle$ states) when the pump is turned back on, producing strong absorption. The reduced contrast in the absence of the deshelving beam is due to the fact that fewer number of atoms in state $|2\rangle$ decay to state $|4\rangle$ because there is no mechanism for atoms in state $|4\rangle$ to be transferred to state $|1\rangle$. In the presence of the deshelving beam, the number of atoms remaining in state $|2\rangle$ after the deshelving π -pulse is significantly smaller, thus producing higher transparency for the probe, and consequently higher modulation contrast.

For both cases (deshelving beam on or off), the modulation depth remains virtually uniform for increasing modulation speeds, but the rapid oscillations do not die off at higher speeds. In order to estimate the bandwidth of the modulator, we used the criterion that both the on and off states of the probe must reach a steady state value before the corresponding states of the pump. This gives a bandwidth of about 1.5 GHz for $\gamma_{\text{down}}=10\text{GHz}$. The bandwidth can be increased further by increasing the value of γ_{down} (as well as $\gamma_{\text{up}}=\gamma_{\text{down}}/4$) and scaling the pump power by the same factor. Indeed, preliminary simulation results have shown that the bandwidth roughly scales with γ_{down} . More details about the impact of various parameters, such as pump and auxiliary beam powers, pulse-width of the de-shelving beam, and the decay rates, on the modulator performance in terms of modulation depth and bandwidth will be presented in a separate paper. Efforts

are also underway in our laboratory to investigate the feasibility of realizing a buffer-gas augmented modulator of this type.

It should be possible to realize this scheme in a tapered nano fiber (TNF) set-up, yielding an efficient modulator at the telecom wavelength at very low control powers ($\sim 40\text{nW}$). The TNF will be designed to operate as a single mode fiber for all three wavelengths: 780 nm, 795 nm and 1323 nm. We have carried out designs of such a TNF, and have shown that there is a range of taper diameters for which it is possible to have a significant overlap between the evanescent modes at these three wavelengths. The TNF would be embedded in a Rb vapor cell, and pressurized with a ^4He buffer gas. The pump and the auxiliary beams will be orthogonally polarized, and combined with a polarizing beam splitter. The probe will be combined with these beams using a dichroic mirror. The combined beams will be launched into the TNF. Similar techniques will be used to separate the probe from the other beams at the output. Of course, the intensity needed to saturate a 500 GHz broadening would be too hard to realize in a TNF. However, based on a typical DPAL laser employing Rb, which requires a threshold pump intensity of about $15\ \mu\text{W}/\mu\text{m}^2$, a pump power of about $3\ \mu\text{W}$ should be enough to achieve a few GHz modulation bandwidth in the TNF, which has a mode area of only $0.2\ \mu\text{m}^2$.

Experimental results to be added

CHAPTER 5 - OPTICALLY CONTROLLED POLARIZER

Quantum Zeno effect (QZE)

The quantum Zeno effect (QZE)^{20,21,22} is the suppression of the evolution of a quantum state through the quantum measurement process. Figure 5.1(a) shows the energy level diagram of a three level system that illustrates this process. Here, states $|1\rangle$ and $|2\rangle$ are assumed long-lived, while state $|3\rangle$ decays rapidly, at a rate Γ , into state $|1\rangle$ only. The QZE in this configuration can be described as follows. In the absence of any coupling to state $|3\rangle$, state $|1\rangle$ will undergo Rabi oscillation, thus getting excited to state $|2\rangle$ at a rate determined by the $1 \rightarrow 2$ coupling strength. When coupled to state $|3\rangle$, the spontaneous emission emulates a measurement process, which resets the quantum state of the system to state $|1\rangle$. As such, evolution of state $|1\rangle$ into state $|2\rangle$ is inhibited.

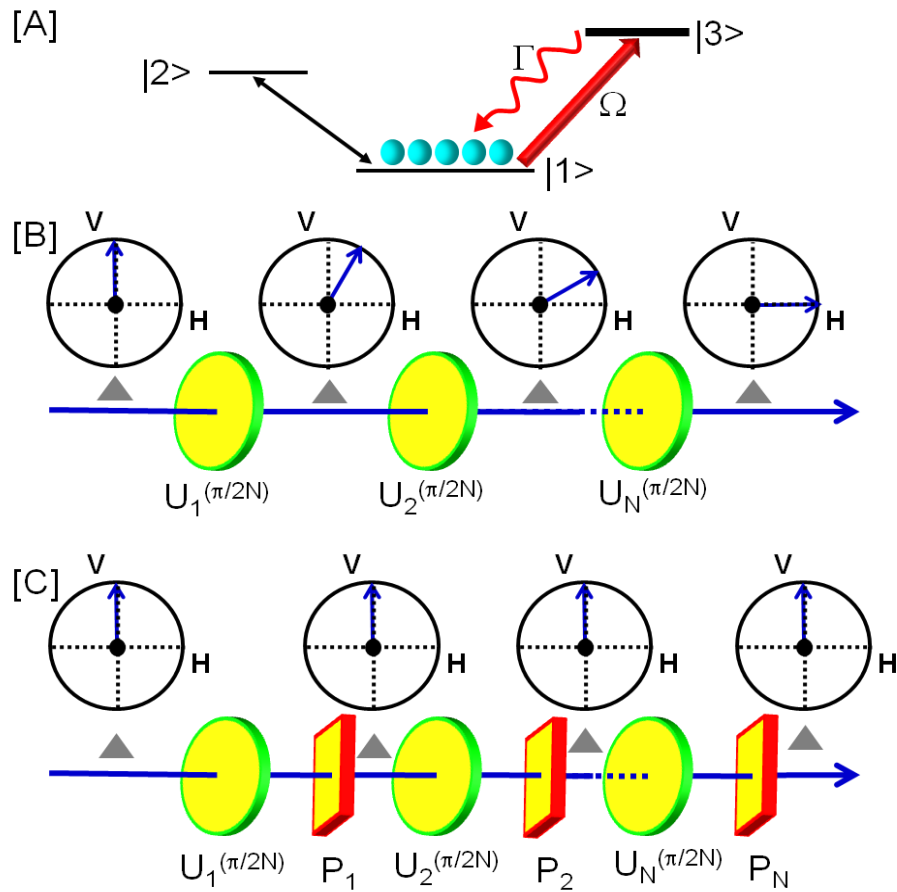


Figure 5.1 [A] Quantum Zeno Effect in an atomic V-system. [B] Evolution of the quantum state of a photon via passage through a series of waveplates. [C] In the presence of interleaved polarizers acting as measurement devices, the evolution to the horizontally polarized state is inhibited.

The phenomenon described above, although initially investigated in the context of atomic transitions, is in fact a general quantum mechanical effect occurring in any system where periodic quantum measurement and quantum state evolution occur. In particular, it is instructive to analyze a bulk-optic model for this effect, as illustrated in Fig. 5.1(b). Here, we consider the evolution of the polarization state of a photon. The polarization degree of freedom for the photon spans two orthogonal states: $|V\rangle$ and $|H\rangle$ representing vertical and horizontal polarizations, respectively. The general quantum state can thus be

written as $\alpha|V\rangle + \beta|H\rangle$, with $|\alpha|^2 + |\beta|^2 = 1$. Consider now a specific situation where input quantum state is $|V\rangle$. When it passes through a wave plate with its fast/slow axis at an angle of 45° with respect to the vertical axis, the polarization state of the photon can be expressed as (ignoring an overall phase factor) $|\psi\rangle = \cos(\Delta n \omega t / 2)|V\rangle + i \sin(\Delta n \omega t / 2)|H\rangle$, where Δn is the difference in refractive index between the fast and slow axis of the waveplate, t is the time of propagation and ω is the optical frequency. We can describe this process by an unitary evolution operator U_ϕ such that $U_\phi|V\rangle = \cos\phi|V\rangle + \sin\phi|H\rangle$, where $\phi = \Delta n \omega t / 2$. When N such plates are placed in series, each causing a unitary evolution U_ϕ with $\phi = \pi/2N$, the polarization state of the photon at the output become $|H\rangle$, aside from an overall but inconsequential phase factor. Consider next a situation where these waveplates are interleaved with polarizers oriented along the vertical axis, as shown in Fig. 5.1(c). The polarizers act as a measurement device, collapsing the state to be $|V\rangle$ with probability $\cos^2 \phi$. In the limit $N \rightarrow \infty$, corresponding to continuous measurement, the final state will be the same as the initial state.

It is also instructive to analyze this process without invoking a quantum description of light. Specifically, we consider a classical light beam polarized in the \hat{x} (vertical) direction at the input. After passing through a waveplate, the polarization state can be expressed as $\alpha\hat{x} + \beta\hat{y}$, with $|\alpha|^2 + |\beta|^2 = 1$, and $\alpha = \cos(\pi/2N)$. It is now easy to see that after a series of N waveplates and polarizers, the output intensity can be expressed as $I_{\text{out}} = I_0 [\cos^2(\pi/2N)]^N$ and in the limit $N \rightarrow \infty$, it can be verified that $I_{\text{out}} \rightarrow I_0$, where I_0 is the initial intensity. This result seems to imply that there is a so-called “classical Zeno effect”. This

is erroneous, since the concept of a measurement induced reduction of a state is absent in the classical World. Instead, the process can be understood via the Quantum Zeno effect by considering a quantum model of a classical laser field (by which we mean a field with intensity much stronger than that of a single photon). Any such field (including, but not limited to the coherent state) can be expressed as a superposition of the Fock states: $|V\rangle = \sum_n \alpha |n\rangle$. Now, the analysis we presented above for a single photon can be applied to each Fock state. Thus, after passing through the series of N polarizers and waveplates, the polarization state remains the same. Therefore, QZE applies even if one does not explicitly consider the optical field quantum mechanically.

b. Optically controlled polarizer

It is well known that the polarization state of an optical field gets modified after propagating through an optically dense vapor medium, a manifestation of optical activity. In an atomic system involving ladder type transitions, the presence of two different frequencies open up the possibility of controlling the behavior of the probe (upper leg) polarization by careful design of the pump parameters (lower leg). In particular, it is possible to make the vapor cell act as a polarizer, oriented either vertically or horizontally depending on the polarization of the pump.

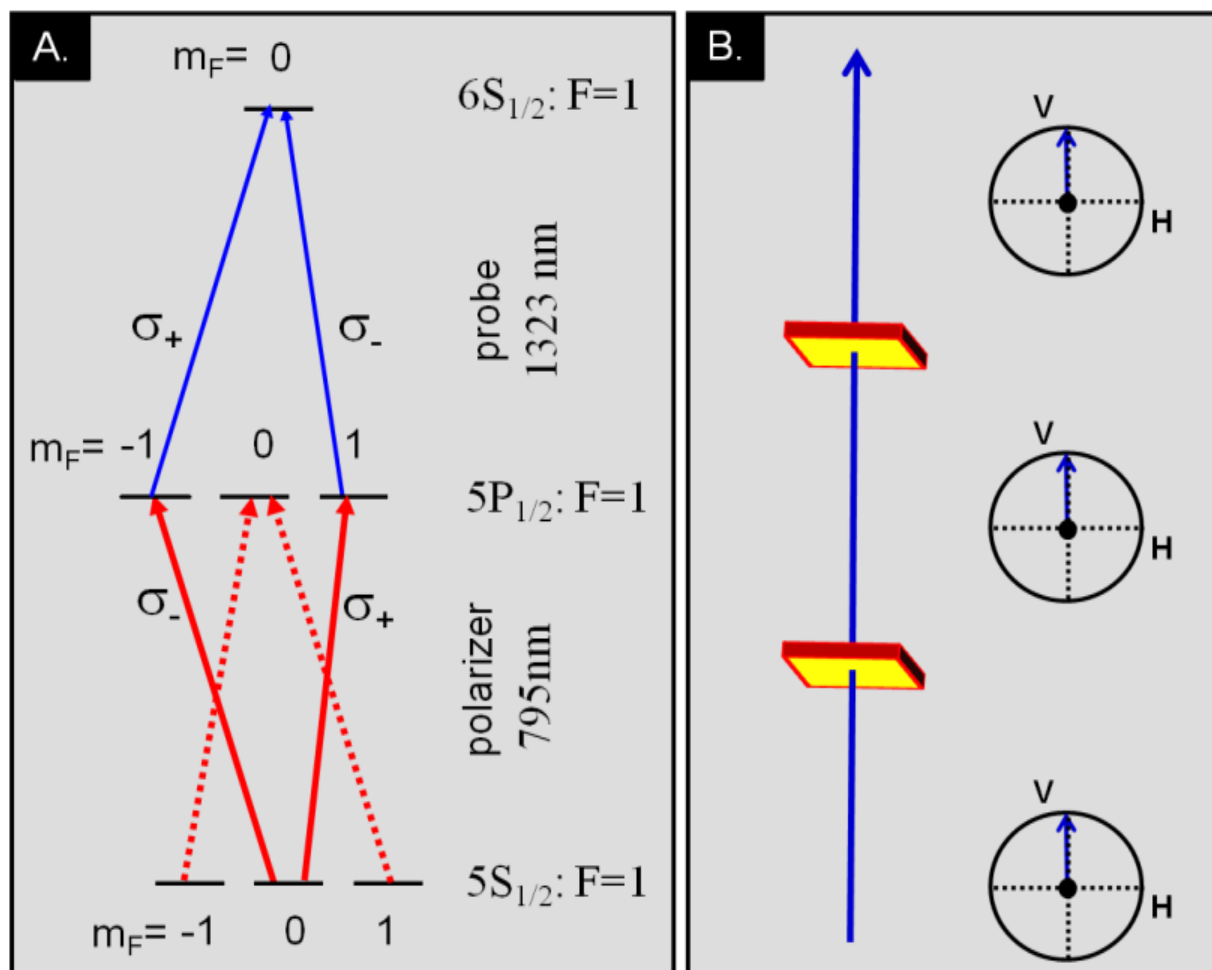


Figure 5.2 Schematic illustration of an optically controlled polarizer using a ladder transition in 87Rb atoms.

In Fig. 5.2(a), we illustrate the basic mechanism for realizing such a polarizer, using a simplified set of transitions. We assume here that the atomic population is optically pumped into $5S_{1/2}, F = 1, m_F = 0$ Zeeman sublevel. Here, the control beam at 795 nm is resonant, and linearly polarized, in the horizontal direction, for example. This means that the two circular components of the control beam, σ_+ and σ_- , are out of phase with each other. As such, these components will produce an out-of-phase superposition of the $m_F = 0$ and $m_F = 1$ Zeeman sublevels. Such a superposition would act as a non-absorbing

(dark) state for the 1323 nm probe that is vertically polarized, since it has two circular polarization components (σ_+ and σ_-) that are in phase with each other. By the same token, this superposition will act as a strong absorber for a 1323 nm probe that is horizontally polarized. Thus, the presence of this control beam would make the system an ideal polarizer. Of course, experimental conditions result in non-ideal behavior and these are discussed in later sections.

c. QZE based all-optical logic gate

A QZE based optical logic gate can be realized if the polarizing effect generator is augmented by a wave-plate effect generator, as shown in Fig. 5.3. Before we understand the working of the logic gate, it is instructive to understand how the waveplate effect is generated. Consider first the case where the lower leg is excited by the field which is detuned from resonance, and the fields on resonance arrows are turned off. The control field is now a right-circularly polarized (σ_+) beam at around 795 nm, tuned a few GHz below the $5S_{1/2}, F = 1 \rightarrow 5P_{1/2}, F = 1$ transition. We assume here that the atomic population is optically pumped into the $5S_{1/2}, F = 1, m_F = 0$ Zeeman sublevel. The control beam, therefore, produces an off-resonant excitations to only the $5P_{1/2}, F = 1, m_F = 1$ Zeeman sublevel in the intermediate state. The probe, at around 1323 nm, is chosen to be linearly polarized; therefore, it has two components: σ_+ and σ_- . As shown in the diagram, the σ_- component sees the effect of the atoms (because of the detuning, it sees only a real susceptibility, with virtually no absorption), while the σ_+ component does not. The parameters of the control beam can be tuned to achieve the condition for a π phase-shift

for the σ -component only, so that the polarization of the signal beam is rotated by 90 degrees. Theoretical and experimental investigations of controlled polarization rotation of a probe field using another optical field (pump) and employing ladder transitions in Rb have been carried out previously^{23,24}. However, both of these employ the EIT effect where the upper leg is excited by a strong control field while the lower leg is probed by a weak optical field, and thus has fundamentally different characteristics than the system we have considered.

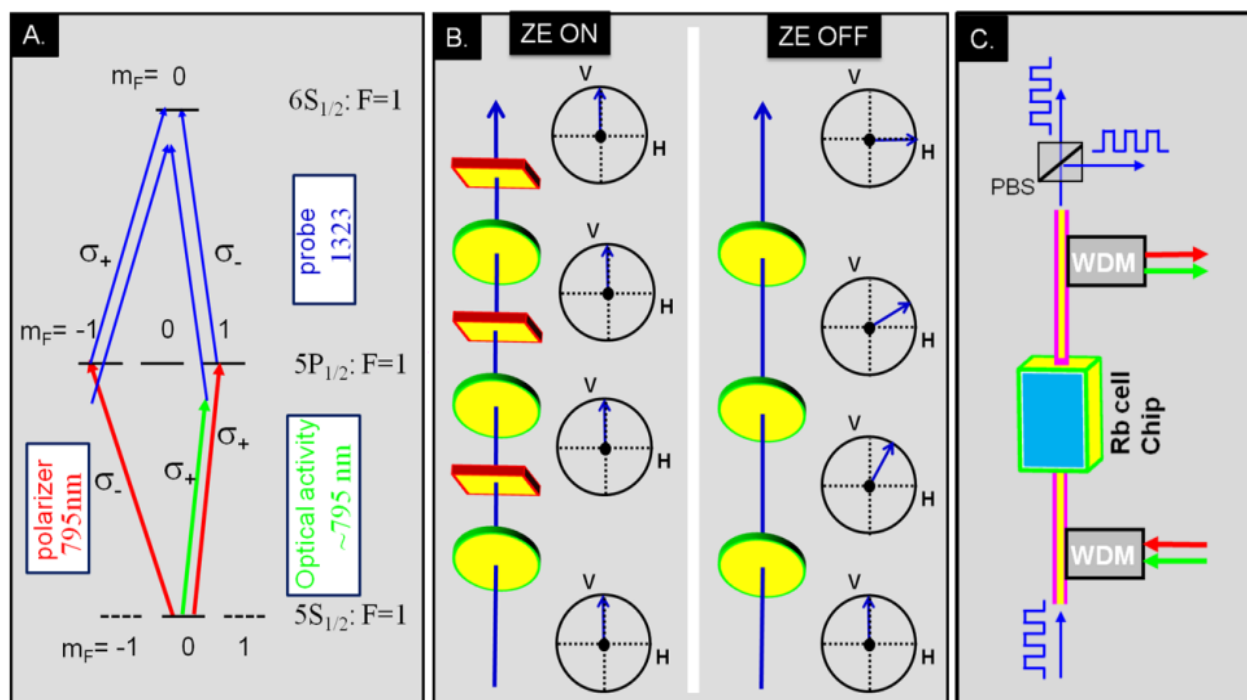


Figure 5.3 Schematic illustration of an optical logic gate using a ladder-transition based polarizer and optical activity in Rb atoms.

The red beams on the lower leg represent the control signal for the polarizer. The presence of this control beam results in selective transmission of one particular polarization of the signal beam (blue) and complete suppression of the orthogonal

polarization, as explained previously. In order to understand the effect of applying both the green and red control beams simultaneously, one should recall the model presented in Fig. 5.1 for the QZE and the discussion that followed, where we considered N pairs of polarizers and polarization rotators, and showed that the polarization does not change as $N \rightarrow \infty$. The physical implementation described here operates in this limit. Even though both processes are occurring simultaneously, the net result is equivalent to infinitesimal evolutions where the processes alternate after each time step.

When the polarizing effect generator is turned off, the polarization of the probe beam rotates by 90 degrees; when it is left on, the Zeno effect induced by the measurement due to the polarizer prevents the polarization of the probe beam from rotating, without any attenuation. This is illustrated in Fig. 5.3(b). On the other hand, when the waveplate effect generator is turned off, the polarization state does not change at all. In Fig. 5.3(c), we show how this process can be used as an optical logic gate for a probe data stream. Briefly, using WDM couplers, all the control beams and the probe at 1323 nm are made to propagate through a Rb vapor cell. Another WDM coupler is used to filter out the beams at 795 nm before the final polarizing beam splitter (PBS) placed at the output. The two ports of the PBS serve as the two output channels of the gate. If the control beams represent a data stream with their presence and absence denoting the ‘1’ and ‘0’ state respectively, then it is easy to construct a truth table for the outputs at port 1 and 2 respectively as shown in Table 1.

Table 1. Truth table for QZE based logic gate

Polarizer	Waveplate	O/P at Port 1	O/P at Port
0	0	1	0
0	1	0	1
1	0	1	0
1	1	1	0
X	Y	$X + Y'$	$X'Y$

Thus, if the sense of the '1' and '0' states of the waveplate effect generator beam are reversed, output at port 1 simply implements an OR operation on the 2 inputs while if the same is done for the polarizer effect generator, output at port 2 implements an AND gate. Of course, the output at ports 1 and 2 are complementary, as expected for a PBS. Full implementation of such a logic gate requires the realization of both the polarizer effect and the waveplate effect in the same medium. However, given the complexity offered by an actual atomic system, we decided to investigate and optimize these two effects separately.

e. Experimental set-up

The experimental configuration we used to realize an optically controlled polarizer is shown schematically in Fig. 5. 4. We used a conventional vapor cell, containing a natural mixture of both the isotopes of Rb. However, we used only ^{87}Rb for our experiment. Here, the control beam and signal beam are co-propagating. A similar set-up was used when the control beam and the signal beam were counter-propagating.

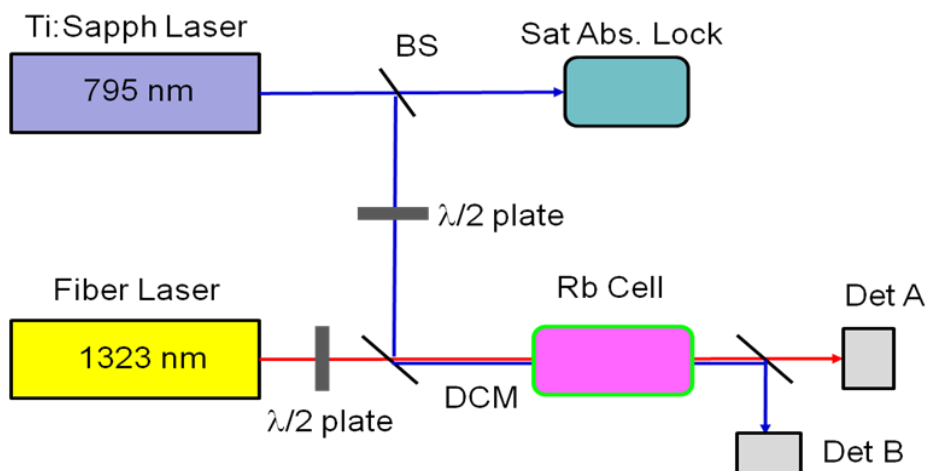


Figure 5.4 Experimental setup used to realize the ladder-system polarizer.

Briefly, beams from two tunable lasers (one at 795 nm, and the other at 1323 nm) were combined with a dichroic mirror (DCM). A part of the 795 nm light was sent to a reference vapor cell for saturated absorption spectroscopy and locking. The combined beams were sent through a vapor cell, shielded from magnetic fields with μ -metal. The cell was heated using bifilarly wound wires that do not add any magnetic fields. After passing through the cell, another DCM was used to split the light into two parts, and each frequency was detected with a separate detector. The polarization of each input beam was controlled separately with two half waveplates. The control laser was locked to one of the lines on the $5S_{1/2}$, $5P_{1/2}$ manifold, while the signal laser at 1323 was scanned over the $5P_{1/2}$ – $6S_{1/2}$ manifold. For the remainder of the paper, the hyperfine levels in the ground state are indicated by unprimed alphabets (F), those in the $5P_{1/2}$ level are primed (F') and those in the $6S_{1/2}$ level are double-primed (F'').

In section 3, we showed a simplified set of energy levels in order to explain the basic process behind an optically controlled polarizer. In practice, however, it is extremely

difficult to realize such an ideal system. For example, it is generally necessary to take into account both the hyperfine levels ($F' = 1$ and $F' = 2$) in the $5P_{1/2}$ manifold to account for Doppler broadening and power broadening. Furthermore, it is virtually impossible to eliminate all the atoms from the $m_F = \pm 1$, $F = 1$ Zeeman sublevels via optical pumping. Hence, all the Zeeman sub-levels at the $5P_{1/2}$ manifold also get coupled with the optical fields. The full set of relevant energy levels that need to be considered are shown in Fig. 5.5. In our model, we considered all the Zeeman sub-levels which explicitly interact with an optical field (all sub-levels of the $F=1$, $F'=1,2$ and $F''=1,2$ hyperfine levels), while the $F = 2$ hyperfine level and the $5P_{3/2}$ level were only considered as population transfer levels and hence all their sub-levels were lumped together as a single level. The transition strengths²⁵ indicated are expressed as multiples of the weakest transition, which in our case is the transition from the $F = 1$, $m_F = 1$ sub-level to the $F' = 1$, $m_F = 0$ sub-level. In order to avoid unnecessary clutter, the matrix elements for the $F' = 1$ to $F'' = 1, 2$ transitions and for the $F' = 2$ to $F'' = 1$ transition are not shown. More details regarding the model are presented in the section 8. Initially, we carried out our experiments without employing optical pumping. Later in the paper, we will discuss in detail how to implement optical pumping properly in order to optimize the performance of the polarizer.

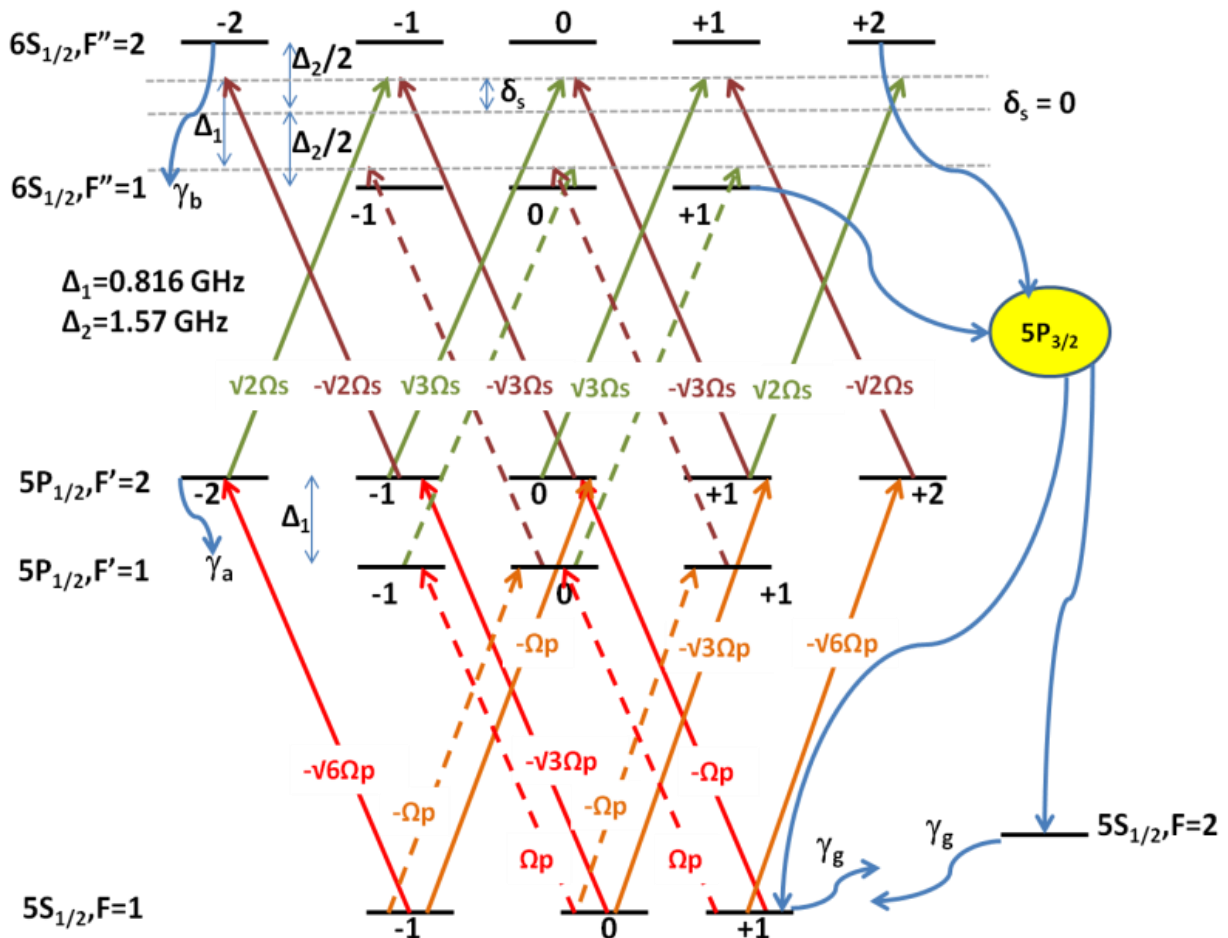


Figure 5.5 Model used for numerical computation. See text for more details.

f. Results

Figure 5. 6(a) shows evidence of the polarizing property of the control beam as the signal beam was scanned across the $5P_{1/2} \square 6S_{1/2}$ manifold. The control beam was vertically polarized, co-propagating with the signal beam, had a power of $\sim 5 \text{ mW}$ and was locked to the $F = 1 \square F' = 2$ line. The temperature of the cell was about $\sim 200 \text{ Celsius}$. The blue (red) trace is the signal transmission when the signal beam is vertically (horizontally) polarized. The $F'' = 1$ and $F'' = 2$ labels indicate the transitions from the $F' = 2$ level, as

the power of the control beam was not strong enough to produce excitations to the far detuned $F' = 1$ level. As is evident from Fig. 5.6(a), signal transmission for the $F' = 1 \rightarrow F'' = 1$ increased significantly when the control beam and the signal beam are cross-polarized. The $F' = 1 \rightarrow F'' = 2$ transition showed opposite behavior to the $F' = 1 \rightarrow F'' = 1$ line in terms of the percentage of absorption. This is due to the fact that the matrix elements for the σ -transitions of the $F' = 2 \rightarrow F'' = 2$ line are of opposite sign as compared to the $F' = 2 \rightarrow F'' = 1$ line 25, and hence the σ -coherences pick up an additional phase difference of π , thus changing the sense of polarization from horizontal to vertical and vice-versa. The assumption in the preceding argument is that the significant contribution to the absorption of the signal beam is from the $F' = 2$ level, since the $F' = 1$ is highly detuned.

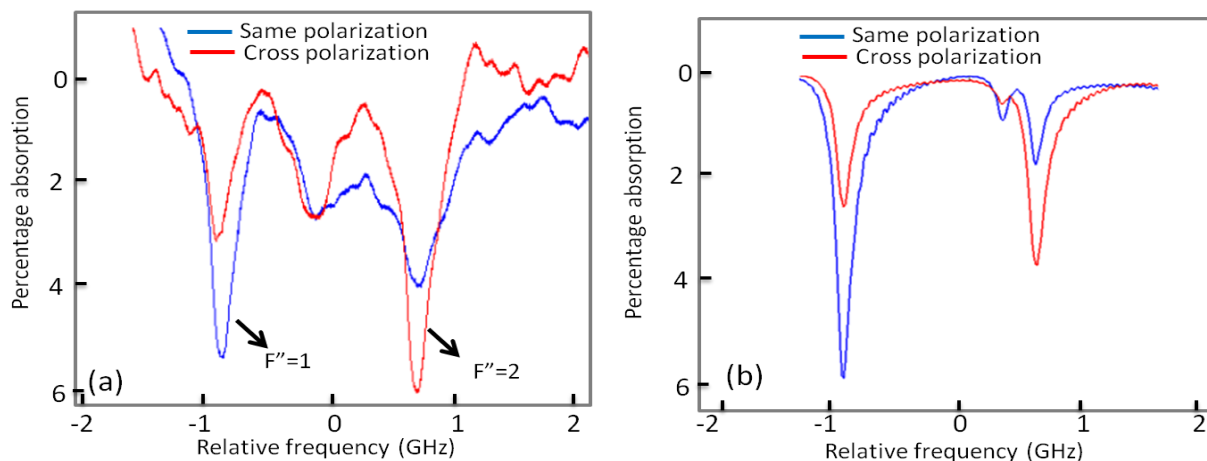


Figure 5.6 Polarizer effect for co-propagating geometry for pump power $\sim 5\text{mW}$ a) Experiment b) Theory.

We obtain $\sim 50\%$ reduction in absorption for the $F' = 2 \rightarrow F'' = 1$ line and about $\sim 70\%$ reduction for the $F'' = 2$ line. The background modulation is due to an etalon effect

caused by the two windows of the cell, which were anti-reflection (AR) coated for 795 nm, but not for 1323 nm. In the future, the etalon effect could be eliminated by using a cell where the windows are not parallel to each other, along with AR-coating at 1323 nm. **Figure 5. 6(b)** shows the corresponding numerical simulation and it is fairly consistent with our experimental result. For this particular simulation, the pump was slightly detuned below the $F = 1 \square F' = 2$ line and this results in the appearance of an additional dip near the $F'' = 2$ line, which is due to the $F' = 1 \square F'' = 2$ line. Indeed, this feature does not appear if the pump laser is resonant with the $F = 1 \square F' = 2$ line or if the pump power is not sufficient to excite the atoms to the $F' = 1$ level. In the experimental data too there seems to be an additional dip in-between the two lines, which we believe may not be caused due to the etalon effect alone. As our simulations indicate, this additional feature might be due to a shift in the pump laser frequency resulting in excitations from the $F' = 1$ level, but a more thorough investigation is needed to resolve this apparent discrepancy. However, it should be noted that the device we propose would operate at one of the main absorption dips, rendering the central dip largely irrelevant.

We also investigated the performance of the polarizer under a counter-propagating geometry. **Figure 5.7** shows data for the $F'' = 1$ transition obtained for two different power levels ($\sim 2\text{mW}$ and $\sim 200\text{mW}$) of the control beam and the corresponding numerical simulation. The $F'' = 2$ transition also showed similar behavior and is not shown here for the sake of brevity.

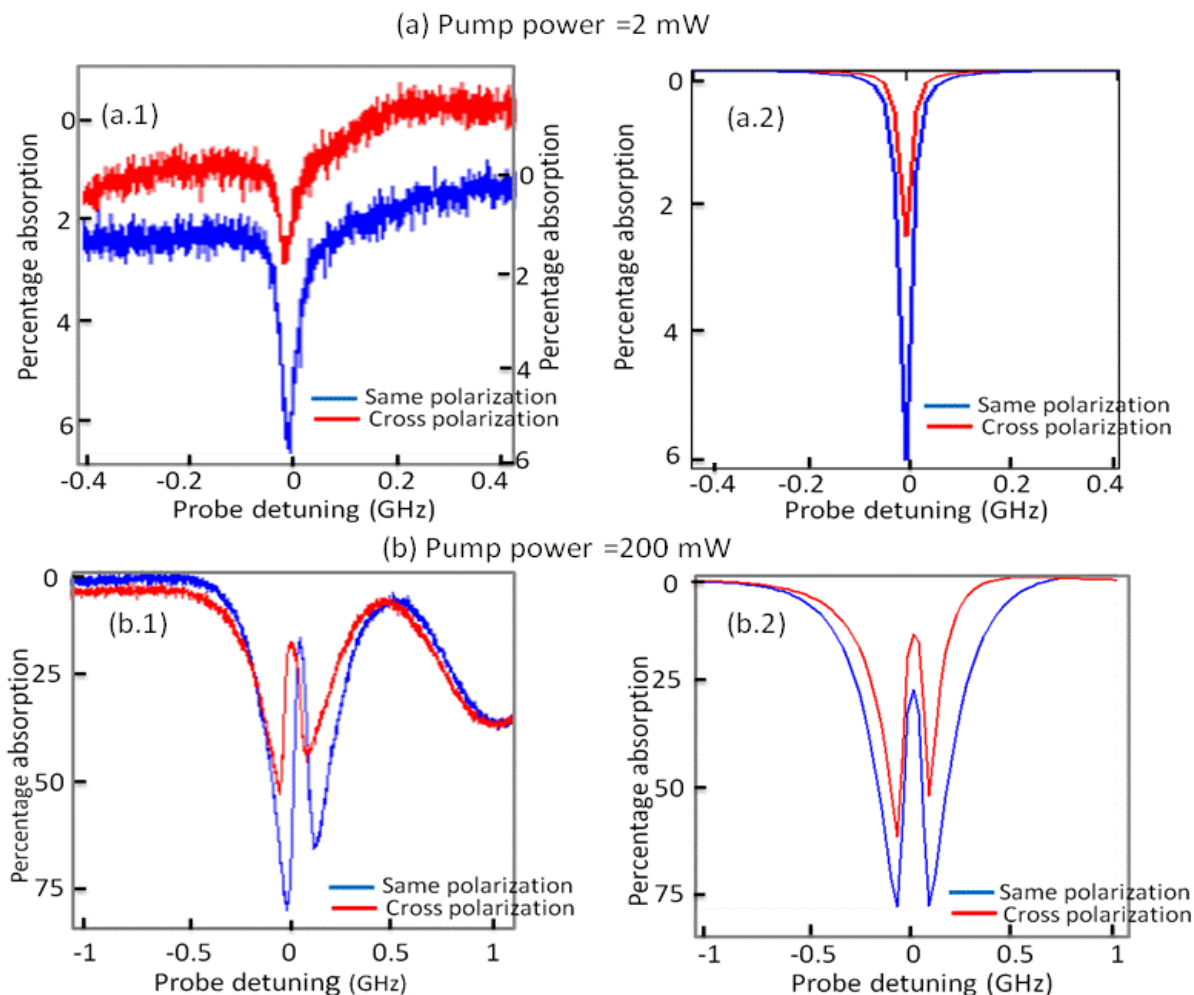


Figure 5.7 Polarizer effect for counter-propagating geometry for 2 different powers of the pump. a.1) Experiment a.2) Theory and b.1) Experiment b.2) Theory.

It is useful to note a couple of differences in the observed signals between the co-propagating and the counter-propagating cases. Since we do not have experimental data under identical conditions (powers of the pump and the probe, temperature etc.) for the two geometries and our theoretical results are fairly consistent with our experimental data, we would present these differences using our simulation results. Figure 5.8 shows the simulation results for both geometries for a pump Rabi frequency of 5 (in units of the

natural linewidth of the 5P manifold ~ 5.7 MHz) when both the control and the signal beams have the same polarization. As seen in Fig. 5.8, the counter propagating geometry produces narrower (and deeper) absorption lines as compared to the co-propagating case. In addition, there is also an apparent splitting in the counter-propagating geometry which is absent in the co-propagating case. These differences based on geometry are due to what we refer to as pump power limited Doppler broadening (PPLDB).

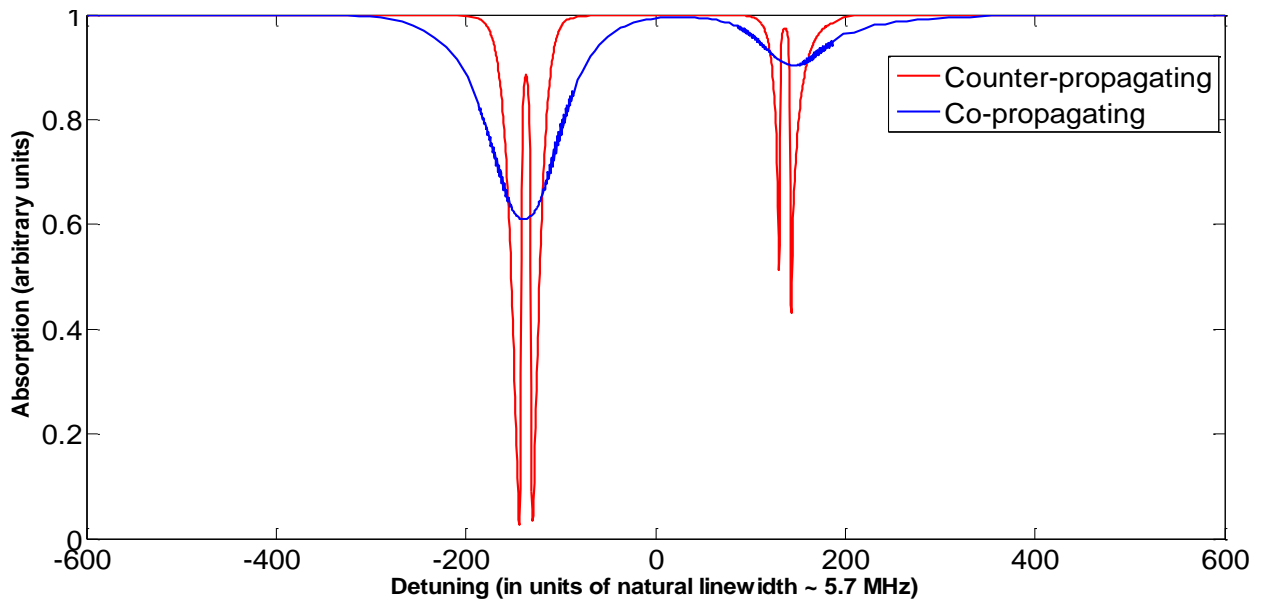


Figure 5.8 Typical absorption profile for co- and counter-propagating geometries. Here, $\Omega_p = 5$.

For the purpose of understanding, it suffices to consider a 3-level cascade system with similar energy difference between the levels as in our original system i.e $k_2 \sim 0.6 k_1$.

Figure 5.9(a) shows such a system where the pump is on resonance with the intermediate level and the probe is scanned across the upper level. Figure 5.9(b) shows the (partial) dressed picture of the interactions for the zero velocity atoms. Here $|1'\rangle$ and $|2'\rangle$ are shown to be degenerate (with $\delta_p=0$), while we show $|3\rangle$ to be higher in energy by an

amount equal to probe field energy (for $\delta_s=0$). This picture is valid for a weak probe and enables us to understand clearly the dynamics of the probe absorption. On the right-side of Fig. 5.9 (b), we show the two split states that result from diagonalization of the interaction between $|1'\rangle$ and $|2'\rangle$. Similar diagrams are shown in Figs. 5.9(c) and 5.9(d) for a positive velocity (same direction of propagation as pump) for the co- and counter-propagating configurations, respectively.

For an arbitrary velocity group v , the energies of the partially diagonalized states can be easily calculated to be $\lambda = (-k_1 v \pm \sqrt{(k_1 v)^2 + \Omega_p^2})/2$, where k_1 is the wavevector of the pump optical field and Ω_p is the pump Rabi frequency. Thus, for the zero-velocity group of atoms, these atomic states would have energies $\pm\Omega_p/2$ and hence would produce absorption at probe detunings of $\mp\Omega_p/2$, as shown in Fig. 5.9(b). This is a manifestation of the well-known Autler Townes splitting (ATS). For any non-zero velocity group, the probe would be further Doppler shifted by $k_2 v$, with the direction of shift depending on whether the probe is co- or counter-propagating, as shown in Figs. 5.9(c) and 5.9(d) respectively. Thus, the resonances would occur at $\left(k_2 + \frac{k_1}{2}\right)v \mp \sqrt{(k_1 v)^2 + \Omega_p^2}/2$ for a co-propagating probe and at $\left(k_2 - \frac{k_1}{2}\right)v \mp \sqrt{(k_1 v)^2 + \Omega_p^2}/2$ for a counter-propagating probe. We also note that the velocity spread of atoms that contribute significantly to the absorption can be estimated to be of the order of $k v_{\text{FWHM}} \sim \sqrt{\Gamma_2^2 + 2\Omega_p^2}$ where Γ_2 is the decay rate of the intermediate level. From these expressions, we can make the following observations:

a) For a vanishingly weak pump, the spread of the velocity groups that contribute significantly to the absorption of the probe is very small ($k v_{FWHM} \sim \Gamma_2$). Thus, both geometries would produce narrow lines (although co-propagating is still slightly broader) with linewidths that are essentially Doppler free and primarily determined by the decay rates of the intermediate and upper level. We can roughly estimate the minimum observable linewidth to be $\sqrt{\Gamma_2^2 + \Gamma_3^2}$, where Γ_3 is the decay rate of the upper level.

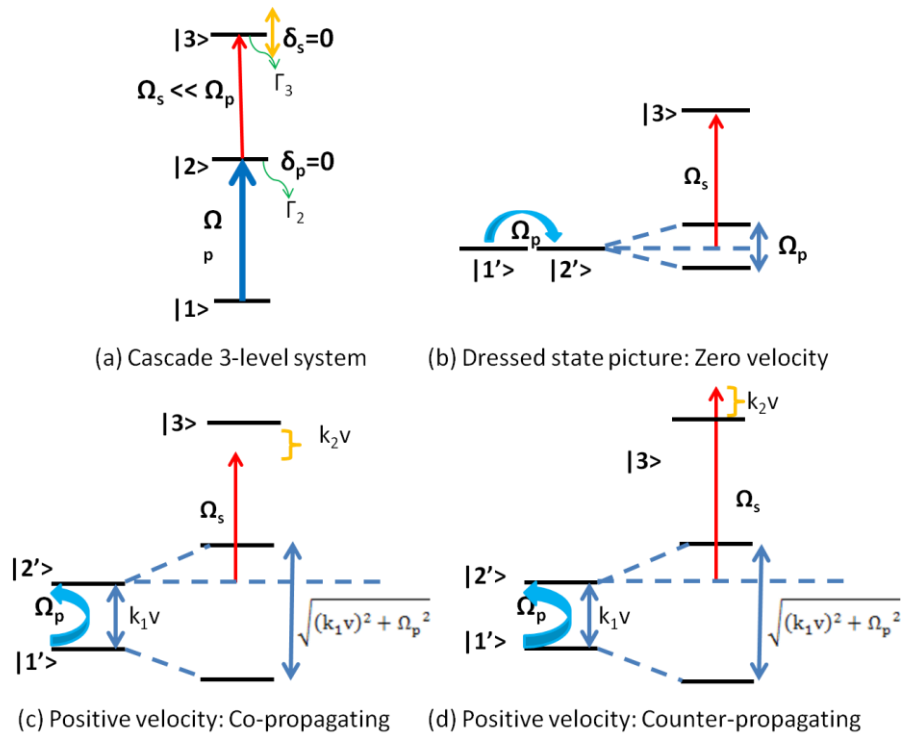


Fig. 5.9. Dressed state picture of 3-level cascade system for different velocity groups

b) There are some differences that arise for a pump Rabi frequency that is much larger than the minimum observable linewidth. We first note that in the co-propagating case, for any given pump Rabi frequency Ω_p we can always find a velocity group, $v_{\text{zero}} = \Omega_p / 2\sqrt{k_2^2 + k_1 k_2}$ that produces resonance at zero probe detuning. If we carry out a similar exercise for the counter-propagating case, we find that the velocity group that produces resonance at zero probe detuning would have $v_{\text{zero}} = \Omega_p / 2\sqrt{k_2^2 - k_1 k_2}$ and this has no valid solution if $k_2 < k_1$, as is the case for our system. As a consequence, in a co-propagating geometry, ATS is generally washed out while it is preserved to some extent in the counter-propagating geometry, the specific details of which depend on the exact value of Ω_p .

c) Finally, we also note that $\left(k_2 + \frac{k_1}{2}\right)v$ is much larger than $\left(k_2 - \frac{k_1}{2}\right)v$. Thus, the resonances for the co-propagating geometry occur at much larger detunings, resulting in broader (and consequently shallower) lines as compared to the counter-propagating geometry.

Similar conclusions can be reached for the negative velocity group of atoms. We refer to this phenomenon of line broadening in a cascade system for a strong pump as Pump power limited Doppler broadening (PPLDB) since the number of velocity groups that contribute significantly to the absorption signal is proportional to the pump power. In Fig. 5.10, the contribution to the absorption (not normalized over the Doppler profile) from three velocity groups $(-V_{\text{zero}}, 0, +V_{\text{zero}})$ are presented for both co-propagating and counter-

propagating geometries for our simplified system. As seen in Fig. 5.10, in the co-propagating case, the non-zero velocity groups contribute significantly to the absorption at zero detuning, while in the counter-propagating case, the contributions from non-zero velocity groups tend to align with the zero-velocity group contribution.

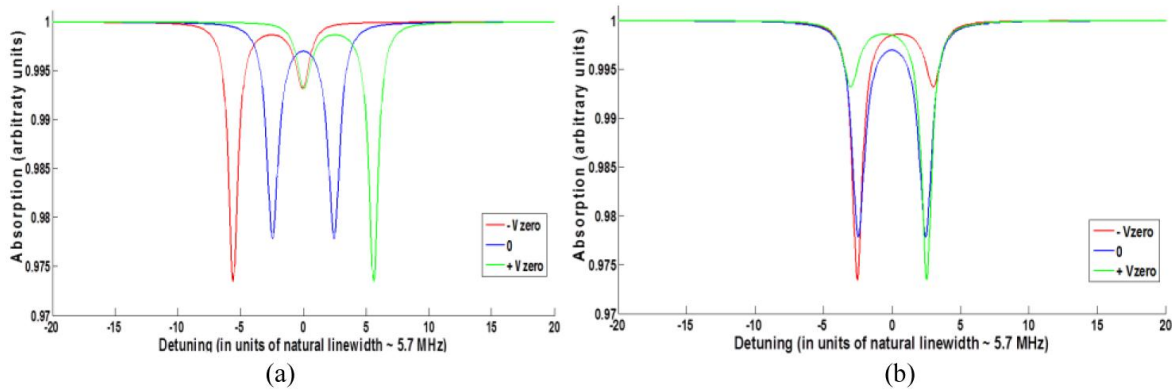


Fig. 5.10. Contribution to absorption from 3 sample velocity groups ($-v_{\text{zero}}, 0, +v_{\text{zero}}$) for a 3-level cascade system when the control beam and signal beam are a) Co-propagating b) Counter-propagating

Of course, our original system involving all the Zeeman sublevels is more complicated due to the presence of additional levels and the fact that Rabi frequencies for the various transitions are not identical, but the intuition developed above using a simplified 3-level cascade system remains valid. In Fig. 5.11, the contribution to the absorption of the $F''=1$ line from 3 velocity groups ($-u/10, 0, +u/10$, where u is mean velocity of atoms) are shown for our original system (see Fig. 5.5) under both geometries.

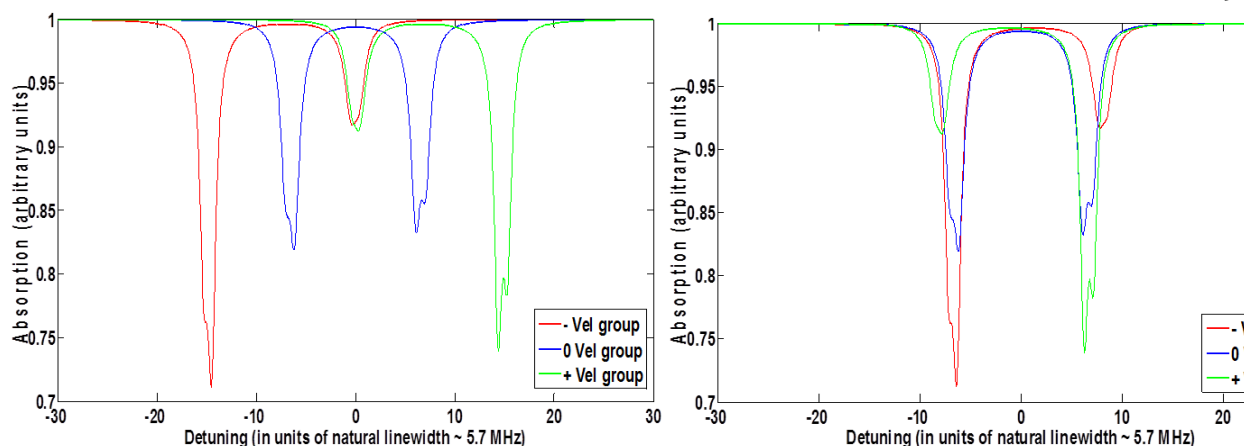


Fig. 5.11. Contribution to absorption of $F'' = 1$ line from 3 sample velocity groups ($-u/10, 0, +u/10$ where u is the mean velocity of Rb atoms) for our original cascade system (see Fig. 5.5) when the control beam and signal beam are a) Co-propagating b) Counter-propagating

But for the slight asymmetry in the line shapes and the appearance of some additional structure in each of the individual lines (due to the presence of multiple levels), the basic features remain identical to that of the simplified 3-level system allowing us derive the same conclusions. Thus, in a co-propagating geometry, the absorption lines are broader, shallower and the ATS is usually washed out while in a counter-propagating geometry the lines are narrower, deeper and ATS is generally preserved in the counter-propagating case, as was seen in Fig. 5.8.

Despite the significant differential absorption at virtually all power levels of the 795nm light, in order for our system to work as an ideal polarizer, we need nearly 100% suppression of one polarization versus nearly 100% transmission for the orthogonal

polarization. Towards this end, we used our numerical model to identify the parameter space and experimental modifications needed to improve the contrast. We will first describe the model used before going to discuss the experimental modification necessary to achieve an acceptable contrast in probe absorption.

g. Model used for simulation and computational details

Any analysis of the polarizer proposed above would require careful monitoring of the populations and coherences of the various Zeeman sub-levels involved in the system. A detailed diagram of all the relevant levels considered along with the relative transition strengths has been presented in Fig. 5.5. Due to power broadening, the $5P_{1/2}$, $F' = 1$ hyperfine level interacts with both the control and the signal optical fields (indicated by dashed lines), albeit at a large detuning, and these interactions have been taken into account in our model. However, we ignored the coherent coupling between $F = 2$ and the $5P_{1/2}$ manifold, because of the large frequency difference between $F = 1$ and $F = 2$ (~ 6.8 GHz for ^{87}Rb). Also, while the control beam is shown to be resonant in Fig. 5.5, ours is a general model where the control beam can be detuned from the $F' = 2$ level by an arbitrary value, say δ_p .

All the Zeeman sub-levels in the $5P_{1/2}$ ($6S_{1/2}$) manifold are assumed to decay at the same rate, $\gamma_a \sim 5.75$ MHz ($\gamma_b \sim 3.45$ MHz). We also assume a nominal cross-relaxation rate ($\gamma_g \sim 0.1$ MHz) between $F = 1$ and $F = 2$ hyperfine levels. Figure 5.12 shows the various decay channels and branching ratios in the system. Here, the individual decay rates between the Zeeman sub-levels are not explicitly shown but only the branching ratios

between the hyperfine levels, which were obtained by summing the decay rates of all possible transitions between the corresponding hyperfine levels. The decay rate between any two Zeeman sub-levels was calculated by assuming it to be proportional to the square of the matrix element of the corresponding transition, such that the sum of all such decay rates from the decaying level equaled the net decay from that level. For example, consider $m_F = 0$, $F' = 2$ sub-level which decays at a rate γ_a . The transition strengths for the σ_+ , σ_- , and π -transitions to the $F = 1$ ($F = 2$) are in the ratio 1:1:2 ($\sqrt{3}:\sqrt{3}:0$). Thus, the net decay rate between the $m_F = 0$, $F' = 2$ sub-level to the $m_F = -1, +1$ and 0 states of the $F = 1$ level were computed to be $\gamma_a/12$, $\gamma_a/12$ and $\gamma_a/3$ respectively and the decay to the $F = 2$ level was computed to be $\gamma_a/2$, since all the hyperfine levels in the $F = 2$ state are lumped together as a single state in our model. We have also taken into account the sourcing of atoms into the ground states from the $6S_{1/2}$ state via the $5P_{3/2}$ state (shown by dashed lines in Fig. 5.12). For our computations, these additional source terms were modeled using an “effective decay rate” directly from the hyperfine levels in the $6S_{1/2}$ state to the $5S_{1/2}$ manifold. A detailed calculation, taking into account the various branching ratios into and from all the hyperfine levels of the $5P_{3/2}$ state was used to determine these rates. However, the decay rate of each of the individual Zeeman sub-level in the $6S_{1/2}$ state was not considered, rather it was assumed that all of them decayed equally to the Zeeman sub-levels of the $F = 1$ and $F = 2$ levels at the respective “effective decay rates” previously determined. The ratio between the decay rates into the $5P_{1/2}$ and

$5P_{3/2}$ state from the $6S_{1/2}$ state was simply decided by the ratio of the explicit values of the transition strength of the D1 and D2 lines [25].

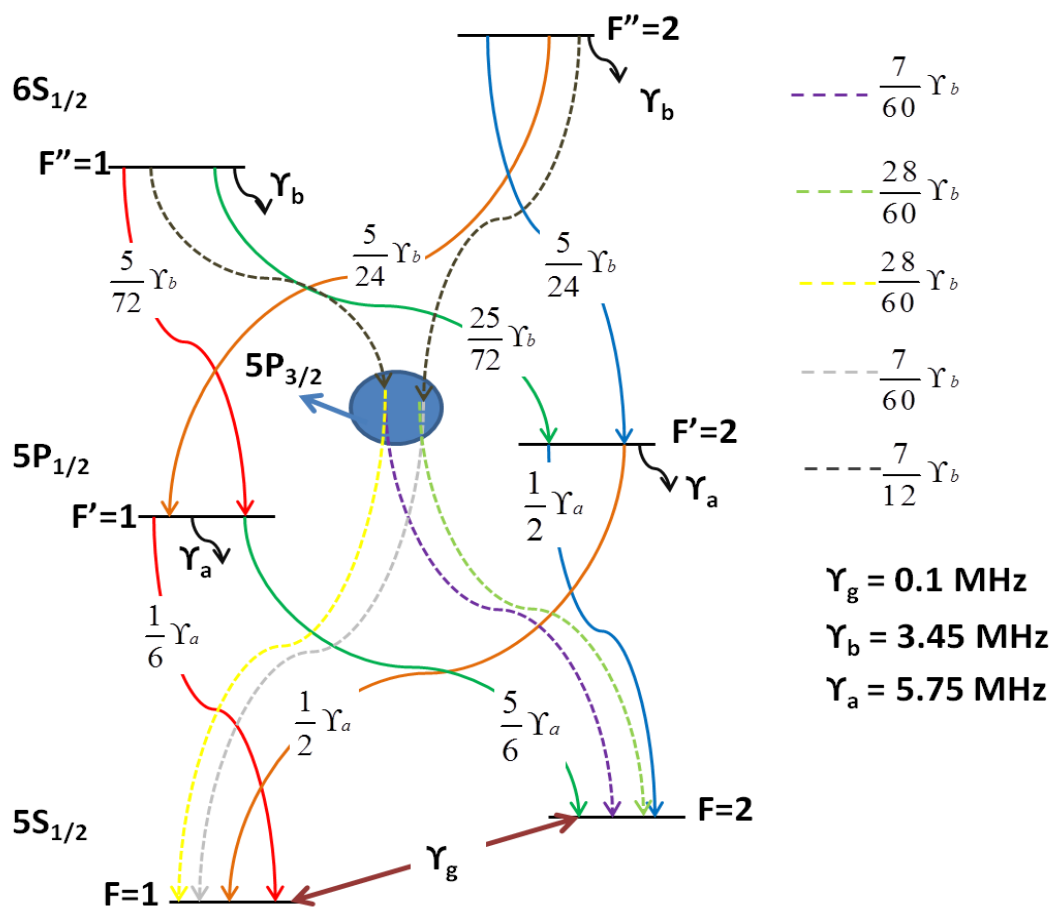


Figure 5.12 Decay rates and branching ratios between various levels in our model.

In addition to keeping track of the signs of the matrix elements involved in the transitions between the Zeeman sub-levels, it is also important to keep track of the explicit phase associated with the optical fields. In most cases, this phase can be factored out while transforming the Hamiltonian to the rotating basis. However, if any level has multiple pathways for excitation such that the pathways form a closed loop architecture, it is not possible to transform all the phases out of the Hamiltonian. Upon transformation

to the rotating basis, this results in the appearance of a so called “closed-loop phase” on one of the legs of the Hamiltonian which cannot be eliminated by any transformation, as shown in Fig. 5.13. In fact, changing the polarization of either the signal beam or the control beam from horizontal to vertical results in changing this closed-loop phase by π and thus the study of the Polarizer effect essentially boils down to studying the behavior of the system as this closed-loop phase is switched between 0 and π .

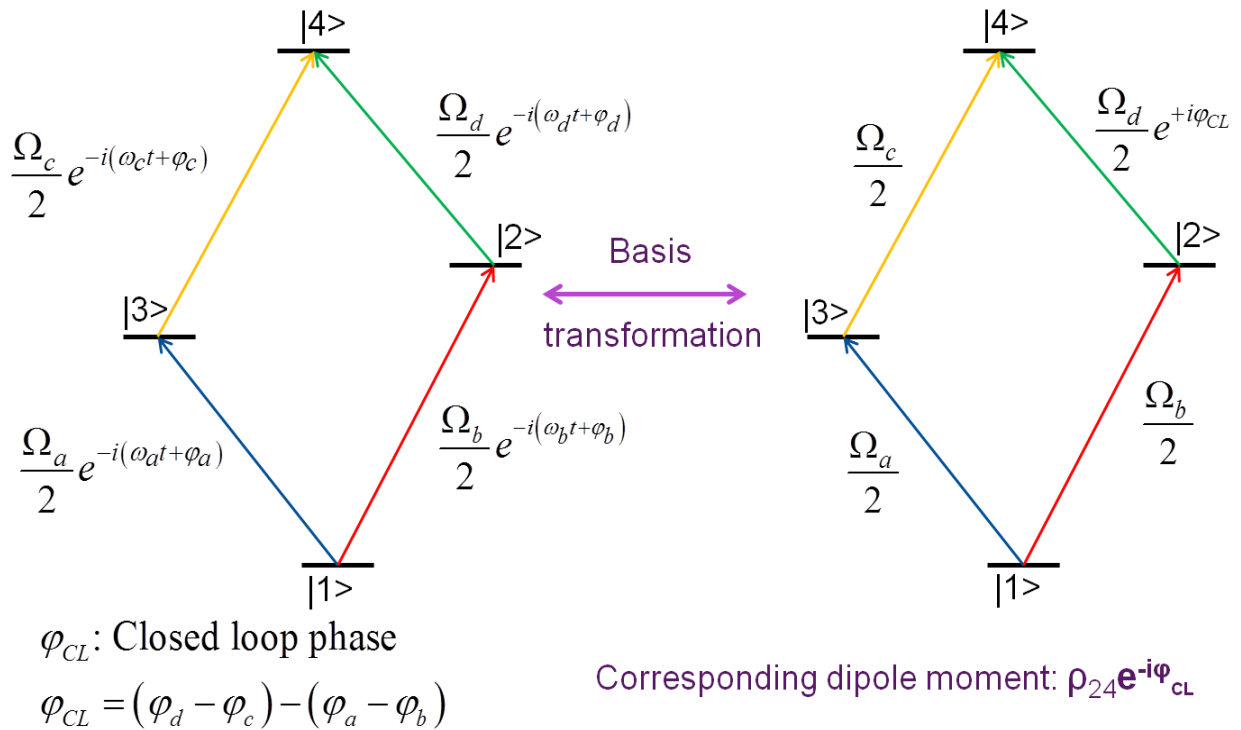


Figure 5.93 Effect of closed-loop architecture resulting from multiple excitation pathways between two levels.

In our model, we have up to a maximum of 20 levels. We used the Liouville equation, that describes the evolution of the density matrix in terms of a commutator between the density matrix and the Hamiltonian, to obtain the steady-state solution. The usual method

of vectorizing the density matrix and then inverting the coefficient matrix thus obtained, is not easy to handle as the size of the coefficient matrix is very large (400*400). In order to overcome this problem, we developed a novel algorithm which would compute the said coefficient matrix automatically, given the Hamiltonian and the source matrix. Briefly, we set each of the elements of the density matrix to unity one at a time while setting all the others to zero and repeatedly compute the commutator between the density matrix and the Hamiltonian. Once this procedure is repeated over all the elements of the density matrix, we would have computed the coefficient matrix. The source terms, as well as any other dephasing terms (such as collisional dephasing) are added in finally as a constant matrix. Details regarding the algorithm are presented in another section and is published here.²⁶

While averaging over the Doppler profile, we used the supercomputing cluster at Northwestern (QUEST) to perform our computations. Using 64 cores and computing the steady state solution for 512 values of detuning, each averaged over 800 points of the Doppler profile, we obtained the steady-state solution for our 20-level system in 3-4 minutes. With a smaller system, say for a 15-level system, we obtained the solution in a few seconds. Some of the results, thus obtained, have already been reproduced in Section 6. For all the simulations, a temperature of 500 Kelvin was used and the density of atoms was taken to be $\sim 10^{11}/\text{cm}^3$

h. Improvements to system and future work

In general, the quality of a polarizer is characterized by its extinction ratio, η , defined as the ratio of the transmitted intensity of light with its state of polarization (SOP) parallel to the transmission axis to the transmitted intensity of the same beam of light with its SOP perpendicular to the transmission axis. The minimum value of η that might be acceptable depends on the signal to noise ratio (SNR) desired in a particular application. For the SI application, for example, an SNR of about 5 would suffice, according to the Rose criterion.²⁷ For the optical logic gate, the SNR requirement could be even lower. This would translate directly to the η that can be achieved in our polarizer, assuming other sources of noise are negligible. The best case, shown in Fig. 5.7(b) corresponds to an $\eta \sim 2.5$. The value of η can be increased significantly by using higher optical densities of the Rb medium (resulting in very high absorption of light polarized perpendicular to the transmission axis) but this would also result in lowering of the transmission of light polarized along the transmission axis of the polarizer. Thus, the requirement of a high value of η needs to be balanced against maximum achievable transmission and this would again depend on the particular application at hand.

In order to increase the extinction ratio of our all-optical polarizer without sacrificing the maximum transmission achievable for a beam of light polarized along the transmission axis, it is necessary to make modifications to our system. One of the non-idealities in our system is that all the Zeeman sublevels in the $F = 1$ state are populated due to decay from various channels. Since the transition between the $F = 1, m_F = 0$ and the

$F' = 1, m_F = 0$ Zeeman sublevels is forbidden, application of a π -polarized optical pumping beam between the $F = 1$ and $F' = 1$ states would pump the atoms into the $F = 1, m_F = 0$ state, as required. However, we note that a π -transition is allowed between the $F = 1, m_F = 0$ and $F' = 2, m_F = 0$ Zeeman sublevels. Hence, if the interaction of the π -beam with $F' = 2$ is considered, it is not possible to obtain a time-independent Hamiltonian after switching to a rotating basis. In order to circumvent this complication, we made the simplifying assumption that the π -beam excites only the $F = 1 \rightarrow F' = 1$ transition. Although not necessary, we also assumed that the control beam only interacts with the $F' = 2$ level. Given the separation (0.816 GHz) between the $F' = 1$ and $F' = 2$ levels, these assumptions are valid for the power levels used in our simulation, as detailed later. The π -beam, expanded using a cylindrical lens and locked to $F = 1 \rightarrow F' = 1$ transition, needs to be brought in through a slot running parallel to the length of the Rb Cell.

However, application of this pumping beam alone is not sufficient, as there is decay from the intermediate ($5P$) levels into the $F = 2$ state, which is another non-ideality in our system. This mandates the need for another optical pumping beam from the $F = 2$ state to the $5P_{3/2}$ state. The net effect of this additional pumping beam was modeled as an increased decay rate from the $F = 2$ to $F = 1$ state. The maximum decay rate obtainable by the application of such a beam is γ_a , the radiative decay rate of the $5P_{3/2}$ manifold. We further note that the ratio of steady-state populations in the $F = 1$ and $F = 2$ states (in the absence of any field) can be estimated to be $\sim \gamma_a / \gamma_g$, where γ_g is the nominal decay rate from the $F = 1$ to $F = 2$ state. It is clear that we can increase the population in the $F = 1$

state by further decreasing γ_g , and this can be accomplished by using a buffer gas loaded cell. Figure 5.14 shows our model after the afore-mentioned changes are incorporated. As noted previously, to avoid unnecessary clutter, not all transition strengths are shown.

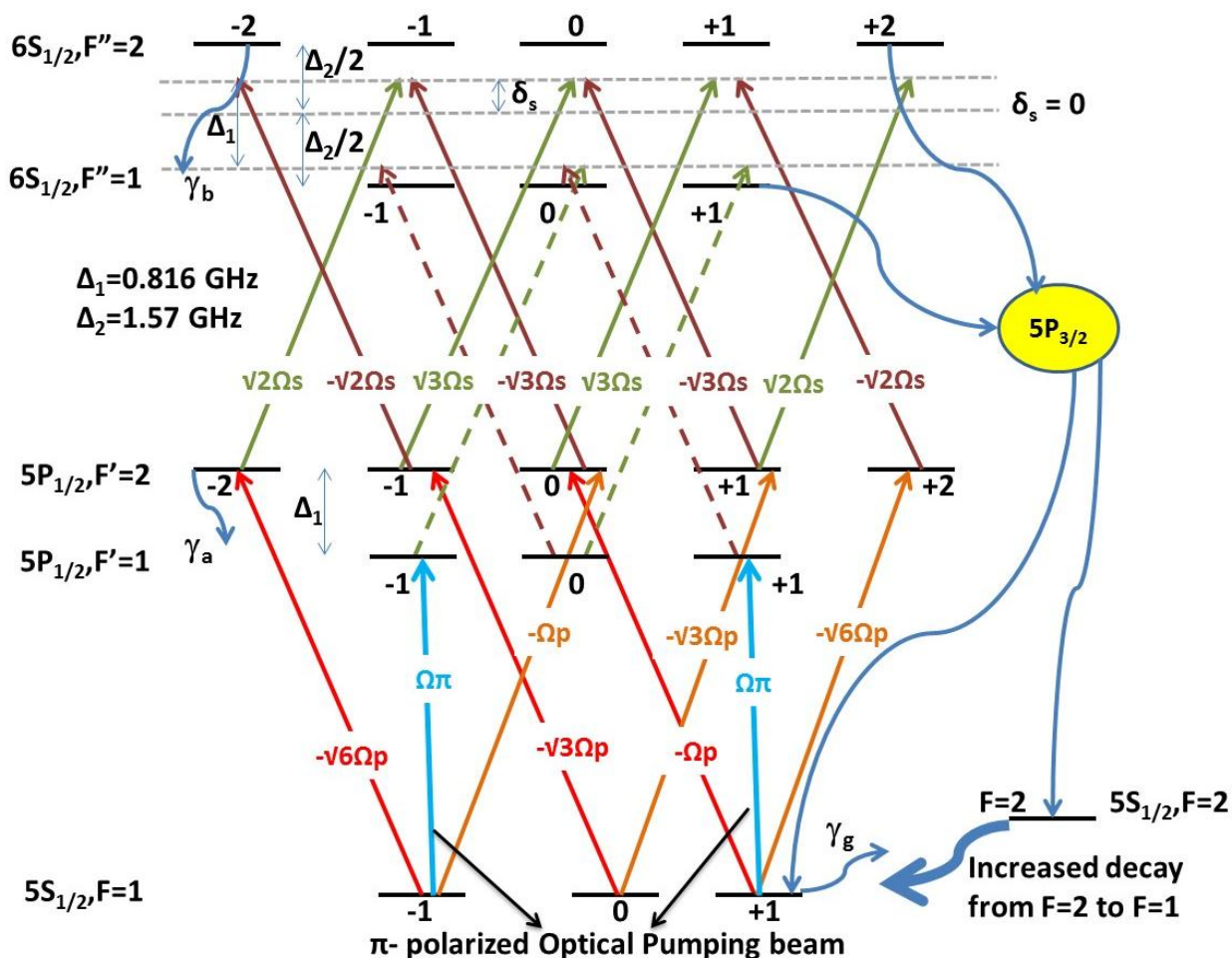


Figure 5.10 Modified model after addition of optical pumping beams and buffer gas.

A typical simulation result obtained by employing the modified system is shown in Fig. 5.15. Again, only the $F' = 2 \square F'' = 1$ transition is shown for the sake of brevity. As is evident from Fig. 5.15, at zero detuning, a signal beam with the same polarization as the

control beam is almost completely absorbed (0.00001% transmission) while nearly 90% of an orthogonally polarized beam is transmitted, corresponding to an $\eta \sim 10^5$, comparable to the best commercially available polarizers. For this particular simulation, we used the co-propagating geometry, the decay rate from the $F = 2$ to $F = 1$ state was set to be equal to the decay rate of the 5P manifold while the decay rate in the opposite direction was set (reduced due to buffer gas) to about 10 KHz. The Rabi frequencies of the control beam and the optical pumping beam were set to be 0.5 and 10 (in units of the natural linewidth of the 5P manifold $\gamma_a \sim 5.7$ MHz), respectively. The density of atoms was taken to be $10^{11}/\text{cm}^3$ and the temperature was set to 500K.

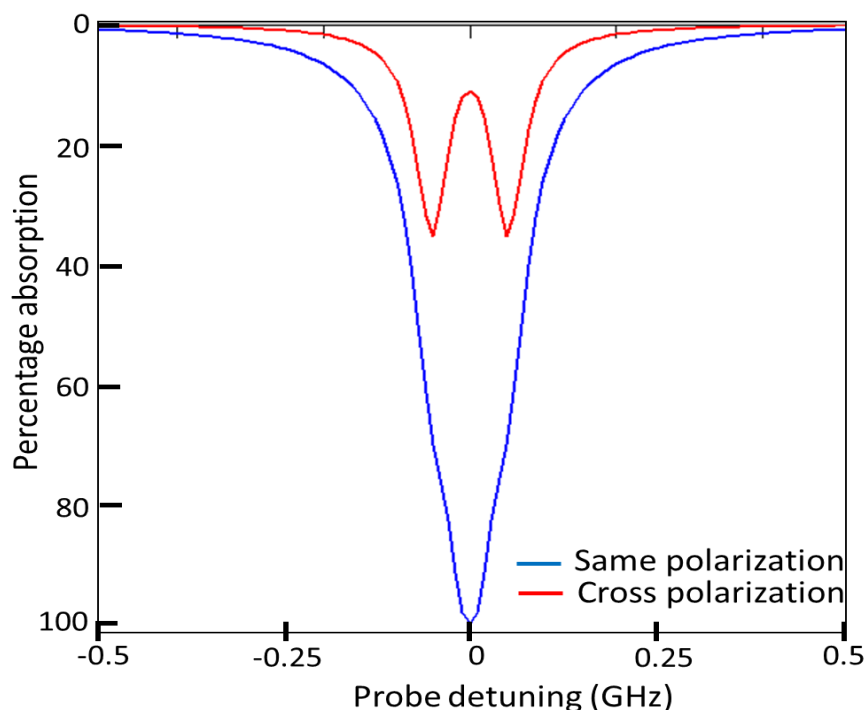


Figure 5.115 Numerical simulation of polarizer effect in the presence of two optical pumping beams and using a buffer gas loaded cell.

It should be possible to realize such a polarizer at a very low light level, using a tapered nanofiber (TNF) embedded in Rb vapor. In a TNF, the typical mode area is $\sim 0.2 \mu\text{m}^2$. Thus, assuming a saturation intensity of $3\text{mW}/\text{cm}^2$, a Rabi frequency of $10\gamma_a$ would correspond to a power of only $\sim 1 \text{ nW}$. Unlike the free space case, the maximum speed of operation in the TNF system would be limited by the transit time broadening ($\sim 60 \text{ MHz}$) rather than the natural linewidth of the $5P$ manifold ($\sim 6 \text{ MHz}$). To see why, note that the speed is limited by the rate at which atoms in the intermediate state relax to the ground state²⁸ and for a TNF system, this rate is effectively determined by the transit time. Finally, we note that the TNF system may be suitable only for demonstrating an all-optical logic gate but not for SI, for which the free space version of the polarizer is better suited.

CHAPTER 6 - OPTICALLY CONTROLLED WAVEPLATE

a. Schematic of optically controlled waveplate and all-optical switch

In an atomic system involving ladder type transitions, the presence of two different frequencies open up the possibility of controlling the behavior of the probe (upper leg) polarization by careful design of the pump parameters (lower leg). In particular, it is possible to make the vapor cell act as a waveplate. The mechanism for producing controlled polarization rotation, thus emulating a waveplate, is illustrated schematically in Figure 6.1a, using a cascaded atomic transition involving four levels where direct

excitation to the upper level from the ground state is dipole forbidden. We consider the $m_F=0$ Zeeman sublevel of a certain hyperfine level into which the atoms have been optically pumped, as the ground state. The lower leg is excited by a right-circularly polarized (σ_+) beam (control beam), tuned a few GHz below the transition frequency to the intermediate level. The control beam, therefore, produces an off-resonant excitation to only the $m_F=1$ Zeeman sublevel in the intermediate state. The probe, applied between the intermediate level and the upper level is chosen to be linearly polarized and hence has two components: σ_+ and σ_- . The σ_- component sees the effect of the atoms and because of the detuning, it sees only a real susceptibility with virtually no absorption, while the σ_+ component of the probe does not see any effect of the pump. The parameters of the control beam can be tuned to achieve the condition for a π phase-shift for the σ_- component only, so that at the output the linear polarization is rotated by 90 degrees.

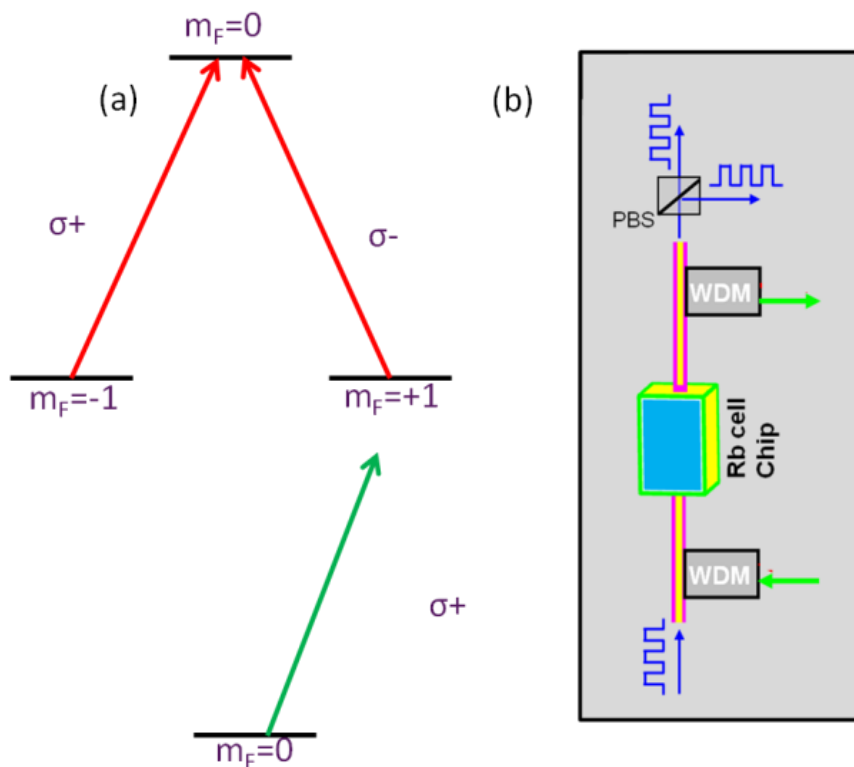


Figure 6.1 Schematic illustration of an optical switch using an optically controlled waveplate. See text for details.

It is relatively simple to see how the waveplate may be used as an all-optical switch, as shown in Fig. 6.1(b). Briefly, using a WDM coupler, the control beam and the probe are made to propagate through a Rb^{vapor} cell. Another WDM coupler is used to filter out the beams before the final polarizing beam splitter (PBS) placed at the output. The two ports of the PBS serve as the two output channels of the switch. Now, by turning the control beam on and off, the probe beam can be made to switch between the 2 ports of the PBS.

In our set-up, we utilized the $5S_{1/2}$ - $5P_{1/2}$ - $6S_{1/2}$ cascade system, for which the pump and probe beams are at 795 nm and 1323nm respectively. Theoretical and experimental investigations of an optically controlled waveplate using ladder transitions in Rb have

been carried out previously^{29,30}. However, both of these works employ the EIT effect where the upper leg is excited by a strong control field while the lower leg is probed by a weak optical field, and thus has fundamentally different characteristics than the system we have considered. For example, in above-mentioned references, since most of the atoms are present in the ground state, noticeable effect can be produced even when the control field is not very strong and is significantly detuned from any resonance. However, in our system, the fact that sufficient atoms have to be excited to the intermediate state necessitates that a stronger control field tuned closer to resonance. Of course, the primary reason for choosing the upper leg as the probe is the need for an all-optical switch at a telecommunication wavelength.

In Fig. 6.1(a), we showed a simplified set of energy levels in order to explain the basic process behind an optically controlled waveplate. In practice, however, it is extremely difficult to realize such an ideal system. We first note that it is virtually impossible to eliminate all the atoms from the $5S_{1/2}$, $F=1$, $m_F = \pm 1$ Zeeman sublevels via optical pumping. Hence, Zeeman sub-levels other than $m_F=1$ at the $5P_{1/2}$ manifold are also get coupled with the pump and probe optical fields. Furthermore, it is generally necessary to take into account both the hyperfine levels ($F'=1$ and $F'=2$) in the $5P_{1/2}$ manifold to account for Doppler broadening and power broadening. Thus, the full set of energy levels that need to be considered is quite large and the model employed for our system is discussed in the next section. For the remainder of the paper, the hyperfine levels in the

ground state are indicated by unprimed alphabets (F), those in the $5P_{1/2}$ level are primed (F') and those in the $6S_{1/2}$ level are double-primed (F'').

b. Comprehensive model used for numerical simulation

In previous analyses of similar systems, a simple model consisting of only the relevant hyperfine levels transitions was employed [29,30]. Reference 31³¹ goes into some detail, considering some of the Zeeman sub-levels, but makes use of some approximations about some of the density matrix elements to arrive at a somewhat approximate result. In our model, we considered all the Zeeman sub-levels which explicitly interact with an optical field (all sub-levels of the $F=2$, $F'=1,2$ and $F''=1$ hyperfine levels), while the $F=1$ hyperfine level and the $5P_{3/2}$ level were only considered as population transfer levels and hence all their sub-levels were lumped together as a single level. The full set of energy levels that we have incorporated in our model are shown in Fig. 6.2. The transition strengths indicated are expressed as multiples of the weakest transition, which in our case is the transition from the $F=2$, $m_F=0$ sub-level to the $F'=1$, $m_F=1$ sub-level, for example. We assume that the control beam is tuned below the $F=2 \rightarrow F'=1$ transition while the signal beam is detuned by an amount δ_s from the $F'=1 \rightarrow F''=1$ transition. Due to the Doppler width and power broadening, the $F'=2$ hyperfine level also interacts with both the control and the signal optical fields (indicated by dashed lines), albeit at a large detuning, and these interactions have been taken into account in our model. However, we ignored the coherent coupling between $F=1$ and the $5P_{1/2}$ manifold, because of the large frequency difference between $F=1$ and $F=2$ ($\sim 6.8\text{GHz}$ for ^{87}Rb).

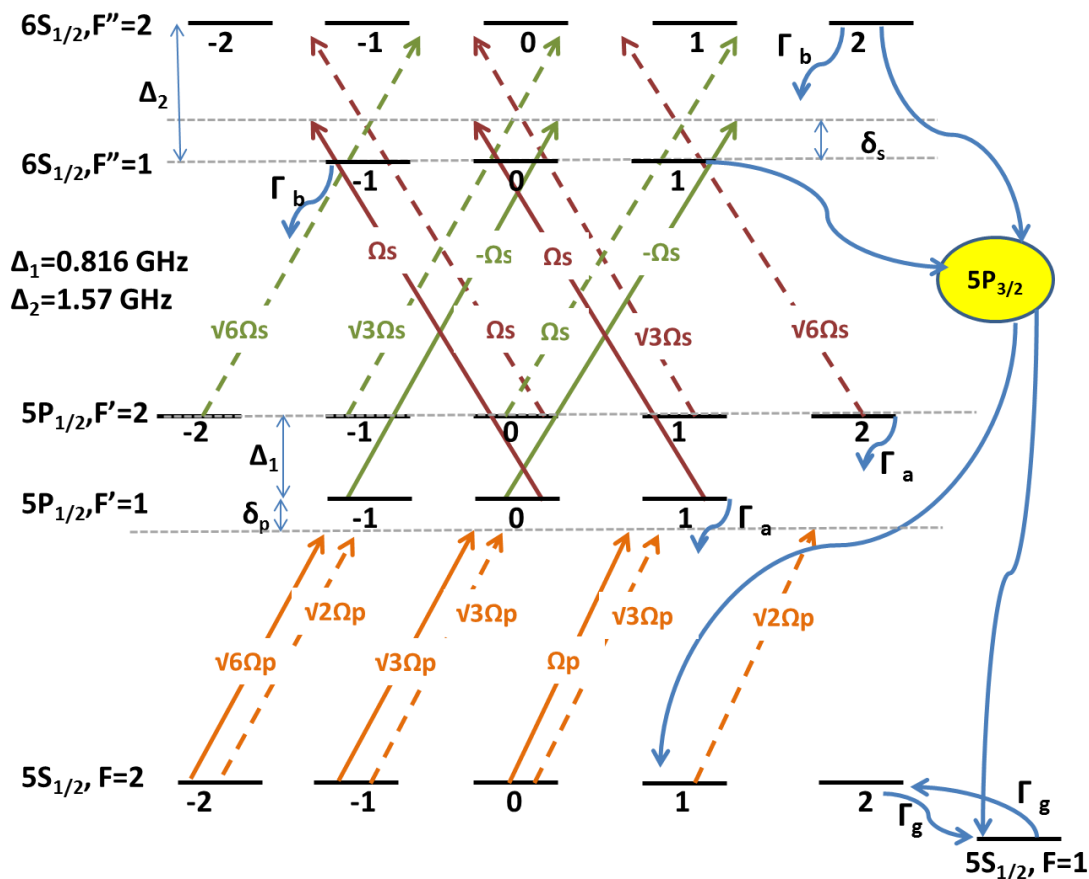


Figure 6.2 Model used for numerical computation. See text for more details.

All the Zeeman sub-levels in the $5P_{1/2}$ ($6S_{1/2}$) manifold are assumed to decay at the same rate, $\gamma_a \sim 5.75$ MHz ($\gamma_b \sim 3.45$ MHz). We also assume a nominal cross-relaxation rate ($\gamma_g \sim 0.01$ MHz) between the ground states. The decay rate between any two Zeeman sub-levels was calculated by assuming it to be proportional to the square of the matrix element of the corresponding transition, such that the sum of all such decay rates from the decaying level equaled the net decay from that level. For example, consider $m_F=0$, $F'=2$ ($F=1$) sub-level which decays at a rate γ_a . The transition strengths for the σ_+ , σ_- , and π -transitions to the $F=2$ ($F=1$) are in the ratio $\sqrt{3}:\sqrt{3}:0$ (1:1:2). Thus, the net decay rate

between the $m_F=0$, $F'=2$ sub-level to the $m_F=-1,+1$ and 0 states of the $F=2$ level were computed to be $\gamma_a/4$, $\gamma_a/4$ and 0 respectively and the decay to the $F=1$ level was computed to be $\gamma_a/2$, since all the hyperfine levels in the $F=1$ state are lumped together as a single state in our model. We have also considered the sourcing of atoms into the ground states from the $6S_{1/2}$ manifold via the $5P_{3/2}$ state. A detailed calculation, taking into account the various branching ratios into and from all the hyperfine levels of the $5P_{3/2}$ state was used to determine these “effective decay rates” directly from the $6S_{1/2}$ states to the ground states. Table 1 shows the “effective” branching ratios from each of the Zeeman sub-levels in the $6S_{1/2}$ manifold to the ground states. The ratio between the decay into the $5P_{1/2}$ and $5P_{3/2}$ state from the upper levels was decided by the ratio of the explicit values of the transition strength of the D1 and D2 lines.

	F''=2					F''=1			
		$m_F=-2$	$m_F=-1$	$m_F=0$	$m_F=1$	$m_F=2$	$m_F=-1$	$m_F=0$	$m_F=1$
	$m_F=-2$	0.68852	0.19426	0.05055	0	0	0.2361	0.09722	0
	$m_F=-1$	0.19426	0.47296	0.190277	0.07583	0	0.1667	0.11805	0.04861
F=2	$m_F=0$	0.05055	0.190277	0.45166	0.190277	0.05055	0.104167	0.125	0.104167
	$m_F=1$	0	0.07583	0.190277	0.47296	0.19426	0.04861	0.11805	0.1667
	$m_F=2$	0	0	0.05055	0.19426	0.68852	0	0.09722	0.2361
	$m_F=-1$	0.04722	0.03333	0.02083	0.009722	0	0.21296	0.1226875	0.1088
F=1	$m_F=0$	0.01944	0.023611	0.025	0.023611	0.01944	0.1226875	0.199	0.1226875
	$m_F=1$	0	0.009722	0.02083	0.03333	0.04722	0.1088	0.1226875	0.21296

Table 1. Effective Decay rates between excited states and ground states

We used the Liouville equation that describes the evolution of the density matrix in terms of a commutator between the density matrix and the Hamiltonian, to obtain the steady-state solution. The usual method of vectorizing the density matrix and then

inverting the coefficient matrix thus obtained, is not easy to handle as the size of the coefficient matrix is very large (400*400). In order to overcome this problem, we developed a novel algorithm which would compute the said coefficient matrix automatically, given the Hamiltonian and the source matrix. Briefly, we set each of the elements of the density matrix to unity one at a time while setting all the others to zero and repeatedly compute the commutator between the density matrix and the Hamiltonian. Once this procedure is repeated over all the elements of the density matrix, we would have computed the coefficient matrix. The source terms, as well as any other dephasing terms (such as collisional dephasing) are added in finally as a constant matrix. While averaging over the Doppler profile, we used the supercomputing cluster at Northwestern (QUEST) to perform our computations. Using 64 cores and computing the steady state solution for 512 values of detuning, each averaged over 800 points of the Doppler profile, we obtained the steady-state solution for our 15-level system in a few seconds.

c. Experimental set-up

The experimental configuration is illustrated schematically in Fig. 6.3. Briefly, beams from two tunable lasers (one at 795 nm, and the other at 1323 nm) are combined with a dichroic mirror (DCM). A part of the 795 light is sent to a reference vapor cell for saturated absorption spectroscopy and locking. The combined beams are sent through a vapor cell, shielded from magnetic fields with μ -metal. The cell is heated using bifilarly

wounded wires that do not add any magnetic fields. After passing through the cell, another DCM is used to split the light into two parts, and each frequency is detected with a separate detector. The control beam at 795 nm, initially polarized linearly, is passed through a quarter-wave-plate in order to produce circular polarization. The polarization of the signal beam, at 1323 nm, is controlled separately with a half-wave-plate. Ideally, the 1323 nm laser would also be locked at a particular frequency but this laser was found to be stable, so that locking it was not necessary.

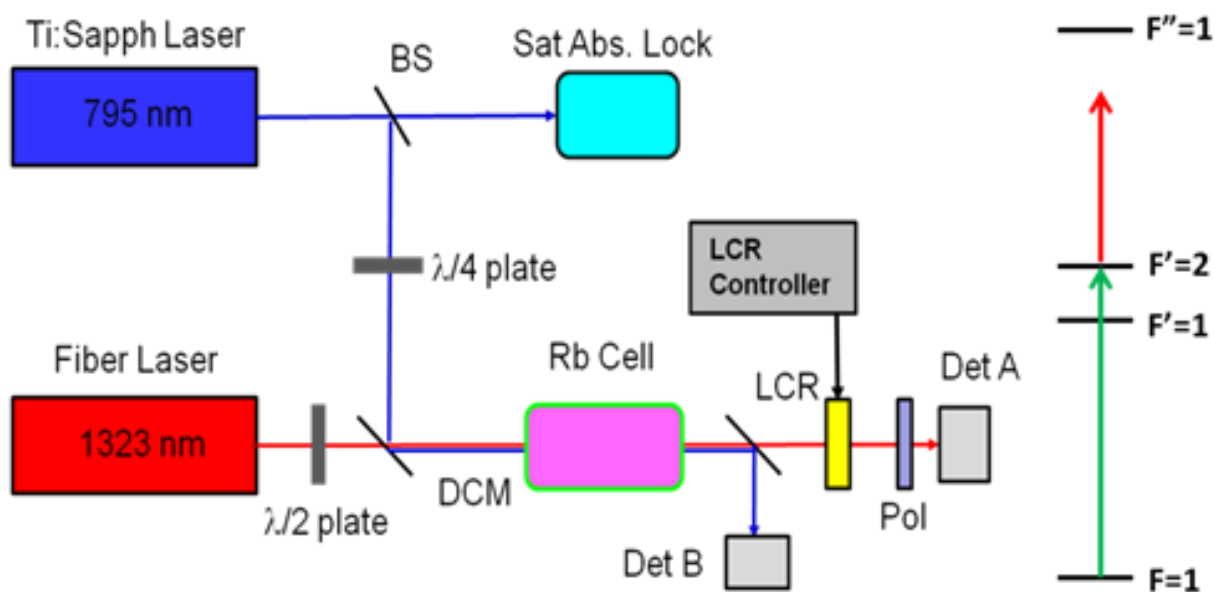


Figure 6.3 Experimental Set-up

In order to analyze the polarization of the signal beam after passing through the cell, we inserted an analyzer before detector A, consisting of a voltage-controlled liquid crystal retarder (LCR), whose fast axis is placed at 45 degrees to the initial polarization direction (say \hat{y}) of the signal beam, followed by a polarizer with its axis orthogonal to initial polarization of the signal beam. Having a orthogonal polarizer at the output is, in

general, not enough, as one cannot determine if the observed signal is a manifestation of polarization rotation alone or a combination of both rotation and absorption, unless of course the detector signal is at least as large as the far off-resonant signal. However, it can serve as a diagnostic tool in identifying the regions of large phase shift as the probe is scanned across the $6S_{1/2}$ manifold. The LCR produces a phase retardance between its orthogonal axes that depends non-linearly on the amount of voltage applied to the LCR controller which can be determined from a calibration curve provided by the manufacturer and verified independently by us. During our experiment, the control voltage to the LCR is scanned linearly from 0 V to 10 V, with 2 V and 8V corresponding to phase shifts of approximately π and 0, respectively for the wavelength that we are using. This particular arrangement of the analyzer provides us with a very large set of data points (corresponding to the LCR scan) from which to obtain the values of absorption coefficients and the phase rotations, thus making it more robust against noise in the system. The signal observed at the detector A can be ascertained by performing a Jones matrix analysis of the entire system, which is discussed next.

d. Jones matrix analysis

Let E_{in} be the signal field amplitude before the Rb cell and let \hat{y} be its polarization direction. Let $\hat{\sigma}_+ = -\left(\frac{\hat{x}+i\hat{y}}{\sqrt{2}}\right)$ and $\hat{\sigma}_- = \left(\frac{\hat{x}-i\hat{y}}{\sqrt{2}}\right)$ be the unit vectors corresponding to right (RCP) and left circular polarizations (LCP) respectively. Then, E_{in} can be represented in the circular polarization basis as $\vec{E}_{in} = E_0\hat{y} = E_{in+}\hat{\sigma}_+ + E_{in-}\hat{\sigma}_-$, where $E_{in+} = E_{in-} = i E_0/\sqrt{2}$

and E_0 is some arbitrary value. The field amplitude after the cell can be represented, in its most general form as $\vec{E}_{after\ cell} = E_{in+}e^{(-\alpha_+ + j\phi_+)}\hat{\sigma}_+ + E_{in-}e^{(-\alpha_- + j\phi_-)}\hat{\sigma}_-$, where (α_+, ϕ_+) and (α_-, ϕ_-) are the attenuations and phase rotations for the RCP and LCP part of the signal beam respectively after passing through the Rb vapor cell. With \hat{x} and \hat{y} as the basis for the Jones vector representation and after some algebraic manipulation, we find that the field amplitude after the cell can be represented as

$$E_{after\ cell} = \frac{iE_0}{2} e^{(-\alpha_- + j\phi_-)} \begin{bmatrix} -e^{(-\alpha_d + j\phi_d)} + 1 \\ -i(e^{(-\alpha_d + j\phi_d)} + 1) \end{bmatrix},$$

where

$$\begin{aligned} \alpha_d &= \alpha_+ - \alpha_- \\ \phi_d &= \phi_+ - \phi_- \end{aligned}$$

Thus, α_d and ϕ_d represent the differential absorption and phase rotation between the RCP and LCP parts of the signal beam. If θ represents the phase retardation produced by the LCR, then the Jones matrix for the LCR is given by

$$J_{LCR} = \begin{bmatrix} \exp(i\theta/2) & 0 \\ 0 & \exp(-i\theta/2) \end{bmatrix}$$

and the Jones matrix for the LCR whose axis is rotated by 45° is given by $J_{LCR45} = R^{-1}(45^\circ)J_{LCR}R(45^\circ)$ where $R(45^\circ)$ represents the rotation matrix for 45° and is given by

$$R(45) = \begin{bmatrix} \frac{1}{\sqrt{2}} & \frac{1}{\sqrt{2}} \\ -\frac{1}{\sqrt{2}} & \frac{1}{\sqrt{2}} \end{bmatrix}$$

Finally, the polarizer with its axis parallel to the \hat{y} axis has the Jones matrix representation

$$J_{XPol} = \begin{bmatrix} 1 & 0 \\ 0 & 0 \end{bmatrix}$$

Thus, the Jones vector for the signal observed at the detector A would be

$$J_{out} = J_{YPol} * J_{LCR45} * E_{aftercell}$$

Performing the calculations, we find that the intensity as seen by the detector A is given by,

$$I = \frac{E_0}{4} e^{-2\alpha} (1 + e^{-2\alpha_d} + (1 - e^{-2\alpha_d}) \sin \theta - 2e^{-\alpha_d} \cos \phi_d \cos \theta)$$

In Fig. 6.4(a), I is plotted for different values of ϕ_d (in degrees) and $\alpha_d = 0$ as the LCR phase retardance θ varies from 0 (left-end) to π (center) and back to 0 (right-end). As is evident from the figure, the signature for increasing differential phase rotation is the upward shift of the minimum and downward shift of the maximum of the curve until $\phi_d = 90^\circ$, at which point the signal is perfectly flat. For greater values of ϕ_d , the shape of the curve gets inverted until $\phi_d = \pi$. On the other hand, for non-zero values of α_d and $\phi_d = 0$, the minima of the curves get shifted inwards, the curves slope upward on either side of the minima and the central part of the curve is flattened out, as shown in Fig. 6.4(b). For non-zero values of both α_d and ϕ_d , the interpretation is not so straight-forward and one has to use 3 data points and invert the expression for I to obtain their values. The algebra is somewhat involved and we present only the final result –

$$y = e^{\alpha_d} = \sqrt{\frac{I_2^2(C_1 - C_3 - S_{3-1}) + I_1 I_2(C_3 - C_2 - S_{2-3}) + I_2 I_3(C_2 - C_1 - S_{1-2})}{I_2^2(C_3 - C_1 - S_{3-1}) + I_1 I_2(C_2 - C_3 - S_{2-3}) + I_2 I_3(C_1 - C_2 - S_{1-2})}} \text{ and}$$

$$\cos \phi_d = \frac{(I_2 - I_1)\left(y + \frac{1}{y}\right) + (I_1 S_2 - I_2 S_1)\left(\frac{1}{y} - y\right)}{2(I_2 C_1 - I_1 C_2)},$$

Where $C_j = \cos(\theta_j)$, $S_j = \sin(\theta_j)$, and $S_{j-k} = \sin(\theta_j - \theta_k)$, where θ_j is the phase rotations produced for some voltage, and I_j is the corresponding intensity seen by the detector.

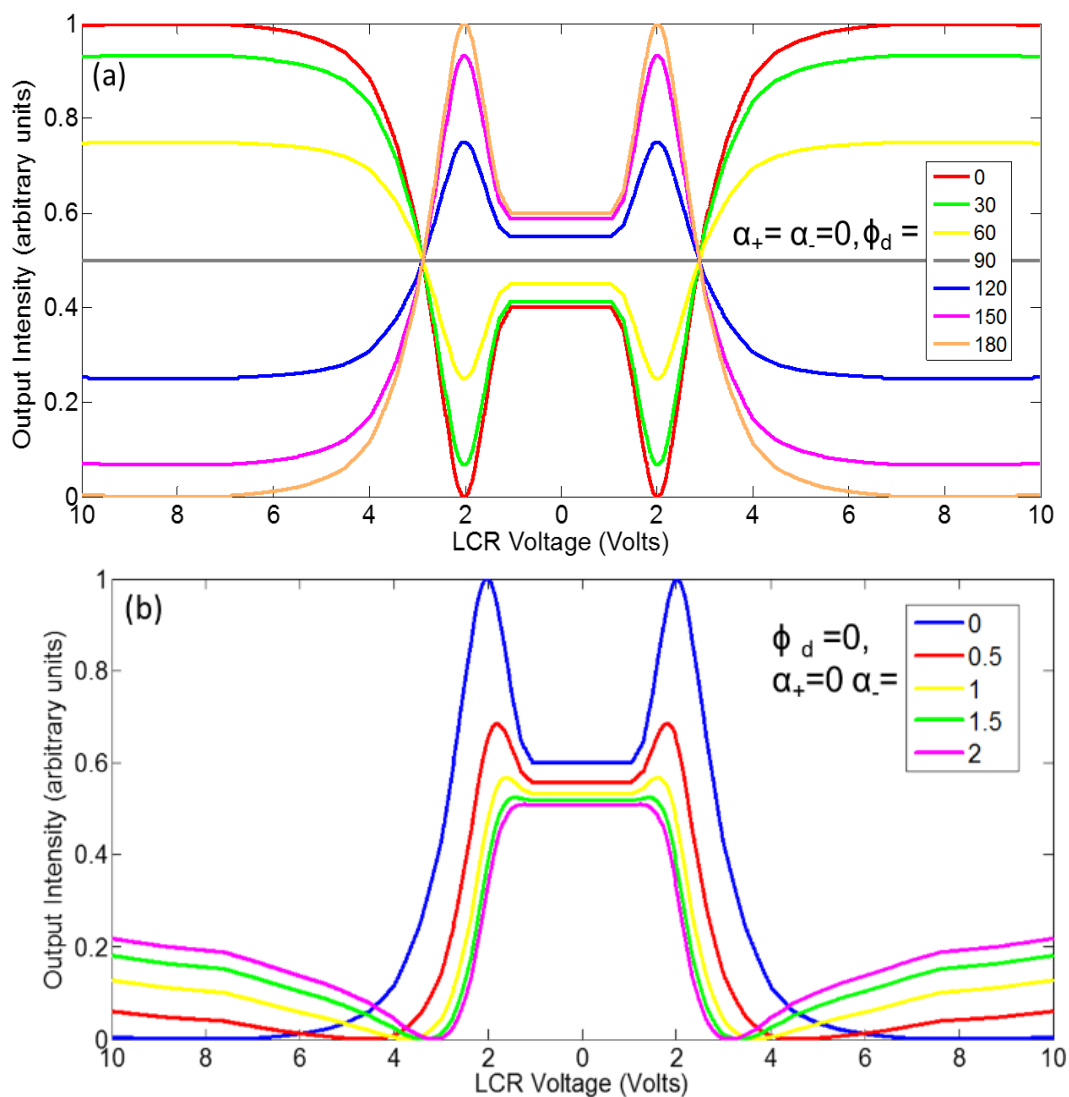


Figure 6.4 Ideal Output seen by detector for different values of a) ϕ_d with $\alpha_+ = \alpha_- = 0$ and b) α_- with $\phi_d = \alpha_+ = 0$

e. Results

The exact spectroscopic details of the $5P_{1/2}$ - $6S_{1/2}$ transitions depend critically on the control beam intensity and detuning, the temperature of the cell and probe detuning. Thus, as a diagnostic tool to identify regions of high phase shift, the LCR was removed

and an orthogonal polarizer was placed after the Rb cell. As the probe laser was scanned across the $6S_{1/2}$ manifold, the detuning of the control beam was varied in order to maximize the transmission through the orthogonal polarizer over the largest possible bandwidth. Then, the LCR was inserted and with the control beam and signal lasers positioned at the detunings previously determined, the exact differential phase rotation and absorption were determined. The temperature of the cell was maintained around 130° Celsius and pump power was about 600 mW obtained from a Ti-Sapphire laser. The probe laser was about 1 mW obtained from a fiber coupled semiconductor laser. Both beams were focused to a spot size of about 50 μm near the center of the Rb cell.

Figure 6.5 shows the results obtained when the LCR control voltage was scanned linearly from 10V to 0V and back up to 10V, for the co-propagating and counter-propagating geometries respectively. The control beam was right circularly polarized and the signal beam was vertically polarized. The pump was placed at a detuning of about 1.5 GHz. The blue trace (normalized from 0 to 1) corresponds to the situation when the control beam was blocked and can thus be treated as the reference signal, corresponding to 0 phase retardance. When the control beam is unblocked, our system acts as an optically controlled waveplate and the red trace is obtained. Comparing with the theoretical plots, we found that the phase shifts for the co- and counter-propagating $\phi_d \sim 180^\circ$ and $\alpha_d \sim 0$. The values obtained are consistent with those obtained using the analytical expressions

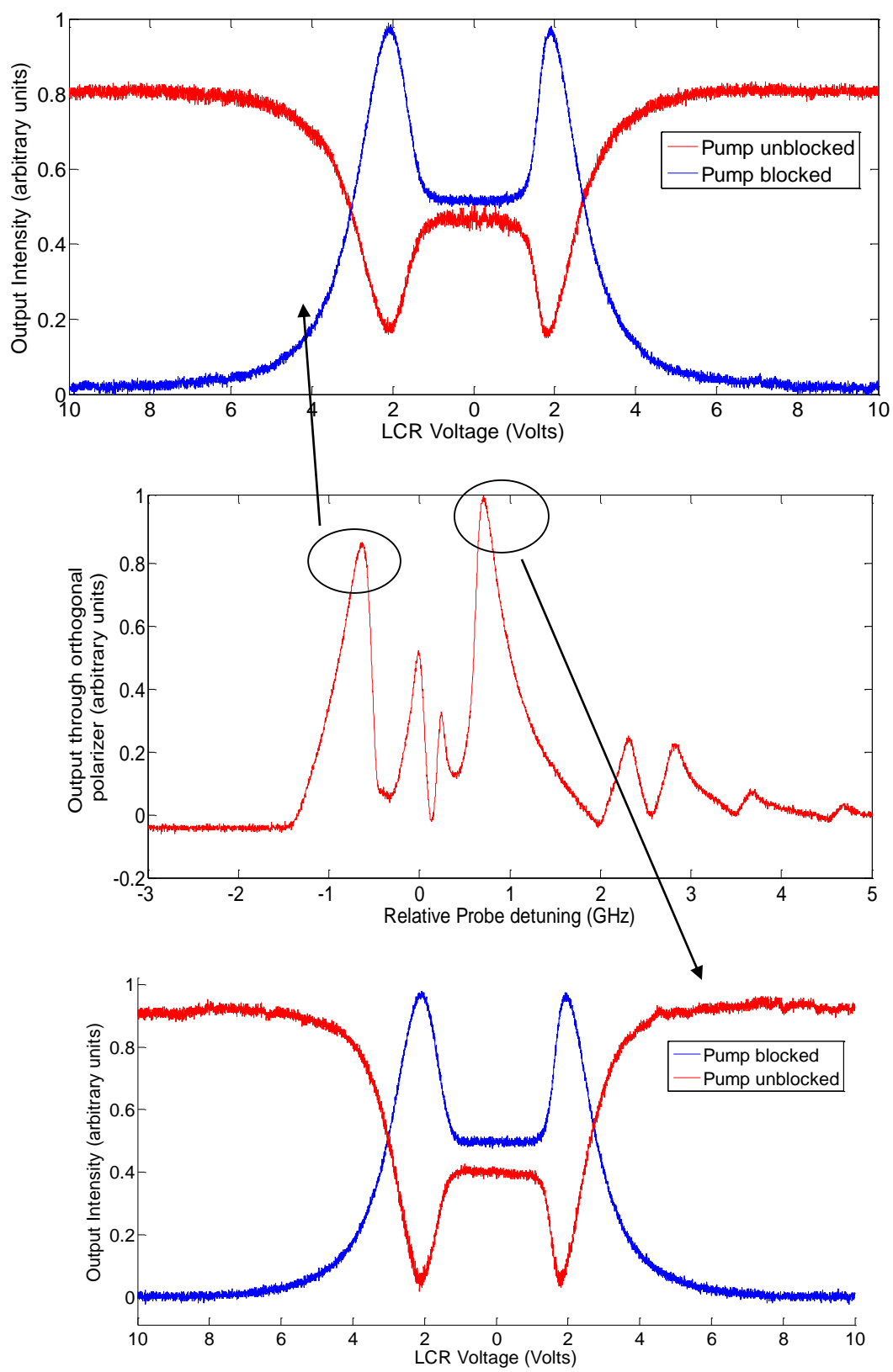


Figure 6.5 Observed experimental data showing differential phase rotation of $\sim 160^\circ$ and 180° respectively and no differential absorption. See text for more details

Fig. 6.6 shows the result obtained from numerical simulations using the model presented in section 2. We perform our calculations by setting Γ_a to unity and rescaling all parameters in units of Γ_a . The pump is resonant with the $F=1$ to $F'=2$ transition and the probe detuning (δ_s) ranges from $-1200\Gamma_a$ to $1200\Gamma_a$. Fig. 6.6(a) and 6.6(b) show the phase shift of the RCP and LCP parts of the signal beam introduced by the Rb medium and Fig. 6.6(c) shows the difference between them. Fig. 6.6(d)-6.6(f) show the corresponding figures for attenuation. As is evident from the figure, at a pump detuning of ~ 1.2 GHz and for Rb density of $10^{12}/\text{cm}^3$ and cell length of 7.5 cm, we can only produce a phase shift of about 180° with minimal differential absorption. The relevant parameters used for this particular simulation are as follows- the decay rates Γ_a , Γ_b and Γ_g are $2\pi*5.75 \text{ sec}^{-1}$, $2\pi*3.45 \text{ sec}^{-1}$ and $2\pi*0.1 \text{ sec}^{-1}$ respectively. The separation Δ , between $F'=1$ and $F'=2$ is $2\pi*814.5 \text{ sec}^{-1}$ ($= 141.4\Gamma_a$) and the Rabi frequencies have been chosen to be $\Omega_p = 100\Gamma_a$, and $\Omega_s = 0.1\Gamma_a$. The expressions used to calculate the attenuation and additional phase retardance introduced by the Rb medium are given by

Phase Shift:

$$\phi_+ = kL \frac{\beta_+}{2} \text{Re}(a_{13,4}\rho_{13,4} + a_{14,5}\rho_{14,5} + a_{12,7}\rho_{12,7} + a_{13,8}\rho_{13,8} + a_{14,9}\rho_{14,9})$$

$$\phi_- = kL \frac{\beta_-}{2} \text{Re}(a_{12,5}\rho_{12,5} + a_{13,6}\rho_{13,6} + a_{12,9}\rho_{12,9} + a_{13,10}\rho_{13,10} + a_{14,11}\rho_{14,11})$$

Attenuation:

$$\alpha_+ = kL\beta_+ \text{Im}(a_{13,4}\rho_{13,4} + a_{14,5}\rho_{14,5} + a_{12,7}\rho_{12,7} + a_{13,8}\rho_{13,8} + a_{14,9}\rho_{14,9})/2$$

$$\alpha_- = kL\beta_- \text{Im}(a_{12,5}\rho_{12,5} + a_{13,6}\rho_{13,6} + a_{12,9}\rho_{12,9} + a_{13,10}\rho_{13,10} + a_{14,11}\rho_{14,11})/2$$

And

$$\beta_{\pm} = b_{min}^2 \frac{3n_{atom}\Gamma\lambda^3}{4\pi^2\Omega_{min}},$$

where k is the wavevector of signal beam, L is the length of the cell, n_{atom} is the density of Rb atoms, Ω_{min} is the Rabi frequency for the weakest probe transition and the various a_{ij} 's are the ratios of the Rabi frequency (Ω_{ij}) of the $|i\rangle\text{-}|j\rangle$ transition to Ω_{min} . For example, $a_{12,7} = \Omega_{12,7}/\Omega_{14,9} = \sqrt{6}$. b_{min}^2 is the fraction of the atoms (<1) that decay along the transition corresponding to Ω_{min} , among all allowed decay channels from the decaying level. In our model, the amplitudes for all possible transitions from $|14\rangle$ are in the ratio $1:1:1:\sqrt{3}:\sqrt{6}$ and hence the fraction of atoms that decay along the different channels are in the ratio $1:1:1:3:6$. Thus, $b_{min}^2 = 1/(1 + 1 + 1 + 3 + 6) = 1/12$.

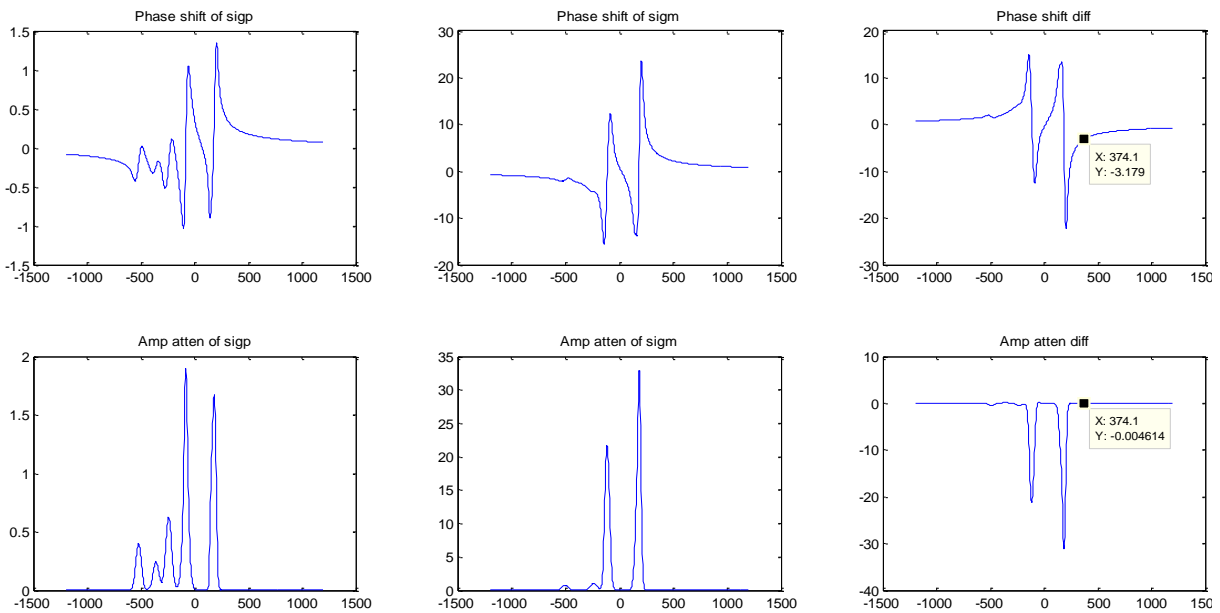


Figure 6.6 Numerical simulation of 15-level system showing phase shift and attenuation of the RCP and LCP parts

of the probe beam as a function of probe detuning. Here $\delta_c \sim 1.2$ GHz, $n_{\text{atom}} \sim 10^{12}/\text{cm}^3$ and

$\Omega_{\text{min}} = 100\Gamma_a$. See text for more details.

CHAPTER 7 N-LEVEL ALGORITHM

For some situations in atomic and molecular physics, it is necessary to consider a system with many energy levels, such as excitation involving many hyperfine levels and/or Zeeman sublevels. The Liouville equation that describes the evolution of the density matrix is expressed in terms of a commutator between the density matrix and the Hamiltonian, as well as additional terms that account for decay and redistribution []. To find solutions to this equation in steady-state or as a function of time, it is convenient first to reformulate the Liouville equation by defining a vector corresponding to the elements of the density operator, and determining the corresponding time evolution matrix. To find the steady-state solution in a closed system, it is also necessary to eliminate one of the diagonal elements of the density matrix from these equations, because of redundancy. For a system of N atoms, the size of the evolution matrix is $N^2 \times N^2$, and the size of the reduced matrix is $(N^2-1) \times (N^2-1)$. When N is very large, evaluating the elements of these matrices becomes very cumbersome. In this paper, we describe an algorithm that can produce the evolution matrix in an automated fashion, for an arbitrary value of N . We then apply this algorithm to a fifteen level atomic system used for producing optically controlled polarization rotation.

a. A Two Level System

To illustrate the basic idea behind the algorithm, we first consider the simplest case: a two-level system of atoms excited by a monochromatic field [], as illustrated in figure 1. Here, $\hbar\omega_1$ and $\hbar\omega_2$ are the energies of levels $|1\rangle$ and $|2\rangle$, and ω is the frequency of the laser, with a Rabi frequency of Ω_0 [].

The Hamiltonian, under electric dipole and rotating wave approximations, is given as

$$\mathcal{H} = \hbar \begin{pmatrix} \omega_1 & \frac{\Omega_0}{2} e^{i(\omega t - kz_0 + \phi)} \\ \frac{\Omega_0}{2} e^{-i(\omega t - kz_0 + \phi)} & \omega_2 \end{pmatrix} \quad (1)$$

where k is the wavenumber of the laser, z_0 is the position of the atom, and ϕ is the phase of the field. Without loss of generality, we set $z_0=0$ and $\phi=0$ in what follows. The corresponding two-level state vector for each atom is

$$|\psi\rangle = \begin{bmatrix} C_1(t) \\ C_2(t) \end{bmatrix}, \quad (2)$$

which obeys the Schrodinger equation

$$i\hbar \frac{\partial |\psi\rangle}{\partial t} = \mathcal{H} |\psi\rangle \quad (3)$$

To simplify the calculation, we convert the equations to the rotating wave frame by carrying out the following transformation into an interaction picture:

$$|\tilde{\psi}\rangle \equiv \begin{bmatrix} \tilde{C}_1(t) \\ \tilde{C}_2(t) \end{bmatrix} = R |\psi\rangle \quad (4a)$$

where

$$R = \begin{bmatrix} e^{i\omega_1 t} & 0 \\ 0 & e^{i\omega_2 t} \end{bmatrix} \quad (4b)$$

The Schroedinger equation now can be written as

$$i\hbar \frac{\partial |\tilde{\psi}\rangle}{\partial t} = \tilde{\mathcal{H}} |\tilde{\psi}\rangle \quad (5a)$$

where

$$\tilde{\mathcal{H}} = \hbar \begin{pmatrix} 0 & \frac{\Omega_0}{2} \\ \frac{\Omega_0}{2} & -\delta \end{pmatrix} \quad (5b)$$

$$\delta = \omega - (\omega_2 - \omega_1) \quad (5c)$$

The time independent Hamiltonian shown in equation 5b can also be derived easily without any algebraic manipulation. To see how, consider the diagram shown in figure 1(b), where we have added the number of photons as a quantum number in designating the quantum states. Thus, for example, $|N,1\rangle$ represents a joint quantum system where the number of photons in the laser field is N , and the atom is in state 1, and so on. Of course, a laser, being in a coherent state, is a linear superposition of number states, with a mean photon number $\langle N \rangle$, assumed to be much larger than unity. In the presence of such a field, the interaction takes place between near-degenerate states, namely $|N,2\rangle$ and $|N+1,1\rangle$, for example, with a coupling rate of $\Omega_0/2$, where $\Omega_N \propto \sqrt{N}$. Since the mean value of N is assumed to be very large, and much larger than its variance, one can assume

the mean value of Ω_N , defined as Ω_0 to be proportional to $\sqrt{\langle N \rangle}$. Under this approximation, we see that the coupling between any neighboring, near-degenerate pair of states is Ω_0 , and the energies of these states differ by δ . If we choose the energy of $|N+1,1\rangle$ to be 0, arbitrarily, then the energy of $|N,2\rangle$ is $-\hbar\delta$. The interaction is contained within a given manifold, so that a difference in energy (by $\hbar\omega$) between neighboring manifold is of no consequence in determining the evolution. These considerations directly lead to the Hamiltonian of equation 5(b). For a system involving more than two levels, a similar observation can be employed to write down the time-independent Hamiltonian by inspection, as we will show later.

The decay of the excited state amplitude, at the rate of Γ can be taken into account by adding a complex term to the Hamiltonian, as follows:

$$\tilde{\mathcal{H}}' = \hbar \begin{bmatrix} 0 & \frac{\Omega_0}{2} \\ \frac{\Omega_0}{2} & -\frac{i\Gamma}{2} - \delta \end{bmatrix} \quad (6)$$

For this modified Hamiltonian, the equation of evolution for the interaction picture density operator can be expressed as

$$\frac{\partial}{\partial t} \tilde{\rho} = \frac{\partial}{\partial t} \tilde{\rho}_{ham} + \frac{\partial}{\partial t} \tilde{\rho}_{source} + \frac{\partial}{\partial t} \tilde{\rho}_{trans-decay} \equiv Q \quad (7)$$

where the 2nd term in the middle accounts for the influx of atoms into a state due to decay from another state, and the 3rd term stands for any dephasing unaccompanied by population decay, often called transverse decay. In the case of a two level system, we have:

$$\frac{\partial}{\partial t} \tilde{\rho}_{ham} = -\frac{i}{\hbar} [\tilde{\mathcal{H}}' \tilde{\rho} - \tilde{\rho} \tilde{\mathcal{H}}'^*] \quad (8a)$$

$$\frac{\partial}{\partial t} \tilde{\rho}_{source} = \begin{bmatrix} \Gamma \tilde{\rho}_{22} & 0 \\ 0 & 0 \end{bmatrix} \quad (8b)$$

$$\frac{\partial}{\partial t} \tilde{\rho}_{trans-decay} = \begin{bmatrix} 0 & -\gamma_d \tilde{\rho}_{12} \\ -\gamma_d \tilde{\rho}_{21} & 0 \end{bmatrix} \quad (8c)$$

For simplicity, we ignore the dephasing term in 8c.

Substituting eqn. 6 into eqn. 8a, we get:

$$\frac{\partial}{\partial t} \tilde{\rho}_{ham} = \begin{pmatrix} \frac{1}{2} i \Omega_0 (\tilde{\rho}_{12} - \tilde{\rho}_{21}) & \frac{1}{2} i ((i\Gamma - 2\delta) \tilde{\rho}_{12} + \Omega_0 (\tilde{\rho}_{11} - \tilde{\rho}_{22})) \\ -\frac{1}{2} i ((-i\Gamma - 2\delta) \tilde{\rho}_{21} + \Omega_0 (\tilde{\rho}_{11} - \tilde{\rho}_{22})) & \frac{1}{2} (-i \Omega_0 (\tilde{\rho}_{12} - \tilde{\rho}_{21}) - 2\Gamma \tilde{\rho}_{22}) \end{pmatrix} \quad (10)$$

Substituting eqns. 8 and 10 into eqn. 7, we get

$$\begin{aligned} \frac{\partial}{\partial t} \tilde{\rho} &= \frac{\partial}{\partial t} \begin{pmatrix} \tilde{\rho}_{11} & \tilde{\rho}_{12} \\ \tilde{\rho}_{21} & \tilde{\rho}_{22} \end{pmatrix} = \begin{pmatrix} \frac{1}{2} i \Omega_0 (\tilde{\rho}_{12} - \tilde{\rho}_{21}) + \Gamma \tilde{\rho}_{22} & \frac{1}{2} i (i(\Gamma + 2i\delta) \tilde{\rho}_{12} + \Omega_0 (\tilde{\rho}_{11} - \tilde{\rho}_{22})) \\ -\frac{1}{2} i ((-i\Gamma - 2\delta) \tilde{\rho}_{21} + \Omega_0 (\tilde{\rho}_{11} - \tilde{\rho}_{22})) & \frac{1}{2} (-i \Omega_0 (\tilde{\rho}_{12} - \tilde{\rho}_{21}) - 2\Gamma \tilde{\rho}_{22}) \end{pmatrix} \\ &= Q \equiv \begin{pmatrix} Q_{11} & Q_{12} \\ Q_{21} & Q_{22} \end{pmatrix} \end{aligned} \quad (11)$$

In general, each of the matrix elements Q_{ij} can depend on all the ρ_{ij} . In order to find the steady state solution, it is convenient to construct the following vector

$$A = \begin{bmatrix} \tilde{\rho}_{11} \\ \tilde{\rho}_{12} \\ \tilde{\rho}_{21} \\ \tilde{\rho}_{22} \end{bmatrix} \quad (12)$$

Equation 11 can now be expressed as a matrix equation

$$\frac{\partial}{\partial t} A = MA \quad (13)$$

where M is a (4×4) matrix, represented formally as:

$$M = \begin{bmatrix} M_{11} & M_{12} & M_{13} & M_{14} \\ M_{21} & M_{22} & M_{23} & M_{24} \\ M_{31} & M_{32} & M_{33} & M_{34} \\ M_{41} & M_{42} & M_{43} & M_{44} \end{bmatrix}$$

Of course, the elements of this matrix can be read-off from eqn. 11. However, this task is quite cumbersome for an N -level system. Thus, it is useful to seek a general rule for finding this element without having to write down eqn. 11 explicitly. Later on in this paper, we establish such a rule, and specify the algorithm for implementing it. Here, we can illustrate this rule with some explicit examples:

$$M_{11} = Q_{11}, \text{ if we set } \tilde{\rho}_{11} = 1 \text{ and } \tilde{\rho}_{ij(ij \neq 11)} = 0 \text{ in eqn. 7;}$$

$$M_{12} = Q_{11}, \text{ if we set } \tilde{\rho}_{12} = 1 \text{ and } \tilde{\rho}_{ij(ij \neq 12)} = 0 \text{ in eqn. 7;}$$

$$M_{13} = Q_{11}, \text{ if we set } \tilde{\rho}_{21} = 1 \text{ and } \tilde{\rho}_{ij(ij \neq 21)} = 0 \text{ in eqn. 7;}$$

$$M_{14} = Q_{11}, \text{ if we set } \tilde{\rho}_{22} = 1 \text{ and } \tilde{\rho}_{ij(ij \neq 22)} = 0 \text{ in eqn. 7;}$$

$$M_{21} = Q_{12}, \text{ if we set } \tilde{\rho}_{11} = 1 \text{ and } \tilde{\rho}_{ij(ij \neq 11)} = 0 \text{ in eqn. 7;}$$

$$M_{22} = Q_{12}, \text{ if we set } \tilde{\rho}_{12} = 1 \text{ and } \tilde{\rho}_{ij(ij \neq 12)} = 0 \text{ in eqn. 7;}$$

$$M_{23} = Q_{12}, \text{ if we set } \tilde{\rho}_{21} = 1 \text{ and } \tilde{\rho}_{ij(ij \neq 21)} = 0 \text{ in eqn. 7;}$$

$$M_{24} = Q_{12}, \text{ if we set } \tilde{\rho}_{22} = 1 \text{ and } \tilde{\rho}_{ij(ij \neq 22)} = 0 \text{ in eqn. 7;}$$

and so on... (14)

This is the key element of the algorithm presented in this paper. Explicitly, in a computer program, such as the one in Appendix A, every time a parameter is changed, the elements of the M matrix are obtained by evaluating equation 7, while setting all but one of the elements of the density matrix to zero. For numerical integration as a function of time, one can then use a Taylor expansion to solve equation 13.

To find the steady-state solution, we set $\frac{\partial}{\partial t} A = 0$, so that:

$$\begin{bmatrix} M_{11} & M_{12} & M_{13} & M_{14} \\ M_{21} & M_{22} & M_{23} & M_{24} \\ M_{31} & M_{32} & M_{33} & M_{34} \\ M_{41} & M_{42} & M_{43} & M_{44} \end{bmatrix} \begin{bmatrix} \tilde{\rho}_{11} \\ \tilde{\rho}_{12} \\ \tilde{\rho}_{21} \\ \tilde{\rho}_{22} \end{bmatrix} = 0 \quad (15)$$

Expanding this equation, we get:

$$\begin{cases} M_{11}\tilde{\rho}_{11} + M_{12}\tilde{\rho}_{12} + M_{13}\tilde{\rho}_{21} = -M_{14}\tilde{\rho}_{22} \\ M_{21}\tilde{\rho}_{11} + M_{22}\tilde{\rho}_{12} + M_{23}\tilde{\rho}_{21} = -M_{24}\tilde{\rho}_{22} \\ M_{31}\tilde{\rho}_{11} + M_{32}\tilde{\rho}_{12} + M_{33}\tilde{\rho}_{21} = -M_{34}\tilde{\rho}_{22} \\ M_{41}\tilde{\rho}_{11} + M_{42}\tilde{\rho}_{12} + M_{43}\tilde{\rho}_{21} = -M_{44}\tilde{\rho}_{22} \end{cases} \quad (16)$$

For a closed system, there cannot be any net influx or outflux of atoms from the system.

Thus, the rate of change of one of the diagonal (population) terms of the density matrix is the negative sum of the rates of change of the other diagonal (population) terms. Thus, one of the equations in the above system of equations is rendered redundant. We also know that for a closed system, sum of the diagonal elements of the density matrix equals unity. In the case of the two level system, we thus have $\tilde{\rho}_{11} + \tilde{\rho}_{22} = 1$. We can thus choose

to eliminate the last equation, for example, and replace $\tilde{\rho}_{22}$ with $(1-\tilde{\rho}_{11})$ in the remaining three equations, to get

$$\begin{bmatrix} M_{11} & M_{12} & M_{13} \\ M_{21} & M_{22} & M_{23} \\ M_{31} & M_{32} & M_{33} \end{bmatrix} \begin{bmatrix} \tilde{\rho}_{11} \\ \tilde{\rho}_{12} \\ \tilde{\rho}_{21} \end{bmatrix} \equiv M' \begin{bmatrix} \tilde{\rho}_{11} \\ \tilde{\rho}_{12} \\ \tilde{\rho}_{21} \end{bmatrix} = \begin{bmatrix} M_{14} \\ M_{24} \\ M_{34} \end{bmatrix} \tilde{\rho}_{11} - \begin{bmatrix} M_{14} \\ M_{24} \\ M_{34} \end{bmatrix} \quad (17a)$$

so that

$$\begin{bmatrix} (M_{11} - M_{14}) & M_{12} & M_{13} \\ (M_{21} - M_{24}) & M_{22} & M_{23} \\ (M_{31} - M_{34}) & M_{32} & M_{33} \end{bmatrix} \begin{bmatrix} \tilde{\rho}_{11} \\ \tilde{\rho}_{12} \\ \tilde{\rho}_{21} \end{bmatrix} = - \begin{bmatrix} M_{14} \\ M_{24} \\ M_{34} \end{bmatrix} \quad (17b)$$

Here, we have defined M' as the reduced matrix resulting from M after eliminating the last row and column, for convenience of discussion during the presentation of the general algorithm later on. To simplify the notation further, we define:

$$B \equiv \begin{bmatrix} \tilde{\rho}_{11} \\ \tilde{\rho}_{12} \\ \tilde{\rho}_{21} \end{bmatrix}, \quad S \equiv \begin{bmatrix} M_{14} \\ M_{24} \\ M_{34} \end{bmatrix}, \quad W \equiv \begin{bmatrix} (M_{11} - M_{14}) & M_{12} & M_{13} \\ (M_{21} - M_{24}) & M_{22} & M_{23} \\ (M_{31} - M_{34}) & M_{32} & M_{33} \end{bmatrix} \quad (18)$$

Using these definitions in eqn. 17, we get:

$$WB = -S$$

Thus, the steady-state solution is simply given by:

$$B = -W^{-1}S \quad (19)$$

In a computer code, such as the one in Appendix A, the elements of W and S can be determined in an automated fashion by using a simple algorithm based on a generalization of this example. We get the values of $\tilde{\rho}_{11}$, $\tilde{\rho}_{12}$, and $\tilde{\rho}_{21}$ by using eqn. 19. Using the condition $\tilde{\rho}_{11} + \tilde{\rho}_{22} = 1$, we can then find the value of $\tilde{\rho}_{22}$.

For the 2-level system, the elements of M , W and S can be worked out by hand, without employing the general rules, with relative ease. However, for arbitrarily large systems, it can become exceedingly cumbersome. In what follows, we describe a compact algorithm for determining the elements of M , W and S for a system with N energy levels.

To start with, determine the elements of the complex effective Hamiltonian of eqn. 6, as well as the elements of $\tilde{\rho}_{source}$ for the N -level system. These matrices can be used to calculate the elements of Q , as defined in eqns. 7 and 11. The elements of M can then be found by using the following algorithm. Let M_{np} denote the element corresponding to the n -th row and p -th column of the M matrix. Similarly, let $Q_{\alpha\beta}$ denote the element corresponding to the α -th row and β -th column of the Q matrix, and $\tilde{\rho}_{\varepsilon\sigma}$ denote the elements corresponding to the ε -th row and σ -th column of the $\tilde{\rho}$ matrix. Then one can use the following prescription to obtain M_{np} :

$M_{np} = Q_{\alpha\beta}$ if we set $\tilde{\rho}_{\varepsilon\sigma}=1$ and $\tilde{\rho}_{ij(ij \neq \varepsilon\sigma)}=0$ in eqn. 7.

Thus, the crux of the algorithm is to obtain a way of finding $\alpha, \beta, \varepsilon$ and γ efficiently, for a given set of values of $\{n, p\}$. These indices are obtained as follows:

$$\beta = \text{nzrem}[n/N]; \quad \alpha = 1 + (n - \beta)/N; \quad \sigma = \text{nzrem}[p/N]; \quad \varepsilon = 1 + (p - \sigma)/N \quad (20)$$

where *nzrem* is a user-defined function prescribed as follows: $\text{nzrem}[A/B] = \text{remainder}[A/B]$ if the remainder is non-zero; otherwise $\text{nzrem}[A/B] = B$. As an example, consider the case of the last line in eqn. 14. Here, $n=2$, $p=4$ and $N=2$. Thus, applying eqn.20, we get: $\beta=2$, $\alpha=1$, $\sigma=2$, $\varepsilon=2$, in agreement with the last line of eqn. 14. We should note that there are other ways to determine these coefficients as well, using the *greatest integer* function, for example.

Once (α, β) and (ε, σ) have been obtained, set $\tilde{\rho}_{\varepsilon\sigma}$ to be 1 while setting the other elements to 0, evaluate the Q matrix using eqn. 7, and then pick out $Q_{\alpha\beta}$ and assign it to M_{np} . Then repeat this procedure of evaluating the Q matrix every time with different element of the $\tilde{\rho}$ matrix set to 1 sequentially, until all elements of the M matrix have been calculated.

The steps for finding S and W, as defined in eqn. 18 for the case of a two level system, are rather simple. The last column of the M matrix barring the very last element is the S matrix. In order to determine the elements of W, find first the M' matrix, which is obtained from M by eliminating the last row and the last column, as illustrated in eqn. 17a for a two level system. Define W_i and M'_i as the i -th column of the W and the M' matrix. Then, update a selected set of W_i , using an index k running from 1 to (N-1), as follows:

$$W_{(k-1)N+k} = M'_{(k-1)N+k} - S \quad (21)$$

To illustrate this rule, consider, for example, the case where $N=3$. In this case, $W_1=M_1-S$ (for $k=1$) and $W_5=M_5-S$ (for $k=2$), and the other six columns remain the same. With S and W thus determined, eqn. 20 is used to find the steady-state solution vector: B. A particular element of the density matrix, $\tilde{\rho}_{jk}$ (excluding $\tilde{\rho}_{NN}$), corresponds to the $((j-1)*N+k)$ -th element of the B vector. The population in the N-th level, $\tilde{\rho}_{NN}$ is simply obtained from the knowledge of the steady- state populations in all other levels and the constraint $\sum_{i=1}^N \tilde{\rho}_{ii} = 1$. Explicitly, we can write:

$$\tilde{\rho}_{NN} = 1 - \sum_{j=1}^{(N-1)} B((j-1)N + j) \quad (22)$$

where we have used the notation that $B(k)$ represents the k -th element of the B vector.

A Matlab code for an N-level system, applied to the case of two-levels, is shown in Appendix A. The code is valid for a general system, only N (number of levels in the system), and the effective, complex Hamiltonian (eqn.6) and the source terms (eqn. 8) need to be changed. *The rest of the program does not have to be changed.* Of course, the plotting commands would have to be defined by the user based on the information being sought. As an example, the population of the excited state as a function of the detuning, δ , produced by this code, is plotted in figure 2.

b. A Three Level System

The two-level problem discussed above is somewhat trivial, and may mask the generality of the algorithm. Therefore, we include here the specific steps for a three-level Λ system [6-11], shown in figure 3, in order to elucidate how the algorithm is completely scalable to an arbitrary number of energy levels involved. In this case, the Hamiltonian under electric dipole and rotating wave approximations is given by

$$\mathcal{H} = \hbar \begin{pmatrix} \omega_1 & 0 & \frac{\Omega_a}{2} e^{i\omega_a t} \\ 0 & \omega_2 & \frac{\Omega_b}{2} e^{i\omega_b t} \\ \frac{\Omega_a}{2} e^{i\omega_a t} & \frac{\Omega_b}{2} e^{i\omega_b t} & \omega_3 \end{pmatrix} \quad (23)$$

where $\hbar\omega_1$, $\hbar\omega_2$, and $\hbar\omega_3$ are the energies of the three levels, and ω_a and ω_b are the frequencies of the laser fields.

After applying the interaction picture transformation using the following matrix

$$R = \begin{bmatrix} e^{i\theta t} & 0 & 0 \\ 0 & e^{i\beta t} & 0 \\ 0 & 0 & e^{i\epsilon t} \end{bmatrix} \quad (24)$$

where $\theta = \omega_1 - \frac{\Delta}{2}$, $\beta = \omega_2 + \frac{\Delta}{2}$, $\Delta = \delta_a - \delta_b$, $\delta = (\delta_a + \delta_b)/2$, $\delta_a = \omega_a - (\omega_3 - \omega_1)$,

$\delta_b = \omega_b - (\omega_3 - \omega_2)$ the Hamiltonian can be expressed as

$$\tilde{\mathcal{H}} = \frac{\hbar}{2} \begin{pmatrix} \Delta & 0 & \Omega_a \\ 0 & -\Delta & \Omega_b \\ \Omega_a & \Omega_b & -2\delta \end{pmatrix}. \quad (25)$$

The transformed state vector for each atom can be written as

$$|\tilde{\psi}\rangle = R|\psi\rangle = \begin{bmatrix} \tilde{C}_1(t) \\ \tilde{C}_2(t) \\ \tilde{C}_3(t) \end{bmatrix} \quad (26)$$

The time independent Hamiltonian \tilde{H} of equation 25 can be written down by inspection, following the discussion presented earlier for the two-level system. First, we observe that the energy difference between $|1\rangle$ and $|3\rangle$ ($\tilde{H}_{11} - \tilde{H}_{33}$) is $\hbar\delta_a$, and the energy difference between $|2\rangle$ and $|3\rangle$ ($\tilde{H}_{22} - \tilde{H}_{33}$) is $\hbar\delta_b$. Next, we make a judicious but arbitrary choice that $\tilde{H}_{11} = \frac{\hbar}{2}\Delta$. We then get that $\tilde{H}_{33} = -\hbar\delta$, which in turn implies that $\tilde{H}_{22} = -\frac{\hbar}{2}\Delta$.

The off diagonal terms are, of course, obvious, with non-zero elements for transitions excited by fields. This approach is generic, and can be used to find the time independent

Hamiltonian by inspection for an arbitrary number of levels. We should note that a complication exists when closed-loop excitations are present. In that case, it is wiser to work out the Hamiltonian explicitly using the transformation matrix approach outlined here. We now add the decay term to get the complex Hamiltonian

$$\tilde{\mathcal{H}}' = \frac{\hbar}{2} \begin{pmatrix} \Delta & 0 & \Omega_a \\ 0 & -\Delta & \Omega_b \\ \Omega_a & \Omega_b & -i\Gamma - 2\delta \end{pmatrix} \quad (27)$$

We assume that the population of the excited state decays at the same rate (from $|3\rangle$ to $|1\rangle$ and from $|3\rangle$ to $|2\rangle$). Now we construct the M matrix for the three-level system which satisfies the following equation under the steady-state condition:

$$\begin{bmatrix} M_{11} & M_{12} & M_{13} & M_{14} & M_{15} & M_{16} & M_{17} & M_{18} & M_{19} \\ M_{21} & M_{22} & M_{23} & M_{24} & M_{25} & M_{26} & M_{27} & M_{28} & M_{29} \\ M_{31} & M_{32} & M_{33} & M_{34} & M_{35} & M_{36} & M_{37} & M_{38} & M_{39} \\ M_{41} & M_{42} & M_{43} & M_{44} & M_{45} & M_{46} & M_{47} & M_{48} & M_{49} \\ M_{51} & M_{52} & M_{53} & M_{54} & M_{55} & M_{56} & M_{57} & M_{58} & M_{59} \\ M_{61} & M_{62} & M_{63} & M_{64} & M_{65} & M_{66} & M_{67} & M_{68} & M_{69} \\ M_{71} & M_{72} & M_{73} & M_{74} & M_{75} & M_{76} & M_{77} & M_{78} & M_{79} \\ M_{81} & M_{82} & M_{83} & M_{84} & M_{85} & M_{86} & M_{87} & M_{88} & M_{89} \\ M_{91} & M_{92} & M_{93} & M_{94} & M_{95} & M_{96} & M_{97} & M_{98} & M_{99} \end{bmatrix} \begin{bmatrix} \tilde{\rho}_{11} \\ \tilde{\rho}_{12} \\ \tilde{\rho}_{13} \\ \tilde{\rho}_{21} \\ \tilde{\rho}_{22} \\ \tilde{\rho}_{23} \\ \tilde{\rho}_{31} \\ \tilde{\rho}_{32} \\ \tilde{\rho}_{33} \end{bmatrix} = 0 \quad (28)$$

The elements of the M matrix can be found explicitly by following the same steps as shown in equation (7) through (13) for the two-level system. Alternatively, these can be found by using the algorithmic approach outlined in equation (20), and implemented by a computer code. The M-matrix can be obtained in $O(N^2)$ steps as opposed $O(N^4)$ that

would be needed using the method prescribed thus far, but it is non-intuitive and masks the understanding of the algorithm. We have outlined the faster method in the appendix.

Substituting $\tilde{\rho}_{11} + \tilde{\rho}_{22} + \tilde{\rho}_{33} = 1$ into eqn. 28, we get

$$\begin{bmatrix} M_{11} & M_{12} & M_{13} & M_{14} & M_{15} & M_{16} & M_{17} & M_{18} \\ M_{21} & M_{22} & M_{23} & M_{24} & M_{25} & M_{26} & M_{27} & M_{28} \\ M_{31} & M_{32} & M_{33} & M_{34} & M_{35} & M_{36} & M_{37} & M_{38} \\ M_{41} & M_{42} & M_{43} & M_{44} & M_{45} & M_{46} & M_{47} & M_{48} \\ M_{51} & M_{52} & M_{53} & M_{54} & M_{55} & M_{56} & M_{57} & M_{58} \\ M_{61} & M_{62} & M_{63} & M_{64} & M_{65} & M_{66} & M_{67} & M_{68} \\ M_{71} & M_{72} & M_{73} & M_{74} & M_{75} & M_{76} & M_{77} & M_{78} \\ M_{81} & M_{82} & M_{83} & M_{84} & M_{85} & M_{86} & M_{87} & M_{88} \end{bmatrix} \begin{bmatrix} \tilde{\rho}_{11} \\ \tilde{\rho}_{12} \\ \tilde{\rho}_{13} \\ \tilde{\rho}_{21} \\ \tilde{\rho}_{22} \\ \tilde{\rho}_{23} \\ \tilde{\rho}_{31} \\ \tilde{\rho}_{32} \end{bmatrix} = \begin{bmatrix} M_{19} \\ M_{29} \\ M_{39} \\ M_{49} \\ M_{59} \\ M_{69} \\ M_{79} \\ M_{89} \end{bmatrix} \tilde{\rho}_{11} + \begin{bmatrix} M_{19} \\ M_{29} \\ M_{39} \\ M_{49} \\ M_{59} \\ M_{69} \\ M_{79} \\ M_{89} \end{bmatrix} \tilde{\rho}_{22} - \begin{bmatrix} M_{19} \\ M_{29} \\ M_{39} \\ M_{49} \\ M_{59} \\ M_{69} \\ M_{79} \\ M_{89} \end{bmatrix} \tilde{\rho}_{33} \quad (29.a)$$

Or

$$\begin{bmatrix} (M_{11} - M_{19}) & M_{12} & M_{13} & M_{14} & (M_{15} - M_{19}) & M_{16} & M_{17} & M_{18} \\ (M_{21} - M_{29}) & M_{22} & M_{23} & M_{24} & (M_{25} - M_{29}) & M_{26} & M_{27} & M_{28} \\ (M_{31} - M_{39}) & M_{32} & M_{33} & M_{34} & (M_{35} - M_{39}) & M_{36} & M_{37} & M_{38} \\ (M_{41} - M_{49}) & M_{42} & M_{43} & M_{44} & (M_{45} - M_{49}) & M_{46} & M_{47} & M_{48} \\ (M_{51} - M_{59}) & M_{52} & M_{53} & M_{54} & (M_{55} - M_{59}) & M_{56} & M_{57} & M_{58} \\ (M_{61} - M_{69}) & M_{62} & M_{63} & M_{64} & (M_{65} - M_{69}) & M_{66} & M_{67} & M_{68} \\ (M_{71} - M_{79}) & M_{72} & M_{73} & M_{74} & (M_{75} - M_{79}) & M_{76} & M_{77} & M_{78} \\ (M_{81} - M_{89}) & M_{82} & M_{83} & M_{84} & (M_{85} - M_{89}) & M_{86} & M_{87} & M_{88} \end{bmatrix} \begin{bmatrix} \tilde{\rho}_{11} \\ \tilde{\rho}_{12} \\ \tilde{\rho}_{13} \\ \tilde{\rho}_{21} \\ \tilde{\rho}_{22} \\ \tilde{\rho}_{23} \\ \tilde{\rho}_{31} \\ \tilde{\rho}_{32} \end{bmatrix} = - \begin{bmatrix} M_{19} \\ M_{29} \\ M_{39} \\ M_{49} \\ M_{59} \\ M_{69} \\ M_{79} \\ M_{89} \end{bmatrix} \tilde{\rho}_{33} \quad (29.b)$$

To simplify the above expression, we define the following objects as before

$$B = \begin{bmatrix} \tilde{\rho}_{11} \\ \tilde{\rho}_{12} \\ \tilde{\rho}_{13} \\ \tilde{\rho}_{21} \\ \tilde{\rho}_{22} \\ \tilde{\rho}_{23} \\ \tilde{\rho}_{31} \\ \tilde{\rho}_{32} \end{bmatrix} \quad S = \begin{bmatrix} M_{19} \\ M_{29} \\ M_{39} \\ M_{49} \\ M_{59} \\ M_{69} \\ M_{79} \\ M_{89} \end{bmatrix} \quad W = \begin{bmatrix} (M_{11} - M_{19}) & M_{12} & M_{13} & M_{14} & (M_{15} - M_{19}) & M_{16} & M_{17} & M_{18} \\ (M_{21} - M_{29}) & M_{22} & M_{23} & M_{24} & (M_{25} - M_{29}) & M_{26} & M_{27} & M_{28} \\ (M_{31} - M_{39}) & M_{32} & M_{33} & M_{34} & (M_{35} - M_{39}) & M_{36} & M_{37} & M_{38} \\ (M_{41} - M_{49}) & M_{42} & M_{43} & M_{44} & (M_{45} - M_{49}) & M_{46} & M_{47} & M_{48} \\ (M_{51} - M_{59}) & M_{52} & M_{53} & M_{54} & (M_{55} - M_{59}) & M_{56} & M_{57} & M_{58} \\ (M_{61} - M_{69}) & M_{62} & M_{63} & M_{64} & (M_{65} - M_{69}) & M_{66} & M_{67} & M_{68} \\ (M_{71} - M_{79}) & M_{72} & M_{73} & M_{74} & (M_{75} - M_{79}) & M_{76} & M_{77} & M_{78} \\ (M_{81} - M_{89}) & M_{82} & M_{83} & M_{84} & (M_{85} - M_{89}) & M_{86} & M_{87} & M_{88} \end{bmatrix}$$

Substituting them into eqn. 29.b, we get

$$WB = -S \quad \text{or} \quad B = -W^{-1}S \quad (30)$$

The Matlab program shown in Appendix B implements our algorithm for the three level system. Note that *this program is essentially the same as the program for the two-level case* with the following modifications: we have (a) defined additional parameters relevant to this system, (b) entered proper elements in the Hamiltonian, and (c) added appropriate source terms for the populations. As an example, we have shown in figure 4 a plot of the population of the excited state, produced using this code, displaying the well-known coherent population trapping dip.

c. Applying the code to a system with an arbitrary number of energy levels

There are many examples in atomic and molecular physics where it is necessary to include a large number of energy levels. One example is an atomic clock employing coherent population trapping [1]. The basic process employs only three Zeeman sublevels. However, the other Zeeman sublevels have to be taken into account in order to describe the behavior of the clock accurately. Using alkali atoms for other applications such as

atomic interferometry, magnetometry and Zeno-effect based switching also requires taking into account a large number of Zeeman sublevels []. Another example is the cooling of molecules using lasers. In this case, many rotational and vibrational levels have to be considered []. The code presented here can be applied readily to these problems, with the following modifications: (a) define additional parameters to characterize the problem, (b) develop the time independent Hamiltonian (possibly by inspection using the technique described earlier, if no closed-loop excitation is present), (c) add proper decay terms to the Hamiltonian, (d) add appropriate source terms for the populations & transverse decay terms, and (e) add plotting instructions for components of interest from the solution vector. Of course, if numerical techniques are to be employed for finding time-dependent solutions, the code can be truncated after the M matrix is determined, followed by application of eqn. 13 along with a proper choice of initial conditions.

d. Applying the code to a specific system with fifteen energy levels: an optically controlled waveplate

As an explicit example of a system involving a non-trivial number of energy levels and optical transitions, we consider here a process where a ladder transition in ^{87}Rb is used to affect the polarization of a probe beam (upper leg) by varying parameters for the control beam (lower leg). The excitation process is illustrated schematically in figure 5, for one

particular configuration where the control beam is right circularly polarized, and the probe is linearly polarized. Because of the asymmetry introduced by the control, it is expected that the left circular component of the probe would experience a much larger phase shift, which in turn would induce an effective rotation of the probe polarization. Thus, the system can be viewed as an optically controlled waveplate for the probe. Here, we use the generalized algorithm to compute the response of this system. Of course, the response of the system under various experimental conditions would be quite different. The interactions of the pump ($\sim 795\text{nm}$) and the probe ($\sim 1323\text{nm}$) are modeled as follows. The pump is either left or right circularly polarized, and is tuned between the $5S_{1/2}, F=1 \rightarrow 5P_{1/2}, F'=1$ and the $5S_{1/2}, F=1 \rightarrow 5P_{1/2}, F'=2$ transitions, with a detuning of δ_p , as illustrated in figure 5. The probe, linearly polarized, is tuned to the $5P_{1/2}, F'=1$ to $6S_{1/2}, F''=1$ transition, with a detuning of δ_s . Due to Doppler broadening, it is important to consider the interaction of the $5P_{1/2}, F'=2$ level with both the pump and probe optical fields. For example, $\delta_p = 814.5\text{MHz}$ corresponds to the situation where the pump is resonant with the $5S_{1/2}, F=1 \rightarrow 5P_{1/2}, F'=2$ transition and $\delta_s = -814.5\text{MHz}$ corresponds to the situation where the probe is resonant with the $5P_{1/2}, F'=2$ to $6S_{1/2}, F''=1$ transition. In our model, we ignore the coherent coupling between $5S_{1/2}, F=2$ and the $5P_{1/2}$ manifold, because of the large frequency difference between $5S_{1/2}, F=1$ and $5S_{1/2}, F=2$ ($\sim 6.8\text{GHz}$ for ^{87}Rb). However, we take into account the decay of atoms from the $5P_{1/2}$ manifold to the $5S_{1/2}, F=2$ state. Furthermore, we account for collisional relaxation (at a rate Γ_g) between $5S_{1/2}, F=1$ and $5S_{1/2}, F=2$ manifolds, in order to model the behavior of atoms in a vapor

cell. Finally, we also take into account the decay of atoms from $6S_{1/2}$, $F''=1$ to the $5S_{1/2}$ manifold via the $5P_{3/2}$ manifold in an approximate manner.

The Rabi frequency of each transition is proportional to the corresponding dipole moment matrix elements. In Fig. 5, all the Rabi frequencies are expressed as a multiple of the Rabi frequency corresponding to the weakest transition. For example, the dipole matrix elements of σ^+ transitions for the $5S_{1/2}$ - $5P_{1/2}$ excitation are tabulated in Table 1. Thus, if we set the coupling between $|1\rangle$ and $|5\rangle$ to be $\tilde{H}_{1,5} = -\frac{\Omega_{P+}}{2}$, then the other coupling terms for the lower leg are as follows:

$$\tilde{H}_{1,9} = -\frac{\Omega_{P+}}{2}, \tilde{H}_{2,6} = -\frac{\Omega_{P+}}{2}, \tilde{H}_{2,10} = -\frac{\sqrt{3}\Omega_{P+}}{2}, \tilde{H}_{3,11} = -\frac{\sqrt{6}\Omega_{P+}}{2}.$$

The decay rates between any two Zeeman sub-levels are assumed to be proportional to the squares of the dipole moment matrix elements such that the sum of all the decay rates equals the net decay rate from that level. We assume all the Zeeman sub-levels in the $5P_{1/2}$ and $6S_{1/2}$ manifold decay at the same rate, Γ_a and Γ_b respectively. To illustrate how the decay terms are determined, consider, for example, state $|5\rangle$, which denotes the Zeeman sublevel $5P_{1/2}$, $F'=1$, $m_F=0$. The dipole matrix elements for all allowed transitions from this state to the various sublevels within the $5S_{1/2}$ manifold are shown in Fig. 6. With the decay rate from $|5\rangle$ to the $5S_{1/2}$ manifold being Γ_a , the decay rate from $|5\rangle$ to $|1\rangle$ (or $|2\rangle$) is $\Gamma_a/12$. The decay from $|5\rangle$ to $|15\rangle$ ($5S_{1/2}$, $F=2$) is calculated by adding the squares of the matrix elements for all transitions between $|5\rangle$ and the Zeeman levels of $|15\rangle$, and this turns out to be $5\Gamma_a/6$.

We have also taken into account the sourcing of atoms into the ground states from the $6S_{1/2}$ state via the $5P_{3/2}$ state. These additional source terms are modeled using an “effective decay rate” (Γ_{bi}) directly from the Zeeman sub-levels in the $6S_{1/2}$, $F''=1$ level to the $5S_{1/2}$ manifold. It is then assumed that all the Zeeman sub-levels at the $6S_{1/2}$, $F''=1$ level decays equally to the Zeeman sub-levels of $F=1$ and $F=2$ levels at this rate. In Fig 7, the branching ratios between the various hyperfine levels and the effective decay rates from the $6S_{1/2}$, $F''=1$ level to the $5S_{1/2}$ manifold are shown. For our initial computations, we used a rough estimate for Γ_{bi} . A more detailed calculation, taking into account the various branching ratios into and from all the hyperfine levels of the $5P_{3/2}$ state can be used to determine Γ_{bi} . However, we found that the results did not change significantly when Γ_{bi} was changed slightly and hence using an approximate value is justified.

The goal of the simulation of the process illustrated in figure 5 is to determine how the state of a linearly polarized probe beam (@1323nm) is affected by its passage through a vapor cell of length L and density n , in the presence of a circularly polarized pump beam (@795nm). Thus, before presenting the details of the atom laser interaction, we specify the terminology relevant for characterizing the probe beam, using the Jones vector formulation. We consider the direction of propagation as the z -axis, and the input probe to be linearly polarized in the x direction. Thus, the input probe can be described as:

$$\vec{J}_{\text{probe,input}} = \begin{bmatrix} 1 \\ 0 \end{bmatrix} = \frac{1}{2} \begin{bmatrix} 1 \\ i \end{bmatrix} + \frac{1}{2} \begin{bmatrix} 1 \\ -i \end{bmatrix} \quad (31)$$

The second part of eqn. (31) indicates that the linear polarization has been decomposed into a right circular polarization and a left circular polarization. The effect of propagation through the cell can now be modeled by expressing the output Jones vector as follows:

$$\vec{J}_{\text{probe,output}} = \frac{1}{2} \begin{bmatrix} 1 \\ i \end{bmatrix} e^{-\alpha_+ + j\phi_+} + \frac{1}{2} \begin{bmatrix} 1 \\ -i \end{bmatrix} e^{-\alpha_- + j\phi_-} \quad (32)$$

where α_+ (α_-) and ϕ_+ (ϕ_-) are the attenuation and phase shift experienced by the right (left) circular component, respectively.

In order to make the system behave as an ideal half waveplate, for example, the phase difference between the right and left polarization components ($|\phi_+ - \phi_-|$) should be equal to π , and the attenuation for each component should equal zero ($\alpha_+ = \alpha_- = 0$). In that case, the output expression can be simplified as:

$$\vec{J}_{\text{probe,output}} = \frac{1}{2} \begin{bmatrix} 1 \\ i \end{bmatrix} e^{j\phi_+} + \frac{1}{2} \begin{bmatrix} 1 \\ -i \end{bmatrix} e^{j\phi_-} = \frac{1}{2} e^{j\phi_-} \left(\begin{bmatrix} 1 \\ i \end{bmatrix} e^{j\pi} + \begin{bmatrix} 1 \\ -i \end{bmatrix} \right) = e^{j(\phi_- - \frac{\pi}{2})} \begin{bmatrix} 0 \\ 1 \end{bmatrix} \quad (33)$$

which is polarized linearly in the y-direction. In practice, the attenuation coefficients are non-vanishing. However, if they are equal to each other (i.e. $\alpha_+ = \alpha_-$), then they simply reduce the amplitude of the signal, without affecting the sense of polarization. Of course, the phase difference ($\phi_+ = \phi_-$) can have a wide range of values, corresponding to different output polarization states. In what follows, we solve the density matrix equation

of motion for the 15-level system shown in figure 5, in order to determine the four quantities of interest: Φ_+ , Φ_- , α_+ , α_- .

The time-independent Hamiltonian after moving to a rotating basis and the RWA can be written down using the method we described in Section 2 & 3. Given the large number of levels, we use below a compact notation, rather than a matrix, to express the Hamiltonian. Specifically, \tilde{H} is given by (setting $\hbar=1$):

$$\tilde{H}_{1,1} = -i\frac{\Gamma g}{2}, \tilde{H}_{1,5} = -\frac{\Omega_P}{2}, \tilde{H}_{1,9} = -\frac{\Omega_P}{2};$$

$$\tilde{H}_{2,2} = -i\frac{\Gamma g}{2}, \tilde{H}_{2,6} = -\frac{\Omega_P}{2}, \tilde{H}_{2,10} = -\frac{\sqrt{3}\Omega_P}{2};$$

$$\tilde{H}_{3,3} = -i\frac{\Gamma g}{2}, \tilde{H}_{3,11} = -\frac{\sqrt{6}\Omega_P}{2};$$

$$\tilde{H}_{4,4} = -\delta_P - i\frac{\Gamma a}{2}, \tilde{H}_{4,13} = -\frac{\Omega_S}{2};$$

$$\tilde{H}_{5,1} = \tilde{H}_{1,5}^*, \tilde{H}_{5,5} = -\delta_P - i\frac{\Gamma a}{2}, \tilde{H}_{5,12} = \frac{\Omega_S}{2}, \tilde{H}_{5,14} = -\frac{\Omega_S}{2};$$

$$\tilde{H}_{6,2} = \tilde{H}_{2,6}^*, \tilde{H}_{6,6} = -\delta_P - i\frac{\Gamma a}{2}, \tilde{H}_{6,13} = \frac{\Omega_S}{2};$$

$$\tilde{H}_{7,7} = \Delta - \delta_P - i\frac{\Gamma a}{2}, \tilde{H}_{7,12} = \frac{\sqrt{6}\Omega_S}{2};$$

$$\tilde{H}_{8,8} = \Delta - \delta_P - i\frac{\Gamma a}{2}, \tilde{H}_{8,13} = \frac{\sqrt{3}\Omega_S}{2};$$

$$\tilde{H}_{9,1} = \tilde{H}_{1,9}^*, \tilde{H}_{9,9} = \Delta - \delta_P - i\frac{\Gamma a}{2}, \tilde{H}_{9,12} = \frac{\Omega_S}{2}, \tilde{H}_{9,14} = \frac{\Omega_S}{2};$$

$$\tilde{H}_{10,2} = \tilde{H}_{2,10}^*, \tilde{H}_{10,10} = \Delta - \delta_P - i\frac{\Gamma a}{2}, \tilde{H}_{10,13} = \frac{\sqrt{3}\Omega_S}{2};$$

$$\tilde{H}_{11,3} = \tilde{H}_{3,11}^*, \tilde{H}_{11,11} = \Delta - \delta_P - i\frac{\Gamma a}{2}, \tilde{H}_{11,14} = \frac{\sqrt{6}\Omega_S}{2};$$

$$\tilde{H}_{12,5} = \tilde{H}_{5,12}^*, \tilde{H}_{12,7} = \tilde{H}_{7,12}^*, \tilde{H}_{12,9} = \tilde{H}_{9,12}^*, \tilde{H}_{12,12} = -\delta_S - \delta_P - i\frac{\Gamma b}{2};$$

$$\tilde{H}_{13,4} = \tilde{H}_{4,13}^*, \tilde{H}_{13,6} = \tilde{H}_{6,13}^*, \tilde{H}_{13,8} = \tilde{H}_{8,13}^*, \tilde{H}_{13,10} = \tilde{H}_{10,13}^*, \tilde{H}_{13,13} = -\delta_s - \delta_p - i\frac{\Gamma_b}{2};$$

$$\tilde{H}_{14,5} = \tilde{H}_{5,14}^*, \tilde{H}_{14,9} = \tilde{H}_{9,14}^*, \tilde{H}_{14,11} = \tilde{H}_{11,14}^*, \tilde{H}_{14,14} = -\delta_s - \delta_p - i\frac{\Gamma_b}{2};$$

$$\tilde{H}_{15,15} = -i\frac{\Gamma_g}{2}.$$

All the other terms of \tilde{H} are equal to zero. We then add the population source terms to the Hamiltonian. We assume the decay rates from $F''=1$ to $5P_{1/2}$ (Γ_{bd}) are equal to the effective decay rate from $F''=1$ to $5S_{1/2}$ (Γ_{bi}). Thus, $\Gamma_{bd} = \alpha\Gamma_b$, $\Gamma_{bi} = (1 - \alpha)\Gamma_b$ where $\alpha = 0.5$

$$\begin{aligned} \frac{d\rho_{11}}{dt} &= (\rho_{44} + \rho_{55} + \rho_{99})\frac{\Gamma_a}{12} + \rho_{77}\frac{\Gamma_a}{2} + \rho_{88}\frac{\Gamma_a}{4} + (\rho_{12,12} + \rho_{13,13} + \rho_{14,14})\frac{\Gamma_{bi}}{18} \\ &\quad + \rho_{15,15}\frac{\Gamma_g}{3} \end{aligned}$$

$$\begin{aligned} \frac{d\rho_{22}}{dt} &= (\rho_{44} + \rho_{66})\frac{\Gamma_a}{12} + \rho_{88}\frac{\Gamma_a}{4} + \rho_{99}\frac{\Gamma_a}{3} + \rho_{10,10}\frac{\Gamma_a}{4} + (\rho_{12,12} + \rho_{13,13} + \rho_{14,14})\frac{\Gamma_{bi}}{18} \\ &\quad + \rho_{15,15}\frac{\Gamma_g}{3} \end{aligned}$$

$$\begin{aligned} \frac{d\rho_{33}}{dt} &= (\rho_{55} + \rho_{66} + \rho_{99})\frac{\Gamma_a}{12} + \rho_{10,10}\frac{\Gamma_a}{4} + \rho_{11,11}\frac{\Gamma_a}{2} + (\rho_{12,12} + \rho_{13,13} + \rho_{14,14})\frac{\Gamma_{bi}}{18} \\ &\quad + \rho_{15,15}\frac{\Gamma_g}{3} \end{aligned}$$

$$\frac{d\rho_{44}}{dt} = \rho_{12,12}\frac{\Gamma_{bd}}{12} + \rho_{13,13}\frac{\Gamma_{bd}}{12}$$

$$\frac{d\rho_{55}}{dt} = \rho_{12,12} \frac{\Gamma_{bd}}{12} + \rho_{14,14} \frac{\Gamma_{bd}}{12}$$

$$\frac{d\rho_{66}}{dt} = \rho_{13,13} \frac{\Gamma_{bd}}{12} + \rho_{14,14} \frac{\Gamma_{bd}}{12}$$

$$\frac{d\rho_{77}}{dt} = \rho_{12,12} \frac{\Gamma_{bd}}{2}$$

$$\frac{d\rho_{88}}{dt} = \rho_{12,12} \frac{\Gamma_{bd}}{4} + \rho_{13,13} \frac{\Gamma_{bd}}{4}$$

$$\frac{d\rho_{99}}{dt} = \rho_{12,12} \frac{\Gamma_{bd}}{12} + \rho_{13,13} \frac{\Gamma_{bd}}{3} + \rho_{14,14} \frac{\Gamma_{bd}}{12}$$

$$\frac{d\rho_{10,10}}{dt} = \rho_{13,13} \frac{\Gamma_{bd}}{4} + \rho_{14,14} \frac{\Gamma_{bd}}{4}$$

$$\frac{d\rho_{11,11}}{dt} = \rho_{14,14} \frac{\Gamma_{bd}}{2}$$

$$\frac{d\rho_{15,15}}{dt} = (\rho_{1,1} + \rho_{2,2} + \rho_{3,3})\Gamma_{gg} + (\rho_{44} + \rho_{55} + \rho_{66}) \frac{5\Gamma_a}{6}$$

$$+ (\rho_{77} + \rho_{88} + \rho_{99} + \rho_{10,10} + \rho_{11,11}) \frac{\Gamma_a}{2} + (\rho_{12,12} + \rho_{13,13} + \rho_{14,14}) \frac{5\Gamma_{bi}}{6}$$

The attenuation and the additional phase shift introduced by the Rb medium (as compared to free space propagation) of the signal beam can be expressed as:

Phase:

$$\phi_+ = kL \frac{\beta_+}{2} \text{Re}(a_{13,4}\rho_{13,4} + a_{14,5}\rho_{14,5} + a_{12,7}\rho_{12,7} + a_{13,8}\rho_{13,8} + a_{14,9}\rho_{14,9})$$

$$\phi_- = kL \frac{\beta_-}{2} \text{Re}(a_{12,5}\rho_{12,5} + a_{13,6}\rho_{13,6} + a_{12,9}\rho_{12,9} + a_{13,10}\rho_{13,10} + a_{14,11}\rho_{14,11})$$

Attenuation:

$$\alpha_+ = e^{-kL\beta_+ \text{Im}(a_{13,4}\rho_{13,4} + a_{14,5}\rho_{14,5} + a_{12,7}\rho_{12,7} + a_{13,8}\rho_{13,8} + a_{14,9}\rho_{14,9})/2}$$

$$\alpha_- = e^{-kL\beta_- \text{Im}(a_{12,5}\rho_{12,5} + a_{13,6}\rho_{13,6} + a_{12,9}\rho_{12,9} + a_{13,10}\rho_{13,10} + a_{14,11}\rho_{14,11})/2}$$

And

$$\beta_{\pm} = b_{min}^2 \frac{3n_{atom}\Gamma\lambda^3}{4\pi^2\Omega_{min}}$$

where, k is the wavevector of signal beam, which is at 1323nm, L is the length of the cell, which is set to be 15cm, n_{atom} is the density of Rb atoms, which is set to be $10^{16}/m^3$, Ω_{min} is the Rabi frequency for the weakest probe transition (for example, the $|14\rangle - |9\rangle$ transition in our model) and the various a_{ij} 's are the ratios of the Rabi frequency (Ω_{ij}) of the $|i\rangle - |j\rangle$ transition to Ω_{min} . For example, $a_{12,7} = \Omega_{12,7}/\Omega_{14,9} = \sqrt{6}$. b_{min}^2 is the fraction of the atoms (<1) that decay along the transition corresponding to Ω_{min} , among all allowed decay channels from the decaying level. In our model, the amplitudes for all possible transitions from $|14\rangle$ are in the ratio $1:1:1:\sqrt{3}:\sqrt{6}$ and hence the fraction of atoms that decay along the different channels are in the ratio $1:1:1:3:6$. Thus, $b_{min}^2 = 1/(1 + 1 + 1 + 3 + 6) = 1/12$.

Setting the pump frequency at a certain value ($\delta_p = \Delta$, which corresponds to the situation when the pump is resonant with the $F=1$ to $F'=2$ transition) and scanning the probe detuning (δ_s), we can plot the various quantities of interest (Φ_+ , Φ_- , α_+ , α_-) as a function of δ_s , as shown in Fig. 8. The relevant parameters used for this particular simulation are as follows. The decay rates Γ_a , Γ_b and Γ_g are $2\pi*5.75 \text{ sec}^{-1}$, $2\pi*3.45 \text{ sec}^{-1}$ and $2\pi*0.1 \text{ sec}^{-1}$ respectively. We perform our calculations by setting Γ_a to unity and rescaling all parameters in units of Γ_a . The separation Δ , between $F'=1$ and $F'=2$ is $2\pi*814.5 \text{ sec}^{-1}$ ($= 141.4\Gamma_a$) and the probe detuning (δ_s) ranges from $-200\Gamma_a$ to $200\Gamma_a$. The Rabi frequencies have been chosen to be $\Omega_p = 5\Gamma_a$, and $\Omega_s = 0.1\Gamma_a$. Fig. 8(a) and 8(b) show the additional phase shifts produced by the Rb medium for the right and left circular polarization parts of the signal beam and Fig. 8(c) shows the difference between them. Fig. 8(d)-8(f) show the corresponding figures for attenuation. For example, at $\delta_s=200$, we have a differential attenuation of ~ 0 and a differential phase shift of about 30° . Since the main purpose of this paper is to illustrate the application of the algorithm for obtaining the solution to the density matrix equations for a large quantum system, we refrain from exploring the parameter space in detail.

e. Conclusion

We have presented a novel algorithm for efficiently finding the solution to the density matrix equations for an atomic system with arbitrary number of energy levels. For this

purpose, the Liouville equation that describes the time evolution of the density matrix is formulated as a matrix-vector equation. We presented an algorithm that allows us to find the elements of the evolution matrix with ease for systems with arbitrarily large value of N . As examples, we then used the algorithm to find steady-state solutions for atomic systems consisting of two- and three- levels. We also described a comprehensive model (consisting of 15 levels) for an optically controlled waveplate using the $5S_{1/2}$ - $5P_{1/2}$ - $6S_{1/2}$ cascade system. Finally, we used the algorithm to obtain the steady state solution for the 15-level system. The algorithm and the Matlab codes presented here should prove very useful for the atomic and molecular physics community.

Appendix A: Matlab Program for Solving the Two Level Problem

```

omeg=5;      % express rabi freq, normalized to gamma
N=2;        % number of energy levels
R=401       % number of points to plot
            % initialize and set dimensions for all matrices
delta=zeros(1,R); %detuning array
M=zeros(N^2,N^2); %M-matrix
rho=zeros(N,N);  %dens mat
Ham=zeros(N,N);  %Hamiltonian with decay
Q=zeros(N,N);    %matrix corresponding to derivative of the density matrix

W=zeros((N^2-1),(N^2-1)); % W-matrix
S=zeros((N^2-1),1);      %S-vector
B=zeros((N^2-1),1);      %B-vector
A=zeros(N^2,R);         %A-vectors, for all detunings

for m=1:R %start the overall-loop
    delta(1,m)=(m-(R+1)/2)/2; %define the detuning, normalized to gamma
    Ham=[0 omeq/2; omeq/2 (delta(1,m)+0.5i)*(-1)]; %elements of Hamiltonian

    for n=1:N^2 %start the outer-loop for finding elements of M;
        for p=1:N^2 %start inner-loop for finding elements of M;

```

```

                %M(n,p) equals Q(alpha,beta) with only rho(epsilon,
                %sigma)=1, and other elements of rho set to zero.

                %determining dummy coefficients alpha and beta
remain=rem(n,N);
if remain==0
    beta=N;
else beta=remain;
end
alpha=(1+(n-beta)/N);

                %determining dummy coefficients epsilon and sigma
remain=rem(p,N);
if remain==0
    sigma=N;
else sigma=remain;
end
epsilon=(1+(p-sigma)/N);

rho=zeros(N,N);          %reset rho to all zeros
rho(epsilon,sigma)=1;    %pick one element to be unity
Q=(Ham*rho-rho*conj(Ham))*(0-1i); %find first part of Q matrix
Q(1,1)=Q(1,1)+rho(2,2); %add pop source term to Q
                        %For an N-level system, add additional
                        %source terms as needed
M(n,p)=Q(alpha,beta);
end %end the inner-loop for finding elements of M
end %end of the outer-loop for finding elements of M

S=M(1:(N^2-1),N^2:N^2); %find S-vector
W=M(1:(N^2-1),1:(N^2-1)); %initialize W-matrix

for d=1:(N-1)
    W(:,((d-1)*N+d))=W(:,((d-1)*N+d))-S; %update W by subtracting
                                        %from selected columns
end

B=(W\S)*(-1); %find B-vector: primary solution

rhonn=1; %initialize pop of N-th state
          %determine pop of N-th state

```

```
for f=1:(N-1)
    rhonn=rhonn-B(((f-1)*N+f), 1);
end
                                %determine the elements of the A vector
A(1:(N^2-1),m)=B;
A(N^2,m)=rhonn;

end                                %end of over-all loop
plot(delta,real(A((N^2-0),:)))
```

Appendix B: Matlab Program for Solving the Three Level Problem

```

oma=1; omb=1; % express omeg rabi freqs, in units of gamma
dels=0;      % common detuning set to zero
N=3;        % number of energy levels
R=401       % number of points to plot
            % initialize and set dimensions for all matrices
del=zeros(1,R); % diff detuning array
M=zeros(N^2,N^2); % M-matrix
rho=zeros(N,N); % density matrix
Ham=zeros(N,N); % Hamiltonian with decay
Q=zeros(N,N); % matrix representing derivative of density matrix
W=zeros((N^2-1),(N^2-1)); % W-matrix
S=zeros((N^2-1),1); % S-vector
B=zeros((N^2-1),1); % B-vector
A=zeros(N^2,R); % A-vectors, for all detunings

for m=1:R %start the overall-loop
del(1,m)=(m-(R+1)/2)/10; %define the detuning
Ham=[del(1,m)/2 0 oma/2; 0 del(1,m)*(-1)/2 omb/2; ...
     oma/2 omb/2 (dels+0.5i)*(-1)];

for n=1:N^2 %start the outer-loop for finding elements of M;
for p=1:N^2 %start inner-loop for finding elements of M;

    %finding alpha and beta
    remain=rem(n,N);
    if remain==0
        beta=N;
    else beta=remain;
    end
    alpha=(1+(n-beta)/N);

    %finding epsilon and sigma
    remain=rem(p,N);
    if remain==0
        sigma=N;
    else sigma=remain;
    end
    epsilon=(1+(p-sigma)/N);

    rho=zeros(N,N); %reset rho to all zeros

```

```

rho(epsilon,sigma)=1;      %pick one element to unity
Q=(Ham*rho-rho*conj(Ham))*(0-1i); %find first part of Q matrix

Q(1,1)=Q(1,1)+rho(3,3)/2;   %add pop source term to Q
Q(2,2)=Q(2,2)+rho(3,3)/2;   %add pop source term to Q
      %Modify as needed for general
      %systems
M(n,p)=Q(alpha,beta);
end      %end the inner-loop for finding elements of M
end      %end of the outer-loop for finding elements of M

S=M(1:(N^2-1),N^2:N^2);   %find S-vector
W=M(1:(N^2-1),1:(N^2-1)); %initialize W-matrix

for d=1:(N-1)
    W(:,((d-1)*N+d))=W(:,((d-1)*N+d))-S; %update W by subtracting
      %from selected columns
end

B=(W\S)*(-1);      %find B-vector: primary solution

rhonn=1;          %initialize pop of N-th state
                  %determine pop of N-th state
for f=1:(N-1)
    rhonn=rhonn-B(((f-1)*N+f), 1);
end
                  %determine elements of A vector

A(1:(N^2-1),m)=B;
A(N^2,m)=rhonn;

end      %end of over-all loop
plot(del,real( A ( (N^2-0),: ) ) )

```

Algorithm Optimization

The crux of the algorithm is to obtain the M matrix in an automated fashion. The most obvious, but rather elaborate ($O(N^4)$ operations) way to perform this task has been illustrated previously. However, several simplifications can be made to the algorithm so that the entire process can be accomplished using $O(N^2)$ operations and also avoid some other redundant operations, thereby increasing the speed by a factor of $\sim N^2$. To do this, we first observe that instead of evaluating the M matrix row-wise as was shown before, it is more beneficial to evaluate it column wise. Each column in the M matrix is simply obtained by successively setting each of the density matrix elements to 1, while setting all others to 0. Thus, the entire 1st column can be obtained by setting $\rho_{11}=1$ and all other $\rho_{ij}=0$, 2nd column with $\rho_{12}=1$ and all other $\rho_{ij}=0$ and so on. In general, by setting $\rho_{\varepsilon\sigma}=1$ and all other density matrix elements to 0, we obtain the $((\varepsilon-1)*N+\sigma)$ th column of the M matrix where each of ε and σ vary from 1 to N .

Furthermore, it is to be noted that the computation $H\rho-\rho H^\dagger$ involve multiplication of extremely sparse matrices, since only one of the elements of the ρ matrix is 1 each time. It is evident that each column of the M matrix will simply be made up of certain columns of the Hamiltonian. Thus, the task is reduced to (a) figuring out the pattern of columns that are picked out from the Hamiltonian and (b) identify the locations in the M -matrix, where they would be filled. To illustrate this clearly, it is convenient to treat the

calculation of the M-matrix as arising from two separate computations: $H\rho$ and ρH^+ .

Let us consider a specific case when $\rho_{\varepsilon\sigma}=1$. The ρH^+ computations would pick the σ^{th} column of the Hamiltonian (with its elements conjugated) to be placed between rows $(\varepsilon-1)*N+1$ and $\varepsilon*N$ of the $((\varepsilon-1)*N+\sigma)^{\text{th}}$ column of the M matrix. The $H\rho$ computations, on other hand, would pick the elements of the ε^{th} column of the Hamiltonian (with the elements picking up an extra negative sign) and populate the following rows of the $((\varepsilon-1)*N+\sigma)^{\text{th}}$ column of the M matrix: σ^{th} row, $(\sigma+N)^{\text{th}}$ row, $(\sigma+2*N)^{\text{th}}$ row and so on until the $(\sigma+N*(N-1))^{\text{th}}$ row. When, this process is repeated for each element of the density matrix, the M-matrix, barring the source terms would have been computed.

Finally, the addition of the source terms can also be simplified by choosing to modify the M-matrix only when one of the diagonal elements of the density matrix is set to 1, i.e $\rho_{\varepsilon\varepsilon}=1$, where $\varepsilon=1$ to N . Furthermore, instead of adding the source terms in-line, as was done previously, we can simply pre-define a “source-matrix” and simply pick off the elements of this matrix that would then be added to the appropriate entries in the M-matrix. For example, one way of defining such a “source matrix” would be to have the coefficients of the $\rho_{\varepsilon\varepsilon}$ in all the source equations (from $d\rho_{11}/dt$ to $d\rho_{NN}/dt$) along the ε^{th} column of the source matrix. Now, all that needs to be done is to simply add the ε^{th} column of the source matrix to the $(\varepsilon-1)*N+ \varepsilon^{\text{th}}$ column of the previously computed M matrix whenever $\rho_{\varepsilon\varepsilon}=1$. As an illustration of these optimization steps, we reproduce

below a modified version of the code for a 3-level system, which should be contrasted with the unoptimized code for the same system presented in Appendix B.

```

oma=1; omb=1; % express omeg rabi freqs, in units of gamma
dels=0; % common detuning set to zero
N=3; % number of energy levels
R=401 % number of points to plot
% initialize and set dimensions for all matrices
del=zeros(1,R); % diff detuning array
M=zeros(N^2,N^2); % M-matrix
rho=zeros(N,N); % density matrix
Ham=zeros(N,N); % Hamiltonian with decay
W=zeros((N^2-1),(N^2-1)); % W-matrix
S=zeros((N^2-1),1); % S-vector
B=zeros((N^2-1),1); % B-vector
A=zeros(N^2,R); % A-vectors, for all detunings
Q_source=[0 0 1/2;
          0 0 1/2;
          0 0 0];

for m=1:R %start the overall-loop
del(1,m)=(m-(R+1)/2)/10; %define the detuning
Ham=[del(1,m)/2 0 oma/2;
     0 del(1,m)*(-1)/2 omb/2; ...
     oma/2 omb/2 (dels+0.5i)*(-1)];

col=0; % index for column of M-matrix that will filled.
index1=1:N;
index2=1:N:N*(N-1)+1;
index3=1:N+1:N^2;
for n=1:N %n keeps track of where in the M matrix the elements of
           Ham have to be entered
for p=1:N %p picks the pth column from the Ham
col=col+1;
M(index1+(n-1)*N,col)=1i*conj(H(:,p));
M(index2+p-1,col)=M(index2+p-1,col)-1i*(H(:,n));
if n==p
M(index3,col)=M(index3,col)+Q_source(:,n);
end
end %end the inner-loop for finding elements of M

```

```

end
S=M(1:(N^2-1),N^2:N^2); %find S-vector
W=M(1:(N^2-1),1:(N^2-1)); %initialize W-matrix

for d=1:(N-1)
    W(:,((d-1)*N+d))=W(:,((d-1)*N+d))-S; %update W by subtracting
                                        %from selected columns
end

B=(W\S)*(-1); %find B-vector: primary solution!

rhonn=1; %initialize pop of N-th state
for f=1:(N-1)
    rhonn=rhonn-B(((f-1)*N+f), 1);
end

A(1:(N^2-1),m)=B;
A(N^2,m)=rhonn;
M=zeros(N^2,N^2);
end %end of over-all loop
plot(del,real( A ( (N^2-0),: ) ) )

```

CHAPTER 8 SUMMARY

We demonstrated all-optical modulation in TNF at ultra-low powers ($\sim 40\text{nW}$). We addressed key issues related to the longevity of the TNF and tried several approaches to prolong its life. In order to implement a modulator in one of the telecom bands we switched to the 5S-5P-6S system. We demonstrated a modulator using this system up to speeds of few MHz, limited by the homogenous linewidth of the intermediate levels. We proposed a novel high-speed modulator in a cascade system using buffer gas induced spin-relaxation and de-phasing, theoretically capable of functioning at few tens of GHz. Under similar conditions, we observed a 100-fold increase in the modulation bandwidth. However, we could not achieve the expected GHz modulation. Further investigation is needed to improve the performance.

We also demonstrated an optically controlled polarizer and waveplate, both of which could operate at speeds of few MHz, thus making high-speed Stokesmetric imaging practical. We obtained an extinction ratio of 2.5 for the polarizer and identified means to improve it by using optical pumping. We investigated the performance under both the co- and counter-propagating geometries. We were able to achieve full control the polarization of one optical field using another, having demonstrated rotation of polarization from horizontal to vertical and also to a circular polarization. Further investigation is needed to optimize the performance of these devices, in terms of the bandwidth, power required etc.

We also developed a novel computational algorithm which could prove extremely useful in performing numerical computations of arbitrarily large quantum systems. We took advantage of a supercomputing cluster to parallelize the code and make the computations extremely efficient.

REFERENCES

- ¹ A. M. C. Dawes, L. Illing, S. M. Clark, D. J. Gauthier, "All-Optical Switching in Rubidium Vapor," *Science*, **308**, 672 (2005)
- ² A. Melloni, M. Chinello, and M. Martinelli, "All-Optical Switching in Phase-Shifted Fiber Bragg Grating" *IEEE Photonics Technology Letters*, **12**, 42 (2000)
- ³ X. Hu, P. Jiang, C. Ding, H. Yang, Q. Gong, "Picosecond and low-power all-optical switching based on an organic photonic-bandgap microcavity", *Nat. Photon*, **2**, 185 (2008)
- ⁴ A. M. C. Dawes, L. Illing, S. M. Clark and D. J. Gauthier, "All-Optical Switch Controls Strong Beams with Weak Ones," *OPN*, Dec. 2005, p 24, (2005)
- ⁵ P. J. Curran, "Polarized visible light as an aid to vegetation classification," *Remote Sens. Environ.* **12**(6), 491–499 (1982).
- ⁶ M. J. Duggin, "Imaging polarimetry in scene element discrimination," *Proc. SPIE* **3754**, 108–117 (1999).
- ⁷ B. J. DeBoo, J. M. Sasian, and R. A. Chipman, "Depolarization of diffusely reflecting man-made objects," *Appl. Opt.* **44**(26), 5434–5445 (2005).
- ⁸ P. Meystre, M. Sargent, *Elements of Quantum Optics*, pp. 60-62, Springer, 1998
- ⁹ M. O. Scully, M. S. Zubairy, *Quantum Optics*, Cambridge University Press, Cambridge (1997)
- ¹⁰ S. M. Spillane, G. S. Pati, K. Salit, M. Hall, P. Kumar, R. G. Beausoleil, and M. S. Shahriar, "Observation of Nonlinear Optical Interactions of Ultralow Levels of Light in a Tapered Optical Nanofiber Embedded in a Hot Rubidium Vapor," *Phys. Rev. Lett.* **100**, 233602 (2008)
- ¹¹ J. Bures and R. Ghosh., "Power density of the evanescent field in the vicinity of a tapered fiber" *J.Opt.Soc.Am.A*, **16**, 1992 (1999)
- ¹² P.N. Moar, S. T. Huntington, J.Katsifolis, L.W.Cahill, K.A.Nugent and A.Roberts, *Near Field Modelling and Measurement of Tapered Optical Fibre Devices*, LEOS 1997 - Ca, U.S.A, <http://ieeexplore.ieee.org/iel3/4988/14076/00645237.pdf>
- ¹³ P.N. Moar , S.T. Huntington, J. Katsifolis, L.W. Cahill, A.Roberts, and K. A. Nugent "Fabrication, modeling, and direct evanescent field measurement of tapered optical fiber sensors" *Journal of Applied Physics*, **85**, 3395 (1999)
- ¹⁴ E. R. I. Abraham and E. A. Cornell, "Teflon Feedthrough for Coupling Optical Fibers Into Ultrahigh Vacuum Systems," *Appl. Opt.* **37**, 1762-1763 (1998)
- ¹⁵ T. A. Birks and Y. W. Li, "The shape of fiber tapers," *J. Lightwave Technol.* **10**, 432 (1992).
- ¹⁶ H. Sasada, "Wavenumber measurements of sub-Doppler spectral lines of Rb at 1.3 pm and 1.5 pm," *IEEE Photonics Technology Letters***4**, 1307-1309 (1992).
- ¹⁷ H. S. Moon, W. K. Lee, L. Lee, and J. B. Kim, "Double resonance optical pumping spectrum and its application for frequency stabilization of a laser diode," *App. Phys. Lett.* **85**, 3965-3967 (2004).
- ¹⁸ J. E. Bjorkholm, and P. F. Liao, "Line shape and strength of two-photon absorption in an atomic vapor with a resonant or nearly resonant intermediate state," *Phys. Rev. A* **14**, 751-760 (1976).
- ¹⁹ B. V. Zhdanov, and R. J. Knize, "Progress in alkali lasers development," *Proc. SPIE* **6874**, 68740F (2008) and references therein.
- ²⁰ B. Misra, and E. C. G. Sudarshan, "The Zeno's paradox in quantum theory," *J.Math. Physics* **18**, 756-763 (1977).
- ²¹ W. M. Itano, D. J. Heinzen, J. J. Bollinger, and D. J. Wineland, "Quantum Zeno effect," *Phys. Rev. A* **41**, 2295-2300 (1990).
- ²² Y. Huang, J. B. Altepeter, and P. Kumar, "Interaction-free all-optical switching via the quantum Zeno effect," *Phys. Rev. A* **82**, 063826 (2010).
- ²³ B. J. DeBoo, J. M. Sasian, and R. A. Chipman, "Depolarization of diffusely reflecting man-made objects," *Appl. Opt.* **44**(26), 5434–5445 (2005).

-
- ²⁴ J. F. de Boer, T. E. Milner, and J. S. Nelson, “Determination of the depth-resolved Stokes parameters of light backscattered from turbid media by use of polarization-sensitive optical coherence tomography,” *Opt. Lett.* **24**(5), 300–302 (1999).
- ²⁵ D. A. Steck, “Alkali D line data,” <http://steck.us/alkalidata/rubidium87numbers.pdf>
- ²⁶ M.S. Shahriar, Ye Wang, S. Krishnamurthy, Y. Tu, G.S. Pati & S. Tseng, “Evolution of an N-level system via automated vectorization of the Liouville equations and application to optically controlled polarization rotation”, *Journal of Modern Optics* (2013)
- ²⁷ D. Stokes, *Principles and Practice of Variable Pressure/Environmental Scanning Electron Microscopy* (John Wiley & Sons, 2008), Chap. 8.
- ²⁸ S. Krishnamurthy Y. Wang, Y. Tu, S. Tseng, and M. S. Shahriar, “High efficiency optical modulation at a telecom wavelength using the quantum Zeno effect in a ladder transition in Rb atoms”, *Opt. Express* (2012)
- ²⁹ S. Weilandt, L. Alexander, and L. Gaeta, “Coherent control of the polarization of an optical field,” *Phys. Rev. Lett.* **81**(16), 3359–3362 (1998).
- ³⁰ M. Xiao, Y. Li, S. Jin, and J. Gea-Banacloche, “Measurement of dispersive properties of electromagnetically induced transparency of Rubidium atoms,” *Phys. Rev. Lett.* **74**(5), 666–669 (1995).
- ³¹ Shujing Li, Bo Wang, Xudong Yang, Yanxu Han, Hai Wang, Min Xiao, and K. C. Peng, “Controlled polarization rotation of an optical field in multi-Zeeman-sublevel atoms”, *Phys. Rev. A* **74**, 033821 (2006).